Non-destructive evaluation of additively manufactured materials: developing a coupled acoustic emission and thermoelastic stress analysis approach

A thesis submitted in fulfilment

of the requirements for the degree of

Master of Engineering

at

The University of Waikato

by

Denis Jouan

Supervisors:

Dr. Rachael Tighe (Waikato university), Prof. Rhys Pullin (Cardiff university)

KO TE TANGATA

THE UNIVERSITY OF
WAIKATO
Te Whare Wānanga o Waikato

2022

Declaration of authorship and published work

Chapter 3 and 4.1.2 was presented at the 2022 3MT master’s competition at the University of Waikato.

Chapters 3, 4.1.2 and 4.2.1 were presented at the IEEE Instrumentation and Measurement Society, New Zealand Chapter 2022 annual workshop.

Chapters 3, 4.1.2 and 4.2.1 were accepted as extended abstract and accompanying presentation at 2023 SEM Annual Conference & Exposition on Experimental & Applied Mechanics, to be held at the Rosen Plaza Hotel in Orlando, FL USA, June 5-8, 2023.

A journal article about Chapter 3 and 4 is currently in draft.

Abstract

A method combining two non-destructive evaluations techniques, acoustic emission and thermoelastic stress analysis, is proposed to monitor cyclically loaded monolithic and additive manufactured metallic samples for crack growth. Current literature was used to investigate additive manufacturing processes and their current quality control methods. A review of acoustic emission and thermoelastic stress analysis theory and recent applications is also provided. It was found that there was currently a gap in monitoring methods for additive manufactured parts under fatigue loading for crack growth due to internal defects. Acoustic emission and thermoelastic stress analysis have never been combined to monitor crack growth in monolithic or additive manufactured metals in such a way and would be ideal methods for crack growth monitoring under cyclic loading due to their inherent benefits. Thermoelastic stress analysis is a full-field non-contact non-destructive evaluation technique which can monitor surface stress fields in materials subjected to cyclic loading. Acoustic emission is ideal for monitoring fatigue damage due to its continuous monitoring capabilities of energy released by crack growth. The proposed method consisted of acoustic emission capturing continuously and saving any waveforms exceeding a set threshold while the thermoelastic stress analysis captured data at regular intervals. Acoustic emission energy was extracted from captured waveforms to provide crack initiation detection as well as a measure of crack severity. Thermoelastic stress analysis provided a crack tip location and enabled crack tip tracking as well as crack growth rate monitoring to complement the acoustic emission energy findings. Acoustic emission could not locate the crack because it only used a single piezoelectric sensor but could detect crack growth anywhere on the sample while thermoelastic stress analysis could give the crack location only if the crack was near the surface or within the field of observation. The method successfully detected cracks and tracked crack growth in monolithic aluminium samples, additive manufactured aluminium and additive manufactured titanium alloy samples under fatigue loading conditions. This method involves little modification to the part being observed, the surface must be painted with a thin coat of matt black paint for thermoelastic stress analysis, and a sensor must be attached to the part for acoustic emission. Acoustic emission energy detected crack growth before thermoelastic stress analysis in most tests however this was due to the experimental method, acoustic emission captures continuously while thermoelastic stress analysis is at regular time intervals. Issues with experimental method came to light in early tests but were addressed in the final tests using additive manufactured titanium samples. Future work includes testing additive manufactured samples with built-in subsurface defects and developing a chip-based system in order to make a smaller and cheaper monitoring system.

Acknowledgements

I would like to acknowledge University of Waikato staff Jonny Van Harselaar, Jack Hies, Larissa Kopf, Sophia Rodrigues, Ben Jackson and Stella Raynova. I would also like to thank my family for supporting me through this degree.

Table of Contents

List of Figures

List of Tables

Chapter 1

Introduction

1.1 Background

Additive Manufacturing (AM) of metals is becoming more attractive than traditional subtractive manufacturing with a 20.8% expected compound annual growth rate from 2022 to 2030 [1]. Inherent benefits of AM include high precision finished parts with complex geometries, including internal features, that would be difficult or impossible to manufacture with conventional machining techniques. Components that would usually require multiple parts can now be made of a single piece, reducing part counts This allows easier installation, reduces the risks of failure inherent of multi-parts systems and enables more efficient spare-parts logistics. Several materials are available from non-metallic materials like polymers and ceramics which are ideal for non-load bearing applications or rapid prototyping to metals including aluminium, steel or titanium which are more suited to load bearing applications. AM parts are manufactured directly from the CAD drawing with minimal manufacturing skills, reducing the requirement for highly skilled machinists. The aerospace industry is making a push for the use of AM parts in expensive low-run projects. The custom and low production quantities required for AM is ideal for such projects like the A-arms of the Waikato University student racing team as seen in Figure 1.

Figure 1. Titanium A-arms for the Waikato university student race car.

While finding diverse structural applications, AM still has drawbacks such as time consuming manufacture depending on size and AM technique as well as inherent defects like porosity, cracks and residual stresses. Some AM techniques output parts with near final dimensions which require post-processes such as milling to final dimensions, to remove support material and to improve surface finish, while most AM metal parts require heat treatment to remove residual stresses. The material undergoes rapid heating and cooling which introduces residual stresses that can negatively affect material mechanical properties. AM metallic parts can have similar mechanical properties such as yield strength and ultimate tensile strength (UTS) to their monolithic counterparts, and with heat treatment they can even exceed their conventional counterparts [2]. The fatigue properties of AM material have not been studied as extensively as conventional metals and researchers have been looking to identify what affects the fatigue life of AM parts as well as differences in fatigue life between conventionally manufactured parts and AM parts. Factors such as surface roughness, layer orientation and residual stresses from uneven heating can significantly lower fatigue life [3]. For example, fatigue loading AM metals perpendicular to the direction they are printed can lower fatigue strength between 40% and 75% when compared to the same material loaded parallel to the printing layers [4]. However, the effects can be reduced by various post-processing approaches such as surface machining and hot isostatic pressing (HIP). It was found that AM titanium samples which were machined and HIP treated displayed a 30% lower fatigue strength than wrought, annealed titanium; while stainless steel samples printed using SLM displayed a 5% to 15% lower fatigue strength compared to their wrought counterparts [4].

As the fatigue properties of AM metals have not been fully explored, it is critical that parts are inspected during and after manufacturing to ensure the part is manufactured without defects enable early crack growth detection before catastrophic failure of the part. Cracks and pores can be present after manufacturing and severely weaken the part, an example of such cracks can be seen in Figure 2. It would also be advantageous to be able to continuously monitor critical parts at risk of fatigue damage in situ to mitigate the current lack of knowledge about fatigue in AM and enable early crack growth detection before catastrophic failure of the part.

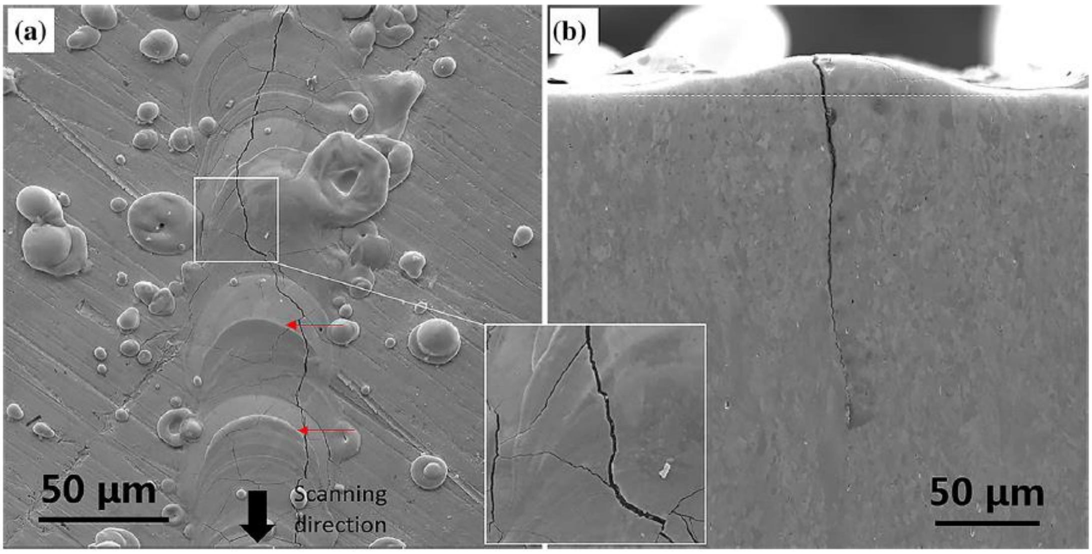

Figure 2. Crack formed during manufacturing in AM titanium part [5].

Current evaluation methods used on AM parts involve the use of destructive testing of test coupons after manufacture to detect any defects such as cracks and porosity in the coupon. The coupon is tested to failure and its mechanical properties and build quality are assumed to be representative of the parts. However, this is not a safe assumption as AM produces parts that are orthotropic in nature, meaning the properties depend on geometry, print direction as well as location on the print bed. Non-destructive evaluation (NDE) techniques can be used to further control and identify anomalies with printing parameters which may lead to defective parts [6]. By using NDE during printing, the need for destructive testing which requires the manufacture of a test coupon could be reduced, which would lower material consumption and waste. Scheduled inspections can detect any damage that may have occurred in service, but a part could undergo catastrophic failure between inspections. Increasing the frequency of scheduled inspection could reduce the change of failure between inspections but would also increase the machine downtime.

Continual in-situ monitoring using NDE as structural health monitoring would therefore be another way to ensure the part is not failing while in use. Inservice monitoring also means the part is used to its full potential service life instead of replacing it based on a time-based maintenance plan. Defects or cracks could be detected and monitored between scheduled inspections without stopping the machine or taking the component out of service. However, there are currently no established methods using NDE techniques used for continuous monitoring of AM parts in-situ for identification and monitoring of crack initiation and crack growth. A new approach which would enable in-situ monitoring of fatigue loaded AM metal parts using NDE techniques is needed to fill the current gap. There are many different NDE techniques available but techniques that are well suited to monitor for crack growth while a part is under fatigue loaded should be selected. Ultrasonic testing could detect cracks after they are formed but could not locate higher stress areas that could initiate crack growth before the crack is initiated. Digital image correlation (DIC) could be used to monitor the strain on the surface which would indicate crack growth, however, DIC requires multiple cameras and good lighting to function which can be challenging depending on the application and space available [7]. Infrared (IR) can work better because it uses one camera and can function without visible light present. Utilising IR with thermoelastic stress analysis (TSA) can show areas of higher stress which could be indicative of crack initiation and growth in the material. However, TSA is only a surface and near-surface technique and another method capable of continuous monitoring that could detect deeper cracks should be used in conjunction. Acoustic emission (AE) could fill such a role as it can monitor energy released by a crack which indicates initiation and growth.

TSA and AE were chosen to be combined to monitor cyclically loaded metallic AM parts because they suit cyclically loaded situations such as fatigue loading and can detect crack growth. TSA uses a processed recording from an infrared camera of the surface of the loaded part to output a stress map, indicating stress concentrations on the surface which could be either be caused by an existing crack or highlight areas where a crack may initiate. These areas of higher stress caused by cracks provide crack position and can also provide crack growth rate should the crack be growing. AE requires the use of a piezoelectric sensor attached to the surface to detect acoustic waveforms emitted by events occurring within the material such as crack growth. These waveforms can be processed to output the how many acoustic events occurred through time and how much energy was released. The number of events indicates crack formation, propagation and damage severity while energy released indicates a measure of how much new surface area is being created. TSA can struggle with thick parts but can detect, locate and track the crack. AE cannot locate the crack using a single sensor, but it provides valuable information on crack initiation, growth and severity, meaning that the methods complement each other well.

If successful, this method could be applied to all AM metallic parts in industries such as aerospace and motorsports that are used in structural applications and undergo cyclic loading. One example of using this method could be monitoring parts continuously over their lifetime for any crack growth using AE, while TSA is used to confirm crack growth. This would enable the possibility to swiftly replace parts in case of crack growth.

1.2 Aims and objectives

The aim of this thesis is to explore the potential of a combined inspection methodology of TSA and AE for the quality assurance of AM parts. To achieve the end goal, a set of objectives were established:

1. Establish independent methods and processing protocols for TSA and AE using laser-cut samples and preliminary testing.
2. Combine and refine TSA and AE methods and processing using waterjet cut samples.
3. Test notched AM samples with the combined method to collect data as well as further refine collection and processing method.
4. Test purpose-built AM samples with a built-in notch using the updated method to detect crack initiation and propagation.
5. Implement the method on AM samples to detect inbuilt subsurface defects.

1.3 Structure

This thesis begins with a review of the literature surrounding the topic in Chapter 2. Latest research in additive manufacturing was explored, as well as current quality assurance techniques. Then the theory of TSA was covered along with recent research in general with a focus on AM metals. Similarly, the theory of AE was explored as well as recent research. Literature combining both TSA and AE in general, and AM were discussed.

After exploring the recent advancements in the field, the proposed test method used in this study to monitor samples for crack growth was described in Chapter 3. This included samples developed to test the proposed method, equipment for the individual techniques, test conditions, individual set up and methods for TSA and AE separately as well as operations for both techniques combined and processing.

Following the method, the results were laid out starting with the first laser cut samples used to establish the monitoring method in Chapter 4. Tests using water jet cut aluminium samples to develop the combined data were presented along with AM aluminium sample tests used to refine the method. The last results with purpose-built titanium samples were presented and discussed.

Finally, the study was concluded and summarised in the conclusion section along with future work in Chapter 5.

Chapter 2

Literature review

2.1 Additive manufacturing

Additive manufacturing is defined as the process of making parts from 3D model data, usually by adding layer upon layer of material during a build. This is opposed to subtractive manufacturing and formative manufacturing methodologies which remove material from a larger piece of material [8].

There are eight main types of AM: binder jetting, directed energy deposition, material extrusion, ultrasonic, vat polymerisation, material jetting, powder metallurgy and powder bed fusion [9]. These techniques can be categorised according to the materials used, such as if the materials used are non-metallic or metallic. Non-metallic AM techniques such as the following are commonly used in rapid prototyping rather than structural roles due to the possibility of relatively quickly manufacturing cheap parts with weak mechanical properties.

2.1.1 Non-metallic:

Binder jetting involves a layer of powder which can be chalk, ceramic, plastics, etc., where a printer jets adhesive on the powder, binding it. Then a new layer of material is added, and the process is repeated until the part is completed. The process is economical with the machine itself being a low cost and inexpensive materials, but the parts created are fragile and require cleaning and hardening with an epoxy adhesive coating to improve their mechanical characteristics.

Material extrusion is used mostly for polymers and is what is most commonly known as 3D printing. A polymer wire is fed through a heated nozzle which melts the polymer and deposits it in the correct place layer by layer. Similarly, to binder jetting, the process is economical, but the final part is often fragile.

Vat polymerisation works by hardening layers of photopolymer resin with a UV laser. Resin is added over the previous layer to be hardened until the part is finished. This method can be expensive, with the products needed to be extracted from the resin and cleaned before being able to be used. However, it has a high level of precision and good surface finish.

Material jetting is like vat polymerisation but instead of the photopolymer being in a vat, it is jetted onto the previous layer and immediately hardened by UV lights, reducing waste. The layer thickness is very small creating a smooth surface and enabling accurate dimensions.

Ultrasonic AM involves the bonding of thin sheets of materials via ultrasonic welding. The part is created by stacking the sheets. A CNC machine or laser cutter can be used once the sheets are all stacked to cut the excess material. This post-processing means there is waste involved in creating the part, it requires materials to come in thin sheets, but it is relatively inexpensive.

2.1.2 Metallic:

Metallic AM is better suited for small run structural parts than non-metallic AM due to improved mechanical properties compared to non-metallic materials. The increased cost and printing time limit the method to be viable only in manufacturing a small number of fully developed parts rather than rapid prototyping. One such method is direct energy deposition which uses welding to create three-dimensional objects. A wire or powder is melted and deposited on the previous layer by a laser or electron beam until the part is completed as seen in Figure 3. This process can be used to create new parts but also for repairing damaged parts or adding new features to existing ones. One example of direct energy deposition is wire arc additive manufacturing which provides high material efficiency and print speed and is suitable for large parts by using an arc welder to add material [10].

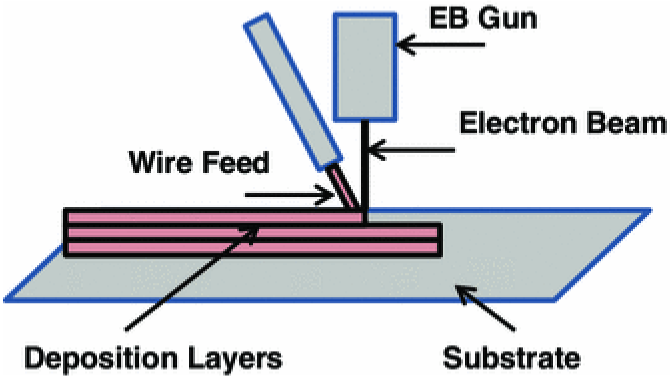

Figure 3. Generic illustration of WAAM process. Used with permission from [11].

Powder metallurgy uses metal powder that is pressed into a shape and then sintered, forming a strong metal shape. This powder can also be mixed with a polymer and extruded into a shape, the polymer is then burned off and the powder is sintered. The main defects affecting this method is un-melted powder [12] which decreases the performances of the part.

Selective Laser Melting (SLM) is a type of powder bed fusion, a layer of powder is deposited on the print bed and a laser melts the powder according to the geometry of the part as seen in Figure 4. A new layer of powder is then laid on top of the previous one and the process is repeated until the part is completed. This process can also be done with an electron beam which is called electron beam melting (EBM). SLM can create strong and complex parts out of ceramic, plastic or metals. Depending on the type of powder used, it can be relatively expensive, in addition, the machine itself can be a large investment. This method is currently in use by the space, aircraft and biomedical industries for metallic structural components [13]. As such SLM will be the method of primary focus in this research. Some of the main manufacturing defect types affecting SLM are lack of fusion (LOF), gas porosities and un-melted powder which are found where the powder is not melted properly or did not fuse with the previous layer [12]. LOF defects often appear due to the selection of inappropriate processing parameters when creating the part and can cause catastrophic failure in structural parts. Hatch spacing is the space between the laser passes, as shown in Figure 4. Hatch spacing plays a large part in the formation of LOF pores as the melt pool caused by the laser is spherical, so if the hatch spacing is too large, there will be un-melted powder in between adjacent laser passes as seen in Figure 4. This can also be caused by a lack of energy in the laser which creates a smaller pool of molten metal, increasing the space between the melted tracks as well as decreasing penetration of the molten pool into previous layers [14]. Scanning speed, laser power and layer thickness are other factors that can affect the formation of LOF defects. A faster scanning speed can reduce print time but could also create more porosity. Gas porosities are created due to the presence of gas trapped in the powder particles before they are melted or trapped environmental gas while the powder is being melted. A higher laser power could reduce porosity at the cost of introducing large residual thermal stress which could cause cracks. Careful thermal control and post processes are required to remove the residual stresses caused by rapid heating and cooling. Increasing layer thickness also has the potential to reduce print time, but a thicker layer would also reduce the accuracy of the print by reducing the ‘resolution’ and increase required finishing processes.

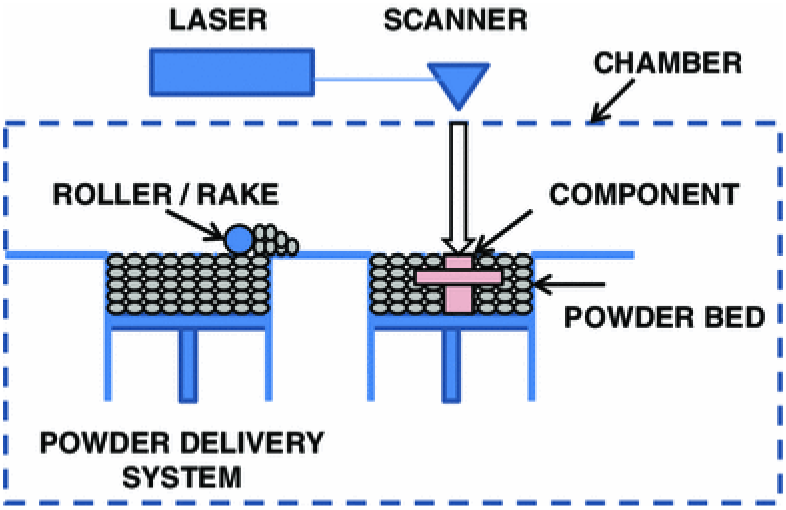

Figure 4. Generic illustration of SLM system. Used with permission from [11].

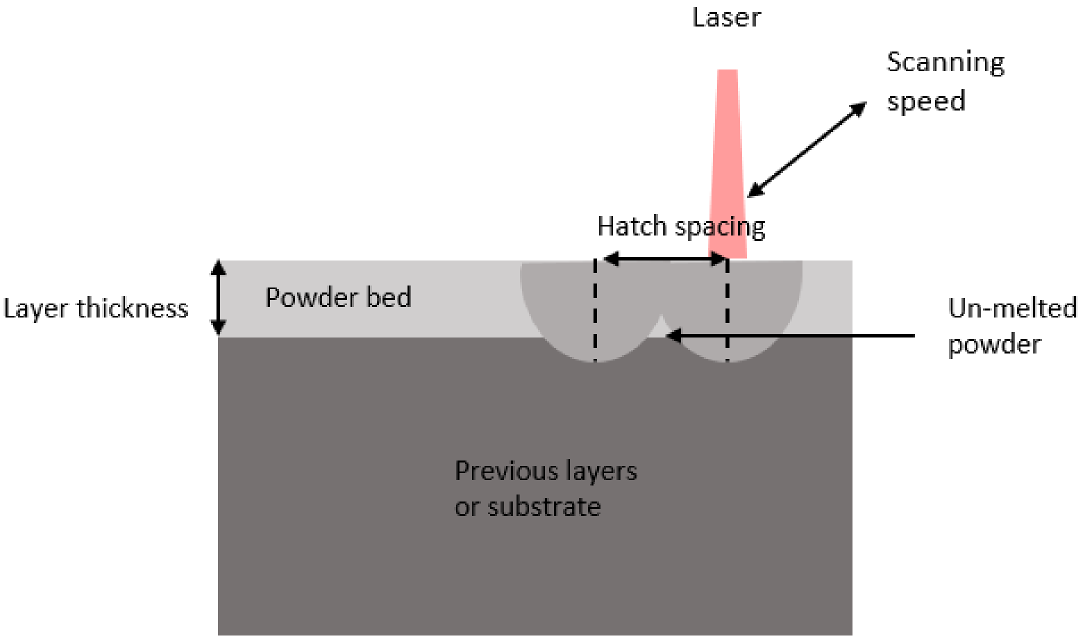

Figure 5. Parameters for selective laser melting with lack of fusion defect pictured. Adapted from [15]

2.1.3 During manufacturing quality control techniques:

Monitoring during the manufacturing process is a growing area of research to develop new and improve existing methods to detect defects as they are printed [16]. Such methods aim to identify anomalies during printing that could increase the changes of defect formation. One such method involves monitoring the melt pool temperature during printing using IR cameras and thermocouples, aiming to detect cold spots which could result in LOF defects [17]. The size of the melt pool can be measured to determine if the laser power is sufficient or if it is too high or too low and could cause LOF defects or porosity [18]. In [16], an IR camera with a 900 Hz framerate was used to monitor surface temperature of the part being manufactured and was able to detect the LOF defects, which were confirmed later by micro-computed tomography (micro-CT) imaging. The colder areas indicated a smaller melt pool and decreased penetration in the material which would cause LOF defects. Acoustic Emission (AE) was also used to monitor parts during the AM process for cracks [19]. It was found that it took up to an hour between a layer being printed and cracks forming, indication that cooling after the print could play a role in crack initiation. The AE data was compared with micro-CT and a direct relation was found between the two confirming that AE could be used to monitor crack growth during manufacturing. The ability to detect a defect during manufacturing enables the issue to be corrected before shipping and installing the part.

2.1.4 Post-manufacturing quality control techniques:

Inspections post-manufacturing using DIC and X-ray computed tomography (XCT) are currently being developed to detect and measure porosity in AM metallic parts [20]. XCT is an offline and specialised inspection method where x-rays are beamed through the part to identify defects. XCT shows promise to enable three-dimensional scans to determine porosity and detect defects, however it is a time-consuming and expensive method and part size is limited to the XCT system size. Conventional A-scan ultrasound can also be used to detect defects within the material, it is faster than XCT but less accurate and cannot be applied to parts with complex geometries. It works by sending an ultrasound wave through the material and measuring how long until it returns, if the signal indicates a shorter distance than the other side of the part, at least one defect must be present.

The feasibility of using TSA on brackets made of AM metals using EBM is being investigated [21]. The study was investigating using TSA for stress analysis on AM brackets undergoing cyclic loading and compared the experimental stress obtained by TSA to FEA results. The initial FEA model made using the CAD dimensions was updated with the built dimensions to provide results representative of the finished part. The TSA provided useful information on the behaviour of the brackets being cyclically loaded by highlighting stress concentrators and areas of higher stress which matched with the FEA study by taking profiles in the same position with TSA and FEA and comparing the stress amplitudes. The agreement between FEA and TSA for stress raiser location showed that TSA can be used to perform stress analysis on AM parts to monitor the material' response to loading.

2.2 Thermoelastic stress analysis

Thermoelastic stress analysis (TSA) is a non-destructive and non-contact method which uses an infrared camera to monitor the surface of a material or component undergoing a cyclic load to assess the surface stress distribution. TSA is based on the concept of the thermoelastic effect which can be described as a material displaying a cyclic thermal response when it is subjected to a cyclic load [22]. The temperature variation in the material is opposite in phase to the loading cycles and when adiabatic conditions are achieved, it can be related to the sum of the principal stresses by Eq1.

$$\Delta\sigma = -\mathrm{K}\frac{\Delta \mathrm{T}}{\mathrm{T}} \qquad (Eq1)$$

Where ΔT is the temperature change, T is the temperature, Δσ is the change of the sum of the principal stresses. K is the thermoelastic coefficient which can be obtained either theoretically or experimentally using readily available material properties as seen in Eq(2).

$$K = \frac{\propto}{\rho C_p} \qquad (Eq2)$$

Where $\propto$ is the thermal expansion coefficient, ρ is the density and C_p is the specific heat capacity at constant pressure.

Equation 1 was theorised for isotropic materials, but in the case of orthotropic materials, the following equation must be used[22]:

$$\frac{\Delta \mathrm{T}}{\mathrm{T}} = \mathrm{K}\left(\Delta\sigma_1 + \Delta\sigma_2\right) \qquad (Eq3)$$

Where $\Delta\sigma$ is the change in the direct surface stress, the subscripts 1 & 2 are the principal directions. This is particularly useful in composites where the material properties are often directionally dependant but also for AM parts where the print direction can affect mechanical performance.

The thermoelastic effect was first theorised in the 1851 account of W. Thompson (Lord Kelvin) [23] who discovered a relationship between the changes in the sum of stresses in a solid and a temperature change in said solid. This theory was confirmed with experimental results in 1915 [24]. The first time TSA was implemented without contact was in 1967 using an infrared radiometer to detect small temperature changes caused by the change in stress in a vibrating cantilever beam [25; 26]. This was using a point measurement; the radiometer was not capable of measuring multiple points at once. The first commercial system for TSA was manufactured in 1982 and was called the SPATE 8000 (stress pattern analysis thermal emission). This system required the use of liquid nitrogen cooling and took a very long time to capture data as it sequentially recorded every individual pixel, however it was the first spatially resolved system outputting an image rather than a point measurement. As it was very expensive, only select research groups around the world had access to the equipment. An example of using SPATE and TSA to monitor composites can be seen in this study where a T joint was loaded at a 45° angle and monitored for areas of higher stress [27]. TSA proved to be useful in mapping areas experiencing higher stress which were then confirmed using FEA.

Rapid development in infrared camera technology since the 1980s have enabled much faster and cheaper data recording, with cameras commonly available rendering TSA more accessible to researchers and industry and driving a research boom in the field. Micro-bolometers have sensor arrays using one sensor per pixel to create the image instead of using one sensor in a scanning pattern like SPATE, vastly improving spatial and temporal resolution. Bolometers can be cooled or uncooled depending on their operating temperature, uncooled systems are generally less sensitive than cooled ones but are still sensitive enough for most applications with typical thermal resolution between 30-100 mK [28]. Another system to detect changes in temperature from IR radiation are photon detectors. They detect photons emitted by the surface to identify the temperature and have a high integration rate (equivalent to a low exposure time in photography) in the order of µs enabling a high frame rate, however photon detectors require cooling of the sensors to function [29]. Photon detectors are generally bulkier than micro-bolometers due to the required cooling but provide improved thermal resolution of typically < 20 mK. More recent advances in IR detection technologies include new cheap chip-based thermal imaging cameras. Most chip-based thermal imaging cameras currently show lower thermal resolution in the order of ± 1 to 2 K with some systems having a thermal sensitivity of less than 50 mK but show great potential for compact, low-cost small monitoring systems for TSA [30].

The sampling frequency of the IR camera must be higher than twice the loading frequency to satisfy the Nyquist frequency [31]. A lock-in algorithm is applied to each pixel in the raw IR data using the loading frequency as the reference signal to yield the surface stress [32]. The temperature amplitude of each pixel can be calculated by comparing temperature when no load is applied and when the load is applied with the least squares method. Once this was repeated for each pixel, K can be applied to find the surface stress amplitude.

TSA measures change in surface and near surface stress fields. This is particularly advantageous for use in non-destructive evaluation and in-situ monitoring of cyclically loaded parts. However, the part must be loaded at a high enough frequency to provide adiabatic conditions to accurately determine stresses, this threshold frequency is dependent upon material properties. If the loading frequency is too low and adiabatic conditions are unable to be maintained, dissipation occurs and temperature amplitudes smaller than a certain magnitude cannot be observed [33]. The loading frequency required to maintain adiabatic conditions is material dependant and influenced by the material’s thermal conductivity, the stress gradient of interest in the structure also influences the minimum loading frequency [22]. A loading frequency in the range of 20-25 Hz is suitable for aluminium [34].

For TSA to remain a NDE technique, the cyclic loading should be within the material’s elastic region to avoid damaging the part. TSA requires the surface to have a high and uniform emissivity to enable quantitative stress analysis and increase thermal sensitivity by more closely resembling a black body [34]. This can be achieved using two to three ‘passes’ of matt black spray paint on the surface which is between 12-27 μm [35].

The assumptions when using TSA to detect defects is that the defects present act as stress concentrators, altering the stress fields on the surface and lowering the service load limit of the part. Only defects severe enough to act as stress concentrators are considered a cause for concern as mentioned in [36]. One of the advantages of using a full-field, non-contact method like TSA is that the part being monitored can a range of scales and does not need to be modified, except for a thin coat of paint, which can be removed if required.

The data from any inspection can also be compared to the previous inspections to monitor for crack growth or other defect formation or progression. However, TSA relies on optical access to the surface. In addition, as previously mentioned TSA is a surface and near-surface technique meaning that if a crack is too deep below the surface and does not alter the surface stress field it will not be detected by TSA.

2.2.1 Applications

A large amount of research has been conducted using TSA for damage detection. It has been used in applications where the material undergoes vibration-based loading for identification of stress concentrators with a goal of in-service monitoring of composite aircraft panels [36]. TSA was used on a fully restrained honey-combed carbon-fibre reinforced polymer (CFRP) composite panel which is representative of a secondary aircraft panel, and it was loaded using vibrations to determine the viability of using such test methods in a laboratory setting. The stress concentration around the bolts holding the specimen were clearly visible in the TSA stress data. Vibrations have also been used to cyclically load a pipe, allowing TSA to inspect the pipe welds in-situ to work towards in-situ monitoring in a power plant [37]. The main issue with using vibrations to load the pipes were that the amplitude was introducing movement in the pipe relative to the sensor and introducing spatial noise. However, the study proved successful in applying TSA to in-situ pipe welds, enabling surface stress fields to be analysed. Another study working towards an in-situ, out of laboratory, application of TSA applied the technique to a joint in a bucket wheel excavator to monitor for stress concentrators under normal loading [38]. FEA was performed before experimental results were collected. The main issue the authors came across was the randomness of the loading under normal operation, TSA usually requires a sinusoidal regular loading to enable the lock-in procedure to function but the vibrations occurring in the excavator were random. However, implementing a self-referencing processing mode can partially solve the random loading issue by finding places in the signal where the stress amplitude is significant and in sync with the loading. This did not solve the issue entirely because only some parts of the recording fit the significant stress amplitude syncing with the loading, therefore TSA could only be conducted during these parts of the recording. To obtain a usable signal from the seemingly random loading, a strain gauge was used along with a Rainflow-counting algorithm, typically used to convert cyclic stress of varying amplitudes to an equivalent cyclic stress with constant amplitudes. This was used to calibrate the TSA image to obtain accurate stress values which were validated by the FEA, proving that TSA can be used to monitor structures with random vibrations in-situ.

Work has also been conducted in the assessment of impact damage using constant cyclic loading and impulse loading to load the material. Crump et. al. [39] studied impact damage in composite overwrapped pressure vessels, the damage was simulated by an internal machined slot, and pressure was cyclically increased and decreased using a piston. The subsurface damage could be detected using TSA which was confirmed using X-ray micro-CT. Similar work was conducted with TSA being used to detect impact damage in woven glass reinforced epoxy composites but impulse loading was explored instead of using cyclic loading. [40] Cyclic loading is a limitation for TSA as it can be difficult to cyclically load parts in-situ if the system is not already cyclically loading the part. It was found that impulse loading was sufficient in allowing TSA to detect changes in damage severity. [41] combined TSA and pulse heating thermography to detect impact damage in fibre glass composite material. It was found that using both methods together could detect delamination and fibre fractures caused by impact.

CFRP is a useful orthotropic material used in many applications and is a large area of study for TSA research. It is possible to detect debonding of layered composites using TSA [42]. The T-joints made of bonded CRFP were cyclically loaded and TSA was used to measure the debonding between layers. The TSA results were confirmed using strain gauges and established ultrasonic methods. Similar research using thermoelastic phase analysis (TPA) on cyclically loaded CFRP to monitor damage and as a fatigue limit index [43]. This method was used to estimate the fatigue limit of the material. It was found that the temperature increases related to the cyclic loading caused the fatigue limit to be overestimated, however the fatigue life was still in good agreement with the S-N curve for this material. It was also found that laminate orientation and if resin was present on the surface impacted TSA results in CFRP samples [29]. In this case, the specimens remained unpainted but the resin on the surface with a thickness of 30 μm displayed a similar thermal-conduction properties to a paint layer. When testing a sample with 60 μm of resin and another with two passes of matt black paint, it was found that the change in temperature across the paint were very close to the calculated values, while the change in temperature through the resin sample were consistently lower than the calculated value and decreased further as the loading frequency increased. Multiple studies have been conducted on fatigue damage detection using TSA in composites. TSA was used to detect cracks in the fibres of fatigue tested woven composites [44] and to evaluate the fatigue limit of glass FRP composites [45; 46]. TSA was also used in conjunction with Markov chains to determine S-N curves of laminate composites undergoing cyclic loading [47]. This method proved effective at predicting fatigue damage and allowed the creation of S-N curves.

Calibrating K for use in AM materials can be difficult due to their orthotropic nature, this can introduce error in the TSA stress data, therefore, a correction factor must be used to eliminate the noise. A correction factor and strain gauge were used to develop a method of TSA that can be applied to orthotropic materials such as the glass epoxy laminate samples used in this study [48]. The strain gauge measured the longitudinal strain within the material which was then input into the calibration constant. The specimens were cyclically loaded to introduce fatigue damage and assessed using the newly devised method which was validated with visual inspection and theoretical results. TSA has also been used to validate FEA findings, full-field strain maps were generated using TSA with two proposed methods and FEA on notched fibre reinforced polymers [49]. Parameters obtained from the surface of the composite were required to create the strain map while remaining invariant to the temperature gradients. The first method could work without two thermo-mechanical coefficients and displayed good agreements with other established methods while the second method could be applied to orthotropic composites without a surface coating. Both methods proved successful in generating the surface strain maps and confirmed the FEA study.

Crack detection and tracking has been undertaken in metal samples using TSA. It was demonstrated that TSA could detect crack initiation and location with both a microbolometer and a photon detector [50]. The latter was a higher spatial resolution but also a much higher price than the microbolometer. A hole was drilled in an aluminium sample to provide an initiation point for crack growth before the sample was cyclically loaded at a steady frequency and loading. The data was decomposed using Chebyshev polynomials to compare the current state with the original state of the sample and measure crack length. [51] used TSA to monitor crack growth in welds in a cyclically loaded cruciform joint using a microbolometer. A novel method for crack growth monitoring based on image segmentation was proposed and found to be able to monitor crack growth with an accuracy of ± 0.3 mm. This method involved taking a window over the monitored area and applying a threshold to the TSA data to increase contrast, any gaps in the surface stress would signify a crack as seen in Figure 6.

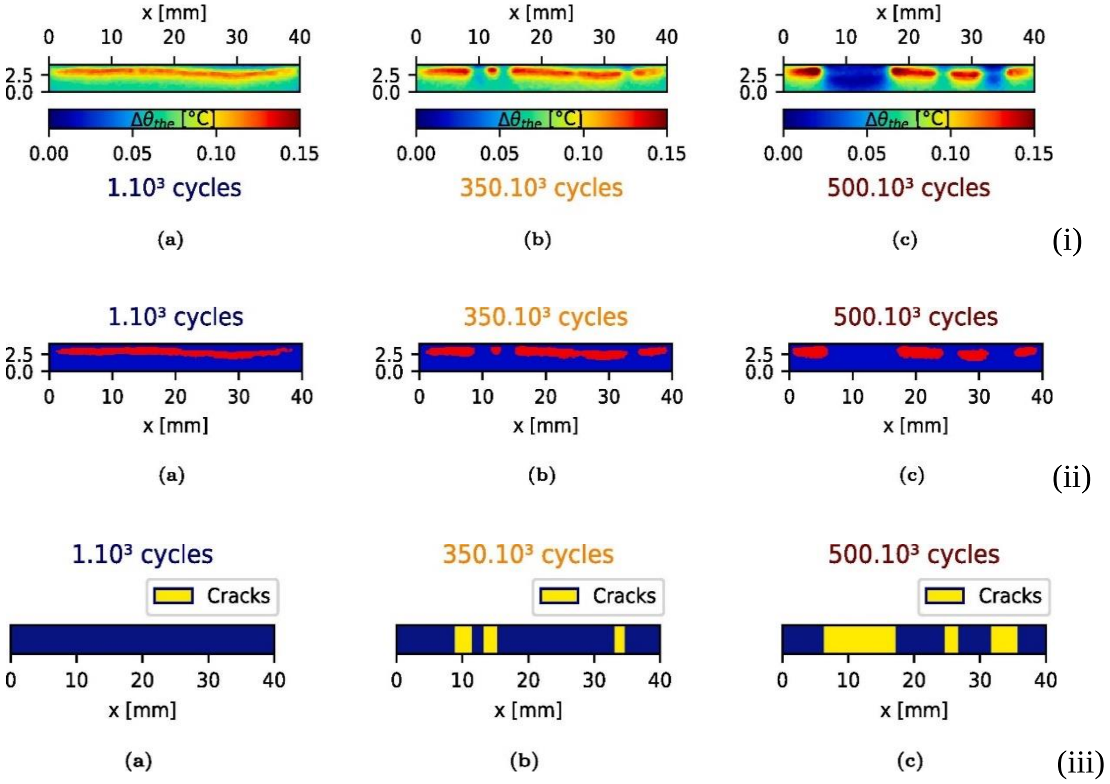

Figure 6. (i) shows the evolution of the stress concentration in the weld joint during fatigue testing. (ii) shows the thresholding of the data. (iii) shows the post-treatment output with the crack highlighted. Reproduced with permission from [51]

Crack growth monitoring can also be automated [52]. A microbolometer was used to find the crack tip and record its path with TSA. The IR camera was mounted on high precision linear movement stages to enable the camera to move in two dimensions across the samples surface. As the crack tip remained at the centre of the image, the frame could be smaller to reduce the size of the data while keeping the same spatial resolution. When the crack tip moves, the camera is automatically moved to keep the tip in the centre of the frame. This method proved successful in monitoring for crack growth but adds complexity to the technique by requiring two stages to be added to the setup as well as limiting the observation area. Automated crack detection and tracking can also be achieved without moving the camera [53]. An algorithm can be used to detect crack tip location by tracking changes in the surface stress field provided by TSA. This method could detect cracks with ±1 mm accuracy and track their path as confirmed via inspection of the broken sample.

TSA has been combined with other techniques before to validate findings. DIC was used in conjunction with TSA to better identify the sources of the TSA signals in CFRP laminates [54]. This method used DIC to input strain values in thermoelastic models instead of using strain gauges. The models were then validated using TSA data and the largest difference between the DIC and TSA $\frac{\Delta T}{T}$ was 1.65×10^{-4} indicating a good agreement between the models and TSA. This combined TSA and DIC method was also applied to stainless steel T-joints to detect and monitor crack growth [55]. The stress concentrators, i.e., the crack tip could be located using both the TSA and the DIC and compared. Both techniques agreed well with each other and theoretical results in crack position.

2.3 Acoustic emission

Acoustic emission (AE) can be defined as "the class of phenomena whereby transient stress/displacement waves are generated by the rapid release of energy from localised sources within a material, or the transient waves so generated" [56]. The piezoelectric sensors are stimulated by stress waves emitted by crack nucleation and growth [57], inclusions, loose parts or structural motion, a representation of which can be seen in Figure 7. The sensor system then converts the signal received as stress waves to electrical signals [58]. These signals can be used to indicate the position of the AE source in three dimensions, along with the severity and the type of damage [57]. In addition to instantaneous monitoring, the data collected can be saved and compared to previous data to monitor for any change. AE is very sensitive, with a minimum limit in the order of 10^{-18} J which means it can detect early cracks typically long before other methods [57].

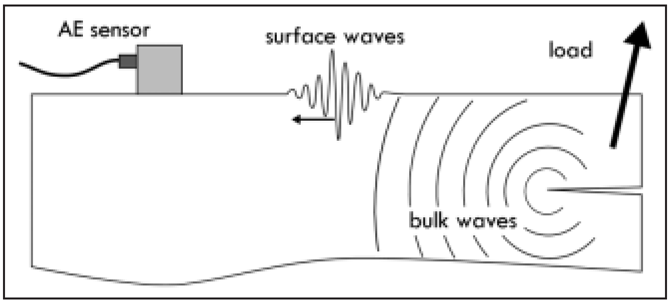

Figure 7. Working principle of AE reproduced with permission from [59].

AE can determine the position of a source by using multiple sensors and triangulating its position with good accuracy [60]. This enables detection of AE events inside the volume of a material using the material's speed of sound which can be measured with the AE sensors and the delay between the detection of successive signals at different sensors. The sensors are usually placed on the surface of the material with a layer of petroleum jelly, silicon or other viscous liquid to ensure acoustic signal transmission between the component and sensor. The full signal can be recorded and stored as well as the basic parameters of each waveform. The number of signals detected indicates the degree of damage for example, when looking at fracture, the number of signals detected is related to the crack formation rate, propagation speed and the degree of damage.

One of the most basic and important experimental setting in AE is setting a threshold value for the signals [61]. If the signal voltage is higher than that threshold, it will trigger the acquisition. This enables the elimination of background noise such as signals created from rubbing. The amplitude (A) is the voltage (V) of the highest peak of the waveform. It can also be measured in dB with the following equation:

$$dB = 20\log\left(\frac{A}{A_{ref}}\right)$$

Where A is the measured voltage and A_{ref} is a constant reference value that is specific to each AE system.

The energy released from the source, also called energy (E) or absolute energy is measured in 'attoJoule' (10^{-18} J) and can be described as:

$$E_{abs} = \int_0^{t_1} V^2(t)\,dt$$

Where the waveform starts at time 0 and ends at t_1.

The other main parameters of the waveform are the signal rise time (RT) which is the time between the first signal threshold and the highest peak, the duration (Dur) is the time between the first and last signal threshold as seen in Figure 8. The inverse of the opening slope called RA, can be defined as RT divided by A as seen in Figure 8 [62]. Different frequencies can also be extracted from the waveform: the average frequency (AF), peak frequency and the central frequency. The AF is calculated by counting the threshold crossings and dividing them by the Dur in kHz. The peak frequency is the frequency with the highest magnitude of the waveform and the central frequency is the centre of the frequency spectrum. Some parameters are sensitive to fracture sources such as the energy released, frequency, RA, Dur and RT and can be used to determine the fracture mode [63]. The energy released in the waveform is related to the creation of new surface area and can be obtained by applying root-mean square (RMS) to the waveform [64].

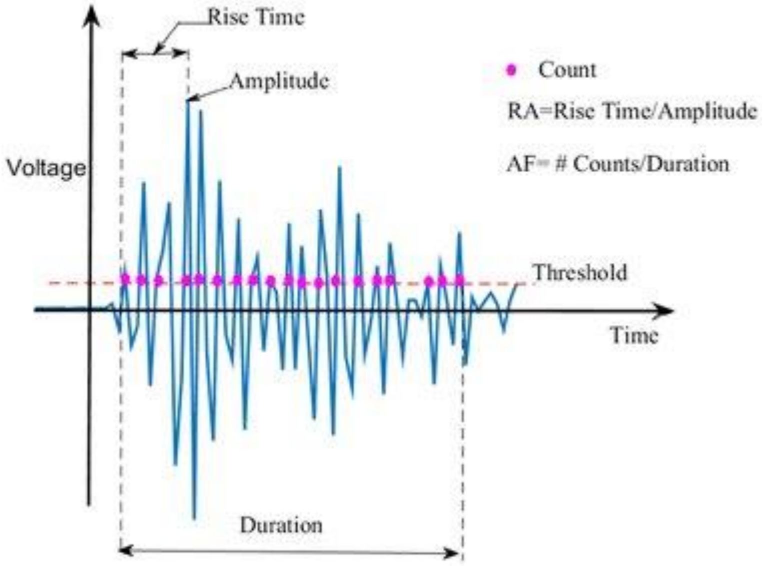

Figure 8. AE signal characteristics used with permission from [65].

AE was first investigated by Kaiser in 1953, with the first documented application published in 1964 [66; 67]. The true qualities of AE were explored and many NDE applications were published in the 1970s. From then on it became an established NDE technique due to its ability to assess and monitor for damage in many different materials and applications.

Similarly to TSA, AE required a sampling rate of at least double the frequency of the actual signal according to the Nyquist theorem [68]. In AE the sampling rate is typically much greater than double the original frequency and can reach 10 times or more. This improves any further data analysis as the signal is more accurate.

Figure 9 shows the typical AE activity expected as a sample is loaded. When a material is loaded, for example to L1 in Figure 9, AE activity created by plastic deformation is usually recorded. If the material is unloaded and reloaded to the same load, no new AE activity will be recorded because all the damage that would occur at L1 has already happened in the initial loading. This is called the Kaiser effect [69], named after Joseph Kaiser who was one of the early researchers of modern AE testing. If the load is further increased to L2 in Figure 9, new AE sources form and create fresh AE activity. Assuming that critical damage was sustained from load L2, AE activity will occur again at lower load L3 if unloaded and reloaded. For example, crack initiation requires a higher load than crack propagation because the cracks act as stress concentrators and locally increase stress. The ratio between load at the beginning of AE activity and the previous maximum load (i.e. $\frac{L3}{L2}$) is called the Felicity ratio (FR) [70]. If the material is intact, FR ≈ 1. This means the Kaiser effect is valid and no new damage is occurring. When the FR decreases, it means there is an accumulation of damage.

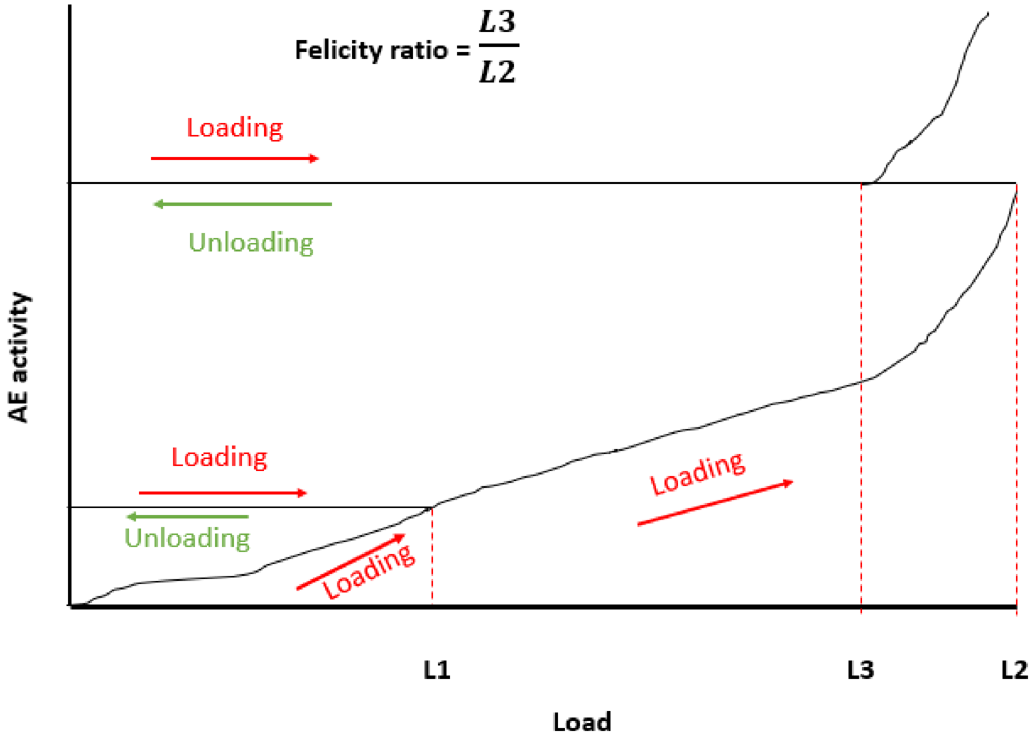

Figure 9. Kaiser effect and Felicity ratio. Reproduced from [57].

The FR and Kaiser effect are useful to provide an evaluation of the material's condition but do not provide a complete picture of the fracture mode, this is especially important in composites. The velocity and magnitude of the AE source dictate the amount of energy released and the amplitude of the signal. The amplitude is also proportional to the speed of the crack propagation and the quantity of surface area generated by the crack. This means that a large crack propagating quickly will generate larger AE signals than a smaller crack propagating slower. AE can also determine the orientation and the movement direction of the crack through the material via the use of multiple sensors. The geometry of the material can affect the recorded signal by guiding it (in a thin material such as an aircraft's skin) or with echoes and other noise.

2.3.1 Applications

AE has long been studied and used to monitor damage in laboratory settings and in-situ on multiple types of materials. A study was conducted on the ability of AE to both differentiate source type and damage severity using a series of tests with known signals generated by PLB and ball bearings drops [71]. It was found that AE could differentiate between source type by comparing a known source type signal to experimentally obtained signals and it could be used to monitor for early damage onset. The capabilities of AE to characterise damage in notched steel plates that were cyclically loaded was also tested [72]. It was found that as damage accumulated and the crack grew, energy and duration of AE signals increased. A change in RA value also indicated a shift from tensile mode to shear mode. These changes occurred approximatively 100 to 1200 cycles before failure and could therefore be used as indicators before failure occurs.

Multiple processing methods have been developed, both simple and advanced as [73] showcased. Using simple hit count and energy released proved to be able to monitor a gear tooth for failure but had a large memory footprint. It was found that using the Chebyshev descriptors and Shannon entropy methods both used a reduced memory footprint while still being able to monitor for damage. This method uses wavelet reconstruction of the signal, then the Chebyshev polynomial decomposition of each wavelet is calculated. These moments can be compared to a baseline waveform. AE energy can be calculated using root mean square (RMS) which allows it to be used as an effective way to monitor damage in steel samples [64].

AE has been studied on AM metals in recent years. The first studies applying AE to AM parts were conducted by Strantza et. al. [74]. An AM beam of titanium was loaded using four-point bending while continuously monitored using two AE sensors. It was found that AE could locate a crack and track its propagation as well as give an indication on crack severity using cumulative hits, amplitude, average frequency and duration. The Kaiser effect and Felicity ratio were found to be valid in AM metals like in conventional metals. This work was built upon further using cyclic loads rather than a static load [75]. This study confirmed that AE can be used to monitor AM metals for crack propagation due to fatigue loading and be used as an early warning sign of crack propagation and component failure.

2.4 TSA and AE coupled

Several papers in the literature have conducted research using AE and infrared thermography (IRT) in composite materials. In [76], two AE sensors were used to measure the AE signals generated by damage in a cyclically loaded woven C/SiC while using an IR camera to measure the thermal dissipation in the sample. The thermal dissipation slowly increased to a steady value and remained there until before failure of the sample where it quickly increased. The energy extracted out of the AE waveforms showed that there was a rapid increase in AE activity and energy at the start of the sample to a steady value until failure with a similar rate to the thermal dissipation. Both monitoring techniques agreed with the damage evolution of the sample which showed that they could be used for damage monitoring in woven C/SiC samples. DIC, IRT and AE were combined to provide strain and temperature differential maps to detect and monitor damage hot spots while AE was recording continuously for activity in fibre reinforced polymer composites [77]. Two AE sensors were used to count AE hits and measure the energy released, activity recorded at both sensors remained low until damage occurred in the sample at which point, they rapidly increased until failure of the sample. The AE signal frequency also showed that there were three stages of fatigue life for the material, and they could be tracked to determine which stage of fatigue life the material was currently in to calculate the remaining service life. The DIC and IRT were captured at the same time to compare their findings, increasing reliability of the results. It was found that IRT is a suitable monitoring method, where the camera does not need to be locked into the loading frequency. This is acceptable for slow loading frequencies (below 10 Hz) as used in these sources. IRT was also used with a 100 Hz sampling rate IR camera along with AE to monitor crack growth in ceramic matrix composites[78]. To monitor the temperature rise, multiple parallel lines were placed at regular intervals of 0.226 mm perpendicularly to the crack growth direction as seen in Figure 10. The interval 0.226 mm was experimentally chosen as it is the true size of each pixel in the IR camera used in this experiment. This is very useful in the case where the crack does not grow straight out of the notch and deviates up or down, the lines will still detect the rise in temperature cause by the passing crack tip. This crack growth was then compared to the AE energy which demonstrated a very similar trend as the sample was cyclically loaded. The measurement of the crack using IRT was proven to be accurate to within 0.1 mm when compared to optical measurements made after failure.

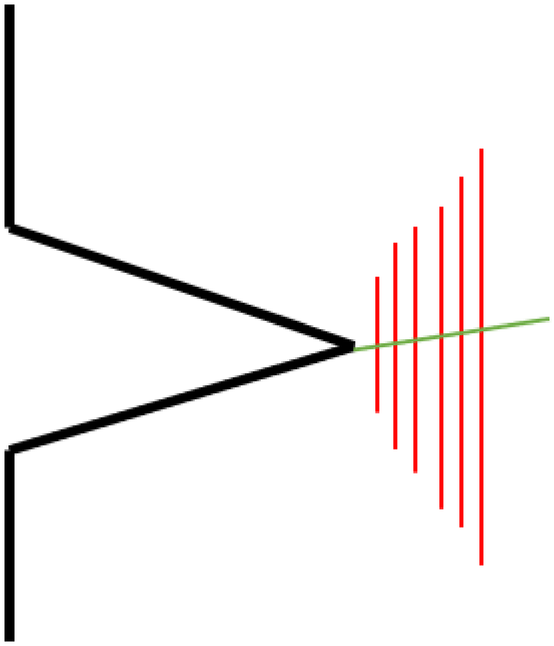

Figure 10. Lines monitoring crack growth representing the method used in [78] (red), crack growing (green).

AE and IRT were also used in monolithic metals, two AE sensors were used to study the tensile behaviour of steel samples by measuring the energy released during tensile testing. The energy released is high at first during the initial elastic deformation phase and start of the plastic deformation phase of the stress-strain curve of the sample before decreasing to almost no energy being released. Just before failure occurs, the energy released increases again. IRT was also applied to the sample where a temperature increase can be seen due to the high strain and culminates during the necking phase before fracture. The temperature increase is caused by increased strain, meaning temperature can be used to monitor strain. AE energy and temperature change obtained through IRT were proven to have similar reactions to increasing stress during a tensile test, with both increasing at the same time when the initial plastic deformation occurs [79]. This is promising to be able to determine fatigue limits in steel samples in the future using these techniques. AE and IRT were also applied to a Ti-alloy plate to determine if crack growth could be detected during a tensile test [80]. Both methods could detect the plastic deformation in the sample and the crack forming. IRT can be used to take a profile through the notch used to initiate crack growth to show crack growth in the sample by highlighting the temperature change created by the plastic deformation [81]. AE was also recording continuously and was useful in detecting cracks during the initial crack growth stages while IRT could only detect the cracks when they were large enough to affect the temperature distribution in the steel sample.

AE and IRT have also been used in the process of manufacturing AM parts [82]. This allowed the detection of defects while the part was being printed such as solidification and fractures. The magnitude of the AE signal could be related to the power of the laser used in SLM, while the IR data provided a better understanding of the conditions forming the AE sources. Lock-in thermography, a similar technique to TSA was combined with AE to determine the fatigue limit of metal matrix composites [83]. Lock-in thermography uses the cyclic temperature response to monitor the surface, but it is not converted to the sum of principle stresses like in TSA. It was found that when loading the sample below the 60% UTS fatigue limit, the heat tracked by the lock-in thermography was able to dissipate. But when loaded above 60% UTS, there is a rapid increase in temperature, and hence energy before the failure of the sample. AE activity was similarly monitored during the test, with a noticeable rise in cumulative AE activity at the same load as the temperature increase. These trends were even more noticeable in the other aluminium sample when the fatigue limit was reached.

Similarly to IRT and AE, TSA and AE have been used together before in composites. In [84], AE is used to detect AE sources in carbon fibre reinforced composites and the findings are validating using TSA. While the methods are not combined per se, they both support each other's findings. A wind turbine blade was monitored using TSA and AE and found that both TSA and AE could identify damaged areas correctly and independently, but the methods were not combined for any post processing[85].

TSA was used to detect cracks in aluminium samples, along with AE to confirm the TSA findings [86]. The crack position was plotted with the AE hits to show a rise in hit numbers that could be correlated with the crack lengthening as seen on the TSA data. Four AE sensors were used on the sample to be able to locate the AE source as seen in Figure 11. This enabled location detection using both AE and TSA. It was found that TSA was more accurate in the position of the crack and enabled the monitoring of the crack growth, while the AE located the events up to 30 mm from the crack. This inaccuracy in locating the AE sources could have been caused by sound dampening in the material, however, AE could detect a crack forming slightly before TSA could. One of the issues presented with the data collection was that the sample used was chosen because it was known to work with TSA. This caused problems with the AE sensors because the sample was relatively small, so the sensors had to be placed close together, reducing the amount of difference between the detection times of the AE events and making the localisation less accurate. TSA and AE were also used to monitor for crack growth in aluminium alloy matrix composites [87]. The two methods were not combined but confirmed each other's results. TSA was monitoring for crack growth in front of the initiation point using a method similar to [78] where multiple parallel lines were used to track crack tip location. This method proved to work well, detecting crack location even when the crack was not visible on the surface of the sample. AE meanwhile captured waveforms using two piezoelectric sensors which showed that RA, energy and rise time of captured waveforms increase 1000 cycles before failure, indicating crack growth. This study proved that TSA and AE can be used to monitor for crack growth.

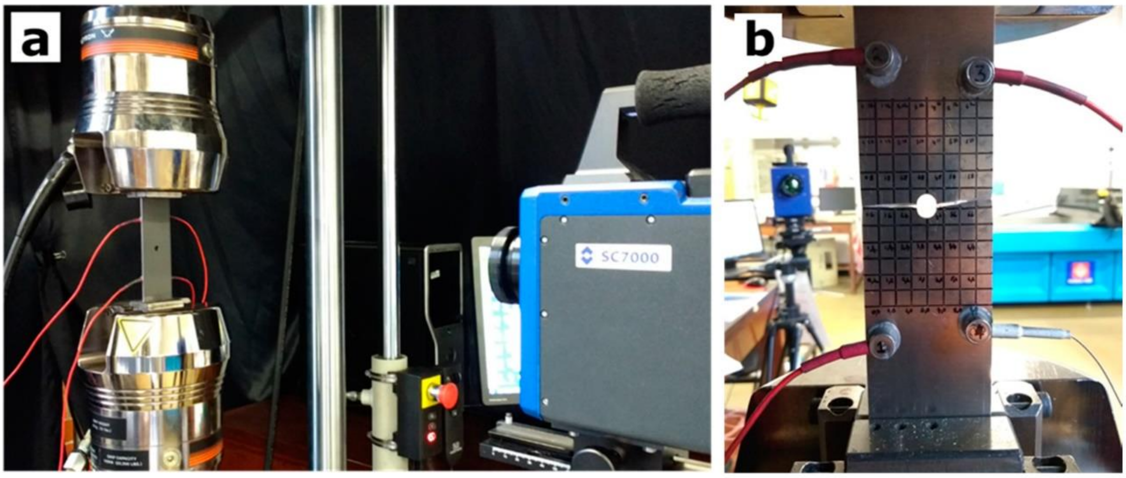

Figure 11. Experimental set-up. Front(A) is TSA collection side and back (B) is AE collection side. Reproduced from [86].

2.5 Summary

The concept of combining AE and TSA together to detect crack growth has not been thoroughly explored. Some work has been conducted with IRT but only limited research with TSA in composites and monolithic metals is currently published. However, both TSA and AE have been proved to be able to detect and monitor crack growth in metals. A gap is present in combining TSA and AE to monitor crack growth in cyclically loaded monolithic metals and AM metals already manufactured. This can could be partially addressed by developing a monitoring method combining both techniques to monitor crack growth in monolithic and AM metals.

Chapter 3

Method

The method used in this research is highlighted in this chapter covering sample design, TSA and AE individual and combined approaches as well as testing parameters and data processing.

3.1 Samples

Four types of samples were used in this research. Type I and II were monolithic metal samples used to develop the test method and data processing before being validated in AM metals using the Type III samples. Once the method was validated, it was used to detect cracks in purpose-built AM samples referred to as Type IV samples. The summary of sample manufacturing method can be seen in Table 1.

Table 1. Sample information.

Sample	Material	Manufacturing method
Type I	Al 5052 H32	Laser cut
Type II	Al 5052 H32	Water jet cut
Type III	AlSi10Mg-0403	SLM
Type IV (notched)	Ti64	SLM
Type IV (plain)	Ti64	SLM

3.1.1 Type I:

The initial samples used were made of aluminium 5052 H32, using a modified ASTM E8/E8M-21 geometry with a thickness of 2 mm and cut using a laser cutter with a 55 mm gauge length as shown in Figure 12. Laser cutting was chosen for the first set of samples because it would be faster and cheaper than a water jet cutter. This sample was used to establish experimental and processing methods required to achieve objective one, detailed in Chapter 1.2.

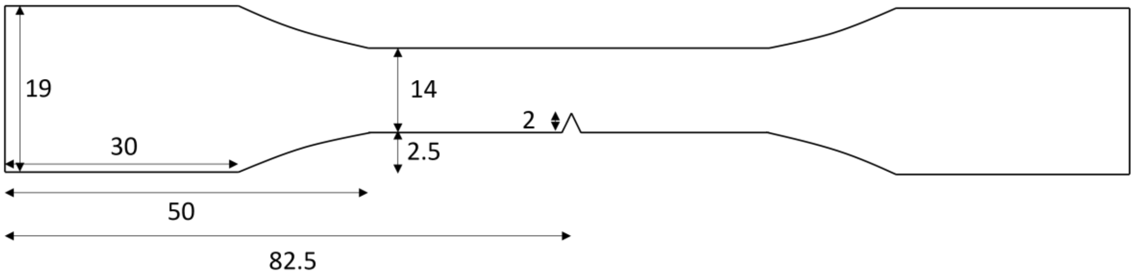

Figure 12. Type I and II dimensions. All measurements in mm. The right-hand side is mirrored on the left-hand side. Not to scale.

3.1.2 Type II:

These samples used the same geometry and material as Type I samples but were 4 mm thick and cut using water jet cutting. The samples were made thicker to increase the required fatigue load as the lower load was close to the lower limit of the machine used to cyclically load the sample. Waterjet cutting was chosen to minimise the localised heat treatment caused by the manufacturing process. These samples were used to achieve the second objective as laid out in Chapter 1.2.

3.1.3 Type III:

The third type of samples was made of SLM manufactured aluminium using AlSi10Mg-0403 aluminium alloy powder, dimensions can be seen in Figure 13. Type III samples were existing samples provided by collaborators at Cardiff University. The geometry was sufficient to satisfy the third objective laid out in Chapter 1.2 as it did not impact testing or data collection. A 2mm deep notch was cut in the centre of the gauge length using a handsaw to provide a known crack initiation point. Thickness of the sample is 2 mm. The printing parameters for these samples are unknown.

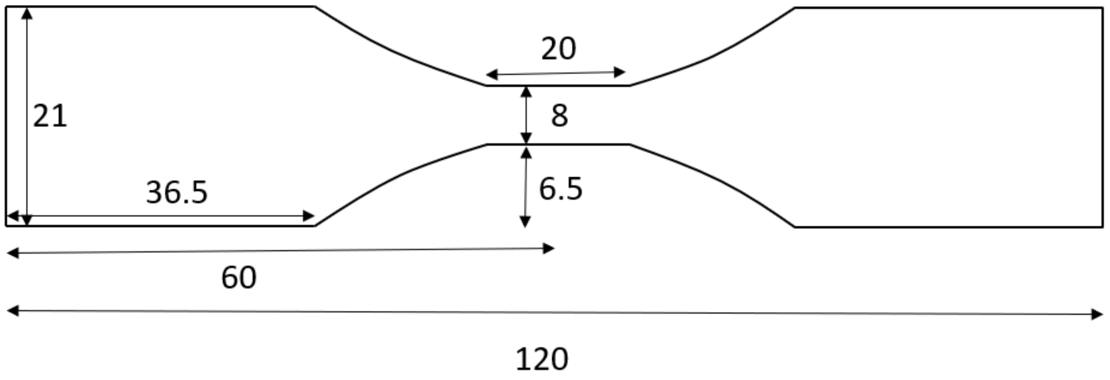

Figure 13. Type III samples. Right-hand side is mirrored on the left-hand side. All dimensions are in mm. Not to scale.

3.1.4 Type IV:

The final samples used in this research were additively manufactured using SLM with Ti64 and the same dimensions as Type III samples but 3 mm thick. The reason for the change of thickness was the same as the Type II samples, the thicker samples could sustain a higher load to avoid the lower limit of the cyclic loading machine. Notched Type IV samples were used to confirm the method in a new material, then plain samples without defects were tested to demonstrate that the proposed method can be used to detect and monitor crack growth in notched SLM printed samples and in samples with no notch as laid out in objective four in Chapter 1.2. The samples were printed using a SLM printing machine with a laser scanning of 1200 mm/s, laser power of 190 W, layer thickness of 30 µm and energy density of 52.8 J/mm^3.

3.2 TSA set up and operation

To prepare the sample for TSA, the surface was cleaned with isopropyl alcohol, then painted with Colour Lab Premium Matt black enamel spray paint. This paint was chosen because it had the highest emissivity value, and it was readily available [88] . The paint coating should be approximatively 15 to 25 µm thick or approximatively “two passes”. If the coating was too thick, it would cause heat dispersion in the paint, too thin would not stop reflections [88]. The paint thickness was checked with a paint thickness gauge to be within the previously mentioned range. The samples were placed in the machine grips, as shown in Figure 14, with the painted surface facing the camera.

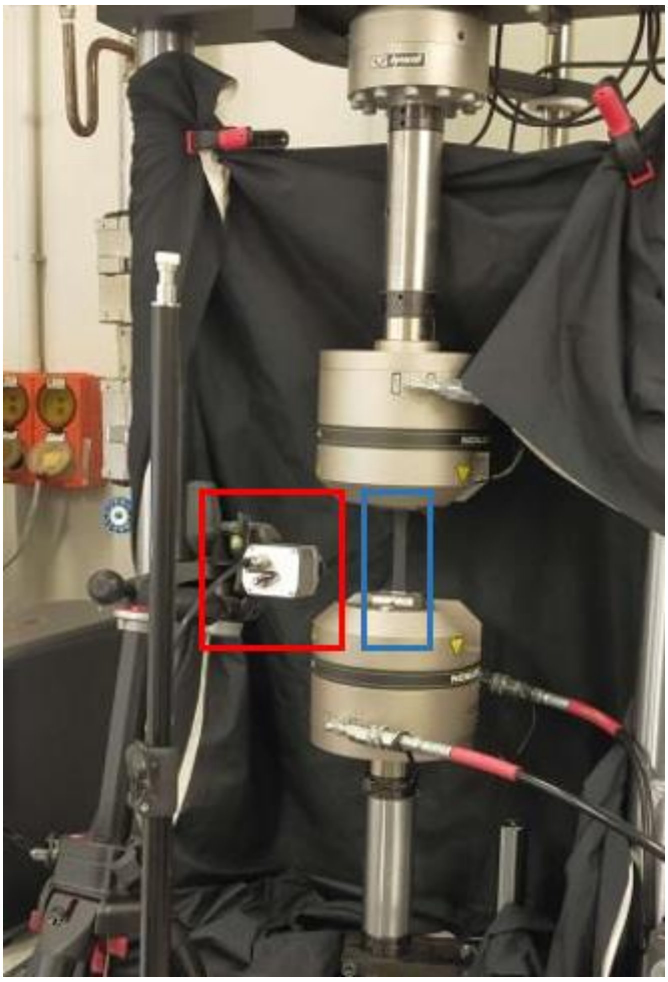

Figure 14. TSA set up in the test machine. Red box highlights the IR camera; blue box highlights the sample in the machine grips.

The test machine used for this work was an INSTRON 8801 servohydraulic machine with 100 kN load cell. The camera was installed sideways on the tripod to increase the number of pixels along the length of the sample, with a camera to specimen distance of 120 mm, providing a horizontal field of view of 64 mm and a resolution of 7.5 pix/mm. The horizontal FOV is rotated in Figure 15. The camera used was a Optris 640PI microbolometer with a 30° lens. The manufacturer's software PIX connect was used as interface between the camera and Matlab to collect the raw footage. The thermal sensitivity of the microbolometer is 40 mK, specification sheet for the camera can be found in Appendix A. The settings used for this experiment were 125 Hz frame rate with a sub-window of 120 x 480 pixels and a recording time of 30 seconds. The recording time is discussed in Chapter 3.4.1. The recordings starts when the oscillations of the hydraulic machine are stable, this is usually 30 seconds after the cyclic loading begins. The raw data collected by the microbolometer is processed in Matlab using a lock-in algorithm, using the loading frequency as the reference signal. This processing outputs an image showing the sum of the principal stresses with Eq(1) and phase distribution on the surface of the sample as seen in Figure 15. The phase data shows the phase of the stress and if the surface stress is in compression on tension. The current research focused on using the stress data.

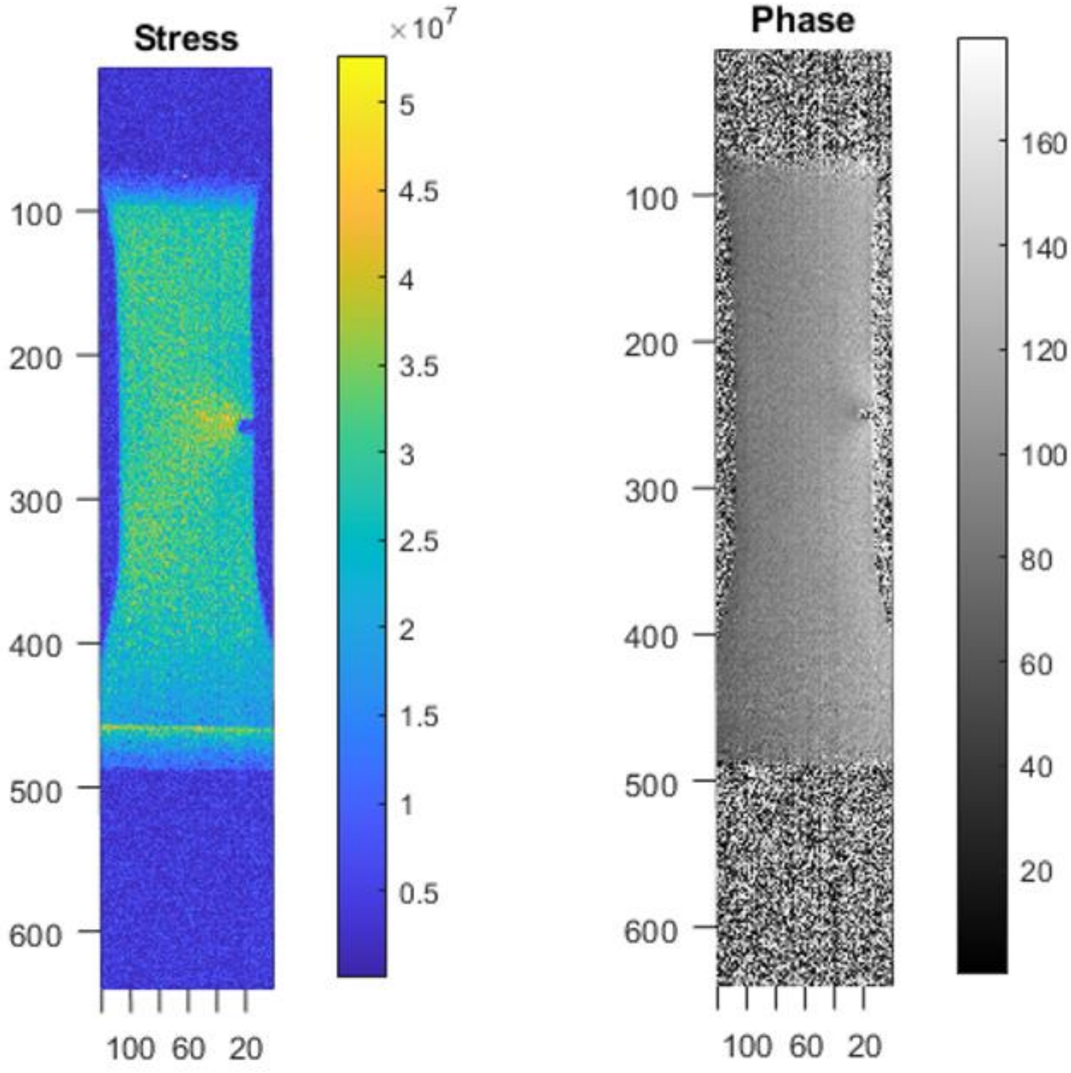

Figure 15. Example of phase and stress output of TSA from a Type III sample. Stress is in Pa and Phase in °.

3.3 AE set up and operation

The AE equipment was set up as in Figure 16. A Picoscope 3425 was used to collect the AE data along with a Mistras 2/4/6-C preamplifier and Nano-30 piezoelectric sensors. The specification sheets for the Picoscope and piezoelectric sensors can be seen in Appendix B and C respectively.

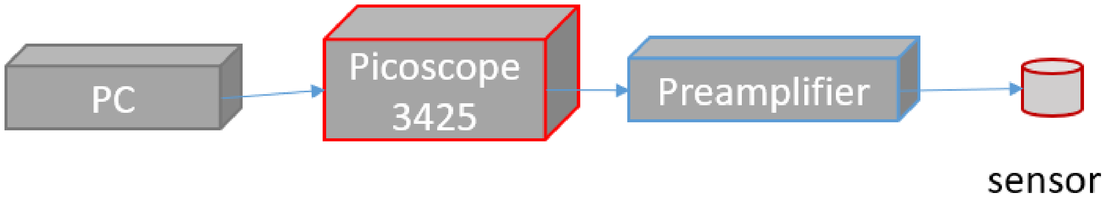

Figure 16. AE setup

In early experiments using Type I samples, the sensor was attached to the sample by applying a bead of ultrasound gel between the sensor and the surface so the signal can freely move from the surface to the sensor, it was then held in position using electrical tape. The sensor was placed on the back of the sample from the IR camera point of view with the tape looping around the sample to attach it. During the first tests, the AE sensor was placed as far away from the notch as possible while still being on the gauge length of the sample to avoid obscuring the surface of the sample for the IR camera. However, a better method to attach the sensor to the sample surface started being used while testing Type II samples which involved placing a 5 to 10 mm bead of Loctite 595 clear RTV sealant to the surface and gluing the sensor, with a curing time of 24 hours. The sensor should be slid in place to avoid bubbles and have a thin film of glue between the surface and the sensor. The thickness of glue needed between the surface and the sensor was investigated in Chapter 4.4.2. This method of attaching the sensor to the surface is advantageous over the original method because it eliminates the need to tape the sensor which obscures the view of the IR camera. To ensure the sensors were attached properly, a pencil lead break test (PLB) [58] was conducted for each new sensor attachment, and the results recorded. If the resulting amplitude was under 95 dB, the sensor was removed, cleaned and glued again. The layout of the sample can be seen in Figure 17.

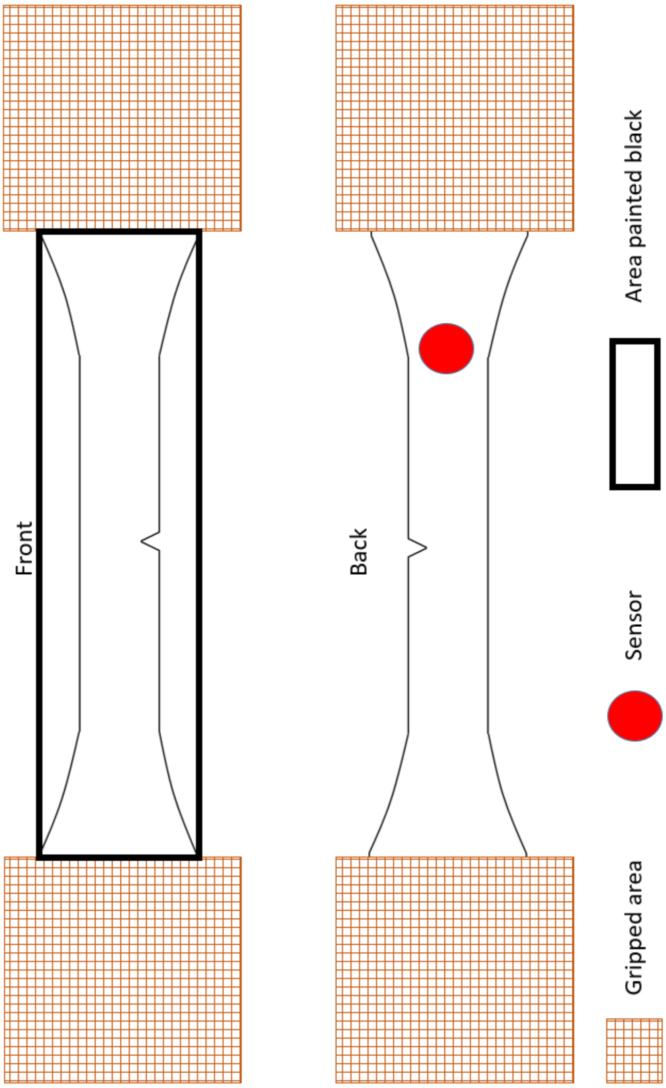

Figure 17. Layout of sensor with painted area and gripped area on sample.

AE was recorded with an automatic threshold that filtered noise; in most cases the threshold value was 35 to 40 mV. This value was determined by raising the threshold at the start of the cyclic loading before a crack was present until no machine noise was detected, this was done to reduce machine noise during testing. A crack is expected to grow in rhythm with the cyclic loading and show a higher amplitude than the noise created by the loading. The sampling rate was 1 MHz.

3.4 Preliminary testing

Preliminary testing was used to determine test parameters for cyclic loading, TSA and AE.

3.4.1 TSA

A series of preliminary tests were conducted to establish testing parameters to be used for TSA data collection. Firstly, the optimal loading parameters for TSA to detect the growing crack must be determined.

3.4.1.1 Loading frequency and range

The loading frequencies seen in Table 2 were applied to the sample and the consistency of the TSA response was assessed using the Type I samples with their surface prepared for TSA as presented in Chapter 3.2. The greater the difference between the loading frequency and the recording frequency, the more data points available for TSA analysis, therefore it is important to establish what the slowest acceptable loading frequency is. However, the loading frequency must not be too slow or else conditions cannot be assumed to be adiabatic. Once a loading frequency was defined, the load range was changed to determine the lowest load range at which stress is detectable with TSA using the current system. The ideal load range would create progressive failure that can be monitored with a slow crack propagation rate. The maximum number of tests per day is three due to AE equipment restrictions and this could be repeated three times per week due to glue curing time for the AE sensors, therefore being able to test three samples per day is ideal.

In total, 14 Type I, 12 Type II, 6 Type III and 5 Type IV were tested. Table 2 presents the tests conducted using Type I samples to determine the optimal load range and loading frequency. The load range would be used to load all samples to failure. The specified load ranges were chosen because they were expected to initiate crack formation as well as crack propagation at a rate that would enable three samples to be tested in one day but also provide regular data capturing over a length of time to replicate continuous monitoring. Multiple loading frequencies were also tested to determine which one would work best for TSA data capturing and processing. This loading frequency will be used for all testing going forward. Literature stated that a loading frequency of 20 Hz would be ideal for TSA in some applications, but other frequencies were also tested to determine if it was suitable for this application. The samples were tested with a loading range of 10 to 40% of their ultimate tensile load (UTL) at different frequencies to determine the optimal loading frequency. Once the loading frequency was chosen, samples would be tested at different loading range with the same frequency to determine which load range would be adequate for the rest of testing.

Table 2. Preliminary tests to determine future test parameters.

		Load frequency (Hz)				
		5	10	15	20	25
Load range (% of UTL)	10 to 20				x	
	10 to 30				x	
	10 to 40	x	x	x	x	x
	10 to 50				x	
	10 to 60				x	

To determine the ideal loading frequency, a stress profile was taken across the notch of samples tested at different frequencies and were plotted in Figure 18. The ideal loading frequency is the one that shows the slowest frequency where the stress profiles converge. It was found that the stress profiles across the notch obtained using TSA converged at 20 Hz as seen in Figure 18, this frequency value is supported by TSA literature [22] for some cases depending on loading and other factors. Below 20 Hz, adiabatic conditions cannot be assumed for the sample, above 20 Hz the sample would be damaged rapidly, preventing monitoring over a longer period of time. This means that because the IR camera can sample 6.25 times per cycle, which satisfies sampling criterion.

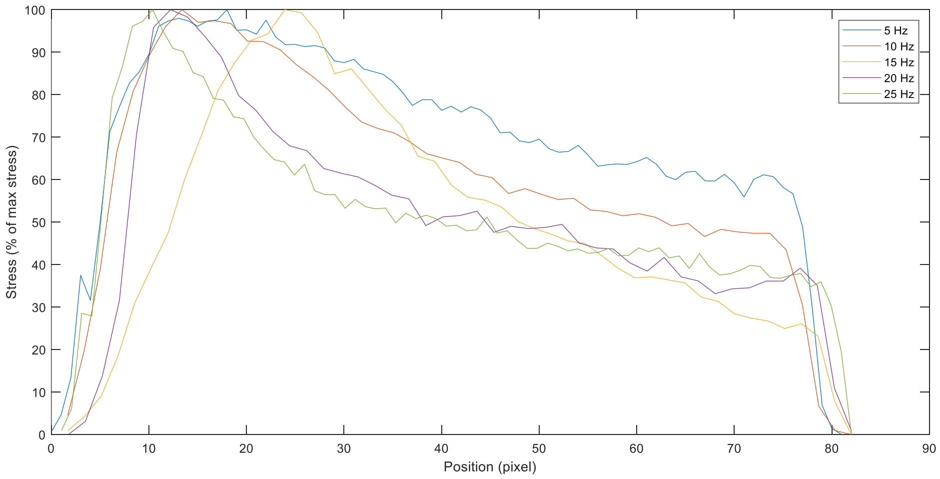

Figure 18. Stress profiles through the notched Type I samples using different loading frequencies.

Loading using 10-50% and 10-60% of the ultimate tensile load found using tensile testing caused the sample to break suddenly without showing a growth in AE activity for Type I samples. The chosen load range was 10-40% of the UTS because it created progressive failure over a reasonable timeframe, typically within 30 mins of the start of the test. Based on the UTL of each sample type, the load ranges for each sample can be seen in Table 3.

This loading was later increased to 20-50% from the waterjet-cut Type II samples onwards to reduce testing time to under 250 000 cycles as 10-40% would take over 400 000 cycles before a sample would start displaying crack growth. The need to alter the loading between sample types was due to the waterjet-cut notch being rounder than the laser-cut notch, causing a lower stress concentration. Increasing to 20-50% UTL means the loading amplitude remains the same but with a higher mean load. The mean load on the notched Type IV samples was calculated using the UTL of the notched samples, not the plain sample. When the samples failed, they failed close to the same cycle count, meaning the first cycles could be accelerated to a higher frequency to increase cycle count rapidly before slowing to monitoring frequency at 20 Hz for data capture and crack growth monitoring. The loading sequence began with a ramp to the mean load, before cyclic loading was applied until failure.

Table 3. Load range by sample type.

Sample	Load range (kN)
Type I	2.2 ± 1.3
Type II	3 ± 1.8
Type III	1.7 ± 0.7
Type IV (notched)	1.5 ± 0.5
Type IV (plain)	6.35 ± 3.85

3.4.1.2 TSA capture length

The initial recording time for TSA was 60 seconds at the specified recording frequency and is driven by data capacity. The microbolometer used could record in either 32Hz (full frame) or 125Hz (windowed). The latter was chosen to increase data collection rate to fit the Nyquist requirement of the sampling frequency being at least double the loading frequency. The total data collected on the system used is limited by RAM size, a limit of 432 000 000 pixels can be recorded at a time, requiring a compromise between sampling rate and window size. The sampling time could be increased by reducing the sampling frequency or windowing the frames. Sixty seconds was the longest sampling time possible with the available hardware without reducing the sampling frequency or windowing down the image further. Saving the raw footage after recording takes approximatively the same amount of time as the recording, so TSA could be recorded every two minutes for one minute at the fastest. However, being able to reduce the recording time, and hence, the saving time would greatly benefit the data collection process, meaning that data could be recorded more frequently. Therefore, the shortest recording time that still provides accurate data, once processed into TSA data, should be used.

The shortest recording time was found by extracting a profile through the notch in a set of processed data from a cyclically loaded Type I sample with a 60 second recording time, referred to as the original set. The original set was cut into 50, 40, 30 and 20 second length processed recordings. Using the same profile data from all processed recordings, the average difference between the original and each of the shorter recordings was noted. This was repeated with four other Type I data sets showing the profile through the notch, the difference between the original 60 second profile and the shorter recordings was averaged, the results are shown in Table 4. Shortening the recording to 50 seconds introduces a 1.91% error and 40 seconds introduces 4% error. Halving the recording time introduces 6.25% error while shortening it by 40 seconds introduces 11.1% error. The error almost doubled between 30 and 20 seconds indicating diminishing returns so shortening the recording by 30 seconds were chosen. Using the 30 seconds recording time instead of 60 seconds effectively doubled the possible TSA data capture rate which increased the spatial as well as temporal resolution when tracking crack growth.

Table 4. Error between original 60s TSA recording and shortened recordings.

Recording length (seconds)	50	40	30	20
Difference compared to original (%)	1.91	4	6.25	11.1

3.4.1.3 Polynomial fitting

To process the stress profiles across the notch of the Type II samples, a seventh order polynomial was fitted to extract the peak location. However, seventh order polynomial was complicating to processing and the optimal polynomial order should be determined to provide as accurate a peak stress location as possible, without unnecessarily adding complexity to processing. To this end, multiple polynomials of different orders were fitted to a profile from a Type III sample, the results can be seen in Figure 19. The polynomial fit can be seen to converge from the fifth order polynomial; therefore, it was chosen to process TSA profiles. This polynomial was used for the Type III and Type IV sample processing.

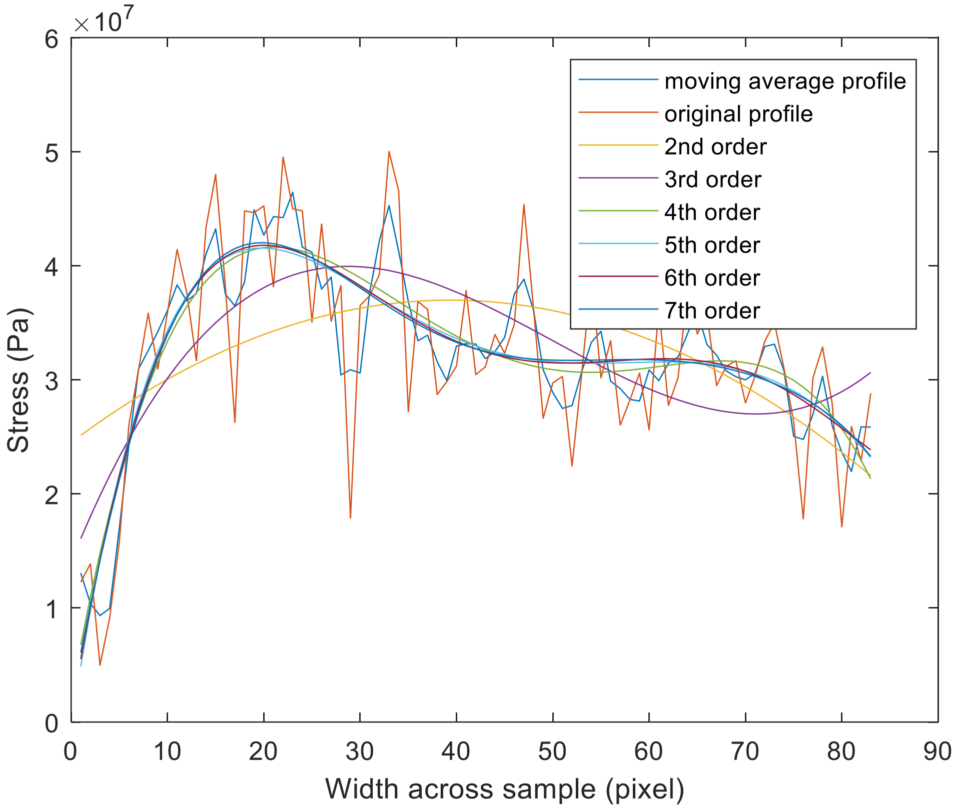

Figure 19. Different polynomial fit on Type III data to determine optimal order of polynomial.

3.4.1.4 K coefficient

Another variable used in the TSA processing is K, it is used to translate the cyclic temperature response from the cyclic loading into stress in TSA, it is a material dependant parameter and can be calculated using Eq(2) and known material properties obtained from [89; 90]. The K values for all samples can be seen in Table 5. The stress calculated using the K value was validated using theoretical calculation, stress in areas with no defects were compared with calculated stress using loading and sample area.

Table 5. K values used to process into stress in TSA.

Sample	K value
Type I	$9.68e^{-12}$
Type II	$9.68e^{-12}$
Type III	$9.68e^{-12}$
Type IV	$3.53e^{-12}$

3.4.2 AE

For all tests, with the exception of Type IV samples, the sensors were glued by hand with no thickness control, however, some samples displayed a smaller amplitude when performing a PLB. To remove the possibility of glue thickness introducing error in AE data, multiple thicknesses were tested. To do this, a 0.9 mm thick sheet of aluminium was fully clamped between two rectangular steel frames and bolts with a torque of 42 Nm fastened the aluminium sheet between the frames. Three sensors were then glued at the centre of the sheet and PLB tests were performed at known distances from each sensor one at a time. The apparatus used in this experiment can be seen in Figure 20.

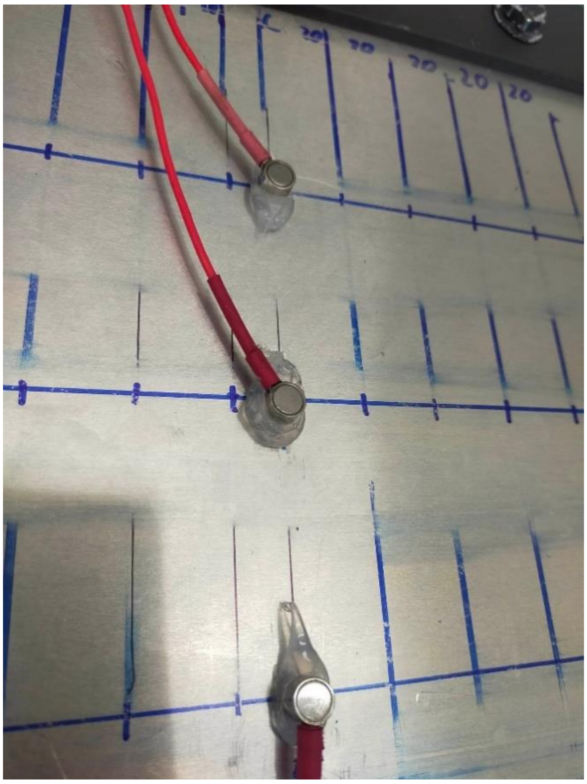

Figure 20. AE sensors glued on metal sheet to determine the optimal glue thickness.

The glue thickness was controlled by placing shims of different thicknesses under the edges of the sensor as seen in Figure 21. This was repeated with 4 different thicknesses and the results are displayed in Figure 22. The free hand glue thickness was between 0.08 mm and 0.25 mm thick.

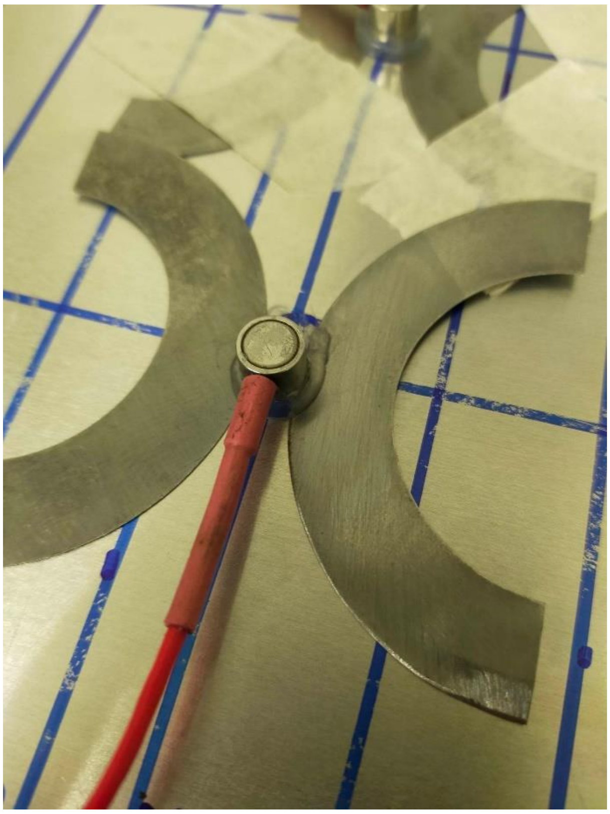

Figure 21. Shims placed underneath the AE sensor to control glue thickness.

It was found that gluing with the shims introduced error in the form of air bubbles due to the difficulty in ensuring the sensor was sheared into place and inadequate glue covering surface where the glue did not spread evenly under the sensor. The quality of the gluing proved to have a much bigger impact than the thickness, with the free hand glue showing consistently higher amplitudes compared to the same 0.25 mm thickness glue with the shims and the other glue thicknesses seen in Figure 22. Uniform glue thickness and the absence of bubbles under the sensor is an indication of good gluing quality. It was decided to focus on shearing the sensor into place properly to avoid air bubbles and using enough glue to provide adequate covering in future tests rather than glue thickness.

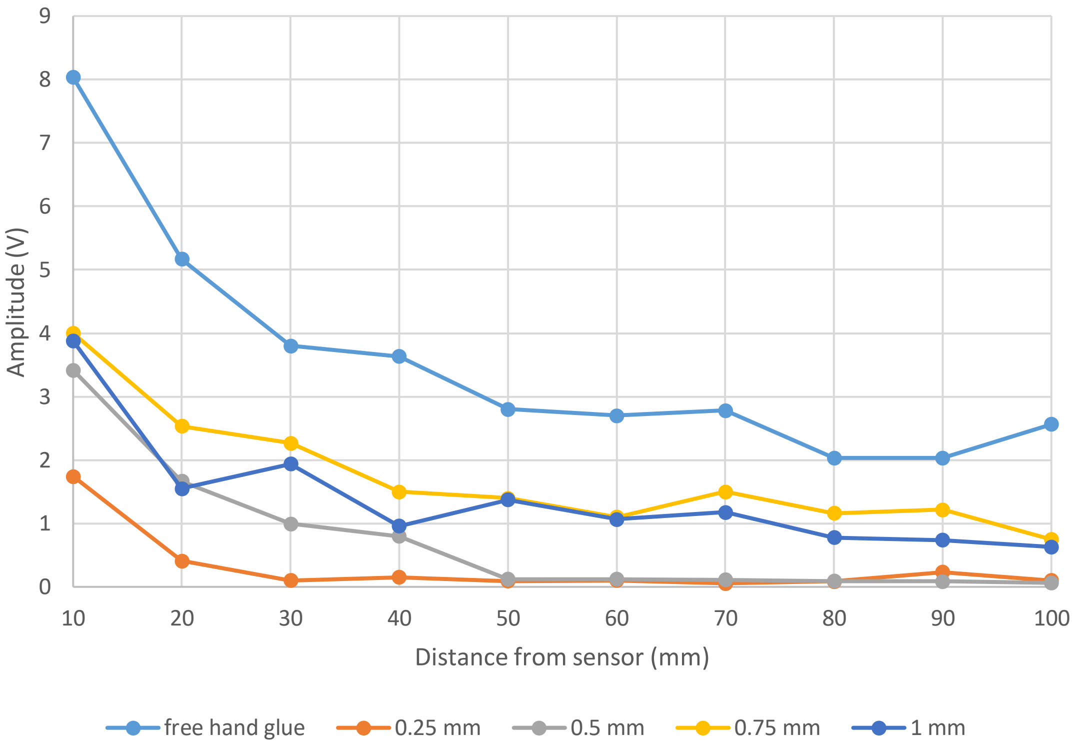

Figure 22. Effects of glue thickness on signal amplitude.

3.5 AE and TSA combined set up and operation

The combined set up was like the individual TSA and AE set ups. Two laptops were used to record the data, one for AE and the other for TSA. The AE sensor was placed on the opposite side of the sample from the camera with the PLB tests performed on the back of the sample near the notch. The position of the PLB was chosen to determine the amplitude of signals generated at the approximate location of the expected crack growth. The PLB was performed on the back side of the sample to not damage the matt black paint on the front. AE recorded continuously while TSA recorded every 10 minutes until AE activity is detected, in which case TSA is recorded every 30 seconds until the sample fails. AE waveforms are saved automatically, immediately after capture with an associated time stamp. Similarly, the TSA data was timestamped upon capture.

3.6 Data processing

Each 30 second TSA recording is converted into a single frame with the stress and phase using the theory discussed in Chapter 2.2.1 and the thermoelastic coefficient K calculated from material properties as seen in Chapter 3.4.1.4 [22] .

A profile is then extracted through the notch as seen in Figure 23, this is done by taking a line three pixels wide from the centre of the notch to the opposite side of the sample horizontally in Figure 23 and averaging them to reduce noise. Three pixels wide was chosen because it would reduce the chance of a single pixel introducing a large error while not widening the profile past the notch into the neighbouring material. The results of the averaging can be seen in Figure 24. This method of taking a profile through the notch was used in [81] and proved to work well to detect linear crack growth originating from a notch.

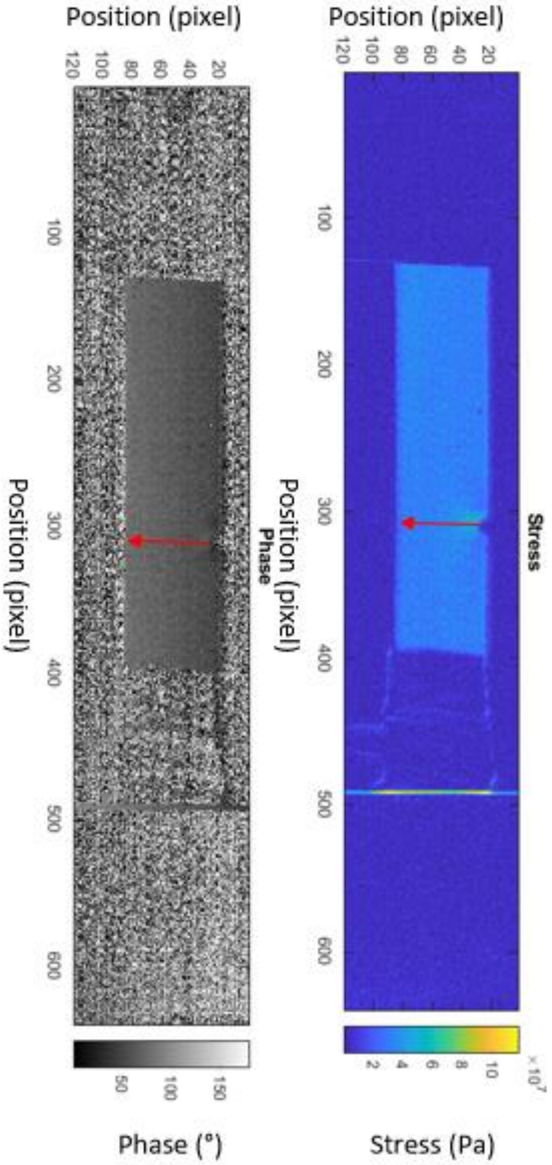

Figure 23. Example of the sum of the principal stress and phase data from TSA. Red arrow is the position and direction of notch profile.

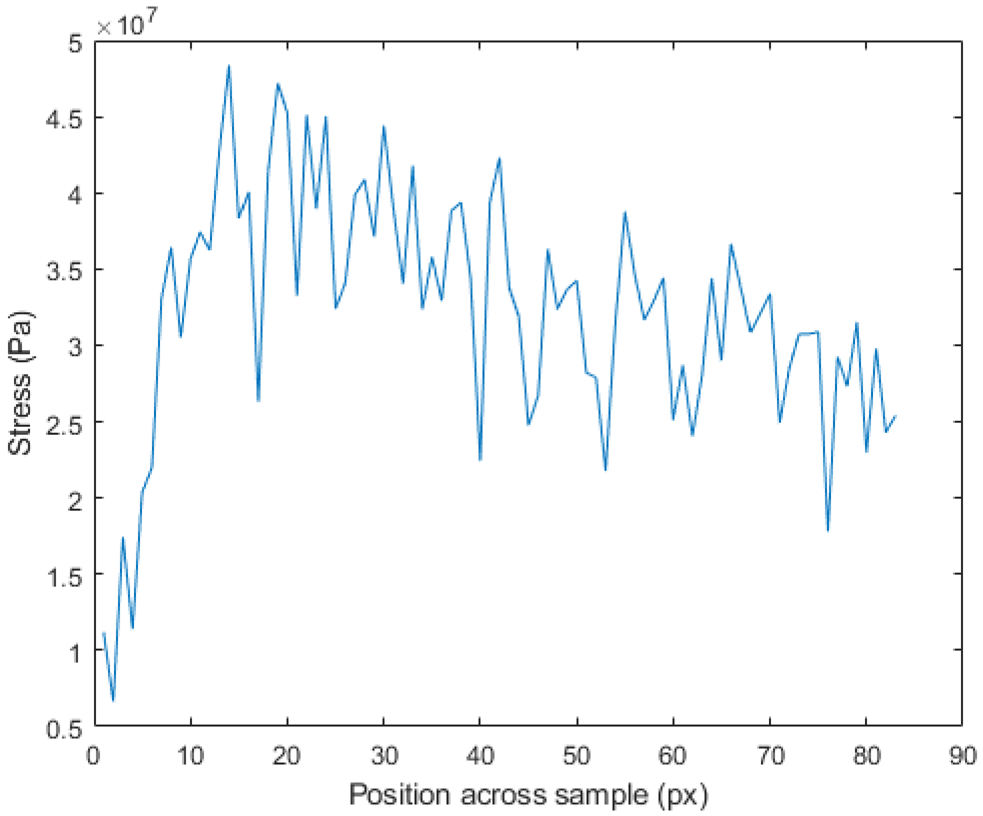

Figure 24. Stress profile through the notch obtained by TSA.

A three-point moving average is applied to the profile to smooth it and to remove any possible error from a rogue pixel as seen in Figure 25.

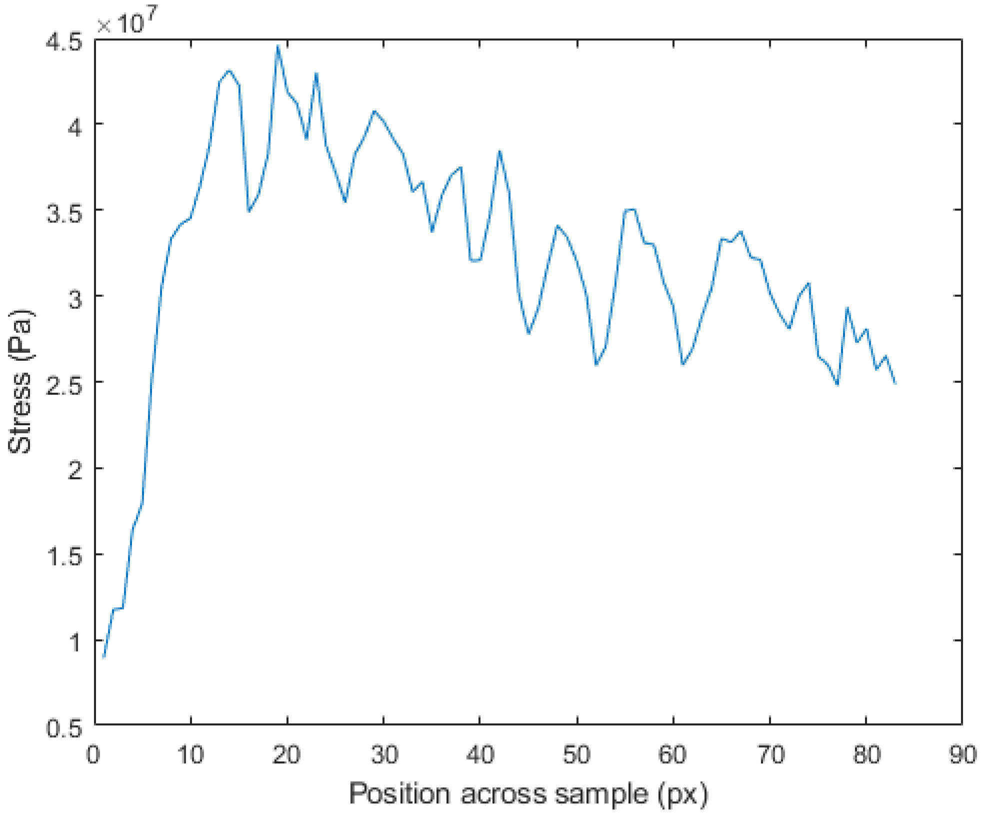

Figure 25. Profile across sample after moving average was applied.

It is worth noting that TSA detects the peak stress location as opposed to crack tip location. The peak stress is found in front of the stress concentrator i.e., the notch or the crack tip, but there will be a small space between the crack tip and peak location due to the fracture toughness of the material, this is discussed in Chapter 4.2.2. Therefore, in Figure 26 the peak location is at 1.5 mm or 11 pixels at the start as opposed to crack tip location at 0 mm when there is no crack present. This is indicated by a red dot in Figure 26.

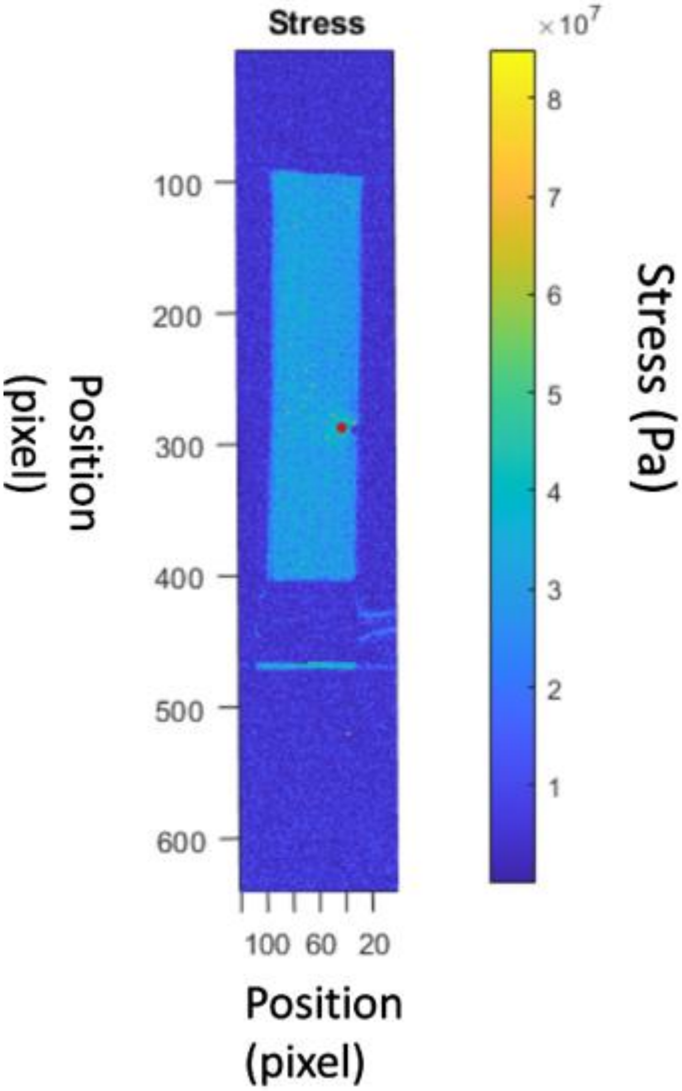

Figure 26. Peak location (red point) in front of notch.

The location of the peak stress is then extracted from each profile by fitting a 5th order polynomial to the notch profiles and gathering the peak stress location, as detailed in Chapter 3.4.1. The amount of stress is not required, only the peak location. However, it was found that fitting the polynomial affected peak location accuracy by 4-5 pixels or 0.3 mm when comparing polynomial peak location to the manual peak chosen by the operator. The small error was judged acceptable as crack length usually exceeds 2-3 mm. Should it be found to be required, a more accurate crack position could be found using a higher resolution IR camera and is discussed in Chapter 5.2.2.

The peak stress location is then plotted through time to visualise the crack tip progression across the sample as shown in Figure 27.

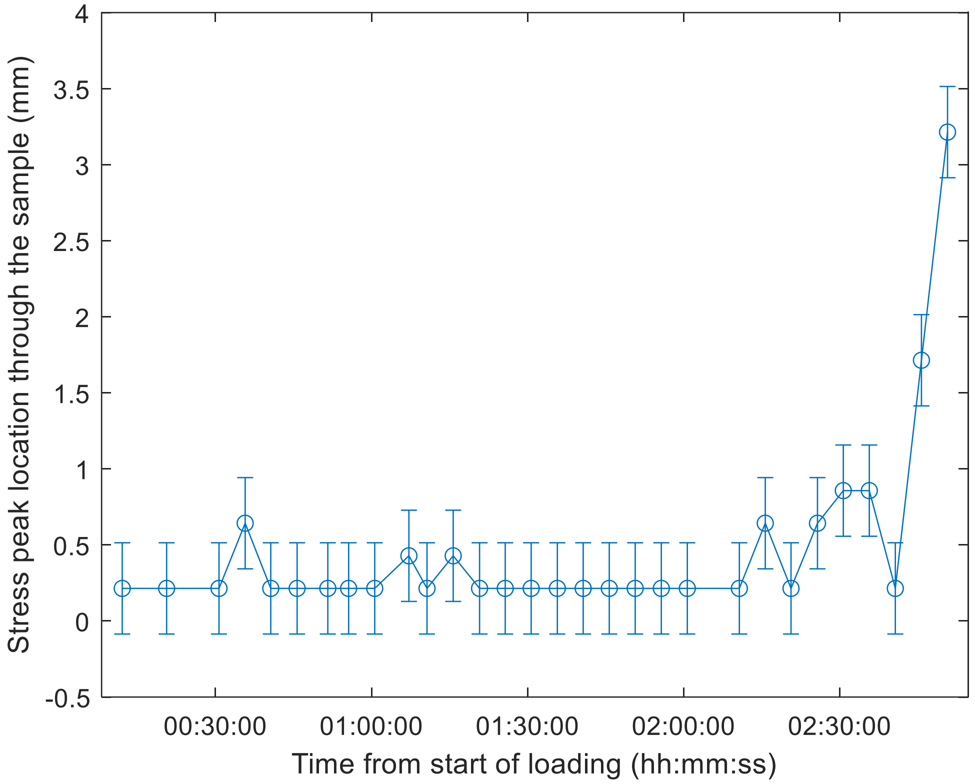

Figure 27. Crack tip location through time obtained using TSA.

The reason why the peak location seems to be moving in the first two hours is because of the camera thermal sensitivity. There is no crack until 2:10 hours and the peak stress should not be moving. When combining the error introduced by the IR camera's sensitivity with the error introduced by the polynomial the error is 0.3 mm, this is the error shown in the figures presented in this thesis.

The AE waveforms were saved with a timestamp as soon as a hit was detected that crossed the threshold value. The energy released by the AE event can be obtained from each waveform by performing the RMS of the waveform, RMS was chosen as it was effective when calculating the energy released, as shown in literature [64]. The number of hits in each waveform can also be counted by applying a threshold to the data, any peak above the threshold is considered a hit. Both number of hits and energy can be timestamped with their waveform and then their respective cumulative totals plotted through time as seen in Figure 28 and 29.

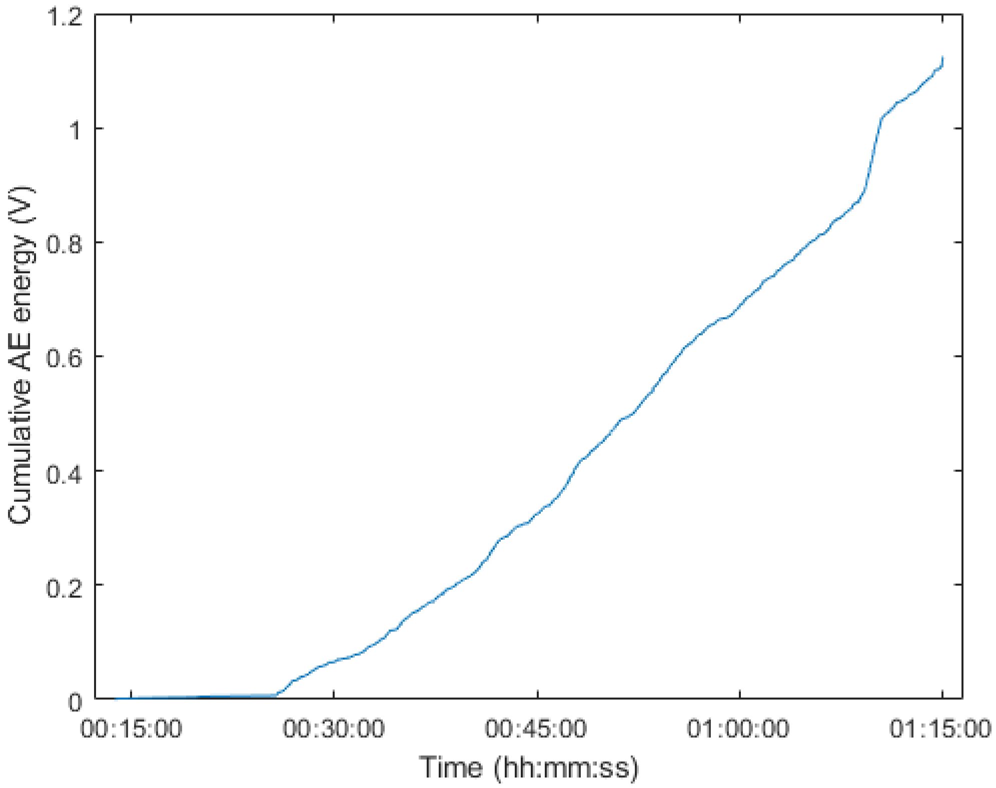

Figure 28. Cumulative AE energy

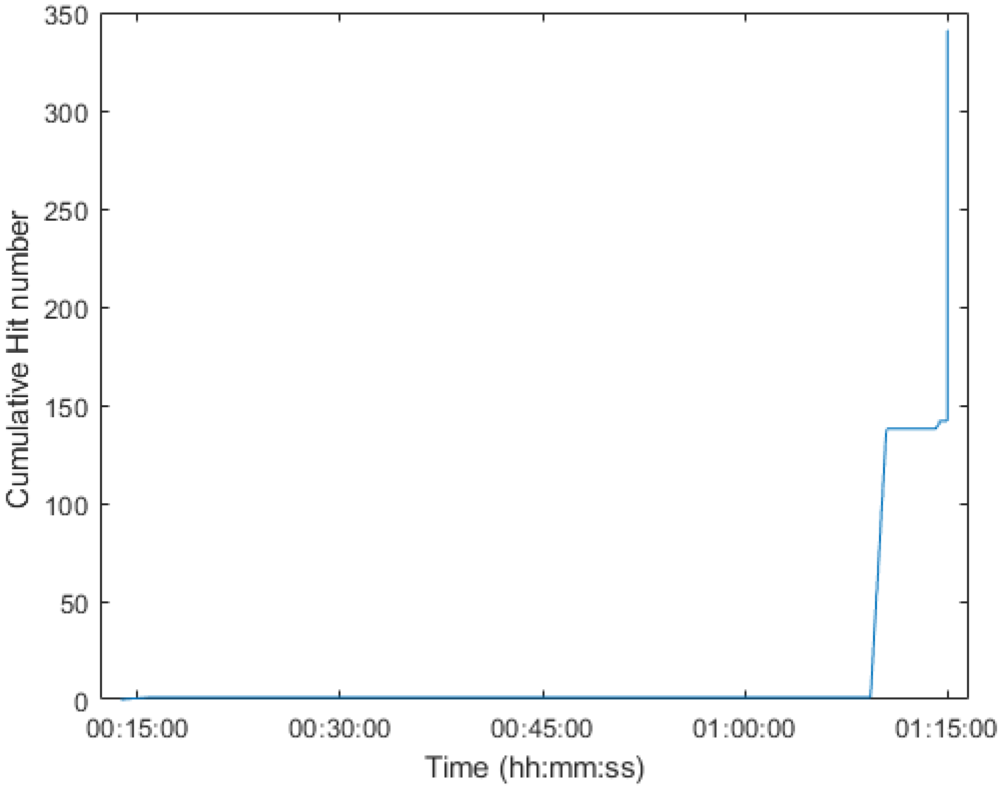

Figure 29. Cumulative AE hit number.

TSA and AE results can then be combined on a common timeline for direct comparison as in Figure 30. The data plotted in Figure 30 show that in this case both techniques detected crack growth at the same time. TSA shows the peak stress location which is in front of the notch or crack after it initiates, a crack is detected when the crack length increases by 1 mm. The IR capture frequency can be increased to provide a higher spatial and temporal resolution for crack growth. The AE energy is the energy collected from each waveform, a sudden increase in gradient indicates creation of new surface area and therefore crack growth. This study focusses on the energy released rather than hits. This shows that both methods detect a change in trend at the same time as seen in Figure 30.

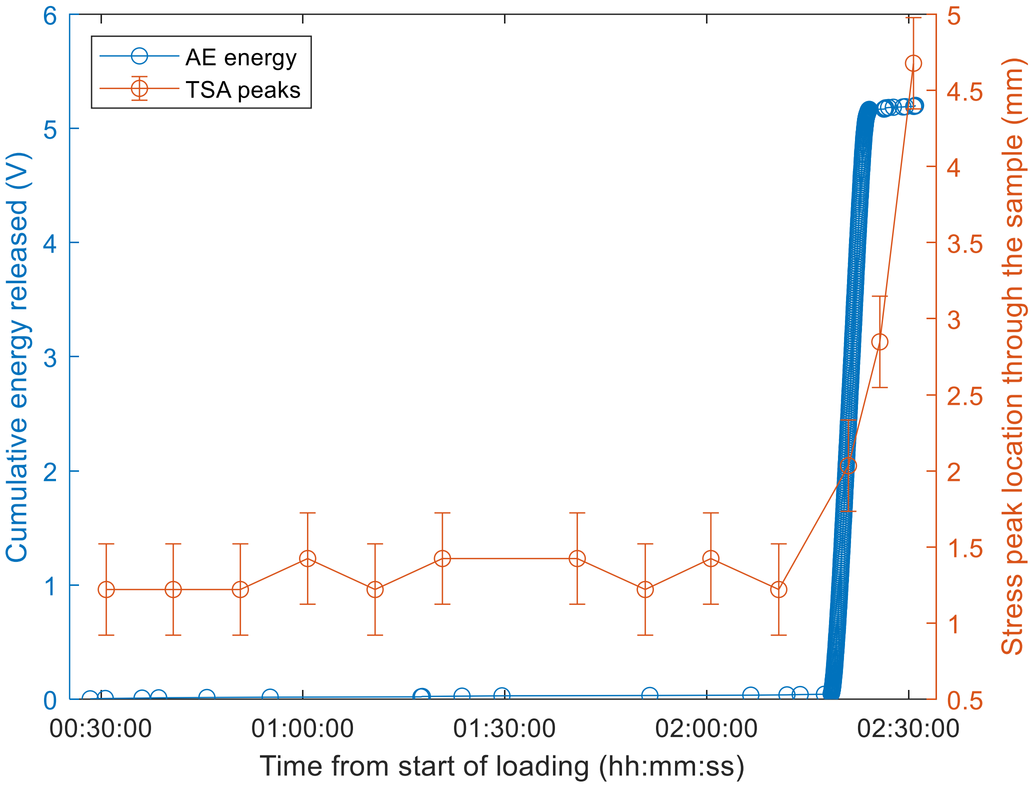

Figure 30. Combined TSA and cumulative AE energy.

This processing method was used to process the data collected from all samples presented in Chapter 4. Possible improvements were discussed in Chapter 5.2.

Chapter 4

Results and discussion

Four types of samples were used in this study to achieve the objectives laid out in Chapter 1.2. Type I samples were used to achieve Objective 1 by enabling TSA and AE to be applied to simple samples to establish independent test and processing methods along with determining testing parameters. Type II samples were used to achieve Objective 2 which involved refining the independent techniques and combining them on samples to improve the test method data processing. Type III samples were used to achieve Objective 3 where the combined method was further refined and applied to AM samples. Finally Type IV samples were used to demonstrate the method can be applied to AM samples with built-in notches of a different material. Objective 5 can be achieved in the future with built-in subsurface defects in Type IV samples using the same manufacturing method and is discussed in more detail in Chapter 5.2.

4.1 Monolithic aluminium results

4.1.1 Type I samples: laser cut aluminium

Early test results using the Type I laser cut, notched samples and a simplified method were promising, AE and TSA were able to detect a crack initiated in a known location. These tests were also used to determine test parameters as discussed in Chapter 3.4 and will not be discussed in this Chapter. The tests with Type I samples used to detect crack growth were successful and one test result can be seen in Figure 32. The TSA peak stress location is shown in orange, this is the location of the peak stress ahead of the notch or crack between the notch and the opposite side of the sample. AE energy shows the cumulated AE energy detected throughout the test; it is indicative of the crack activity. Crack initiation can be seen by the sharp change in trend in AE energy detected at 8 minutes as well as change in the TSA stress peak location after 9:30 minutes in Figure 32. These results demonstrate expected behaviour and are representative of future test results. The system error for TSA is 0.3 mm, it is not applied to this dataset because it is one of the first datasets collected. The increase in peak location between 9:30 and 11 minutes is 1.4 mm so it would still be detected even with the 0.3 mm error. The crack seems to be shortening in length between 2 min and 6:30, however this is not physically possible and is an artifact of the processing due to the TSA error. There is no crack present until after

8 minutes in this sample. The crack growth is detected by AE first, the energy released indicates that new surface area is being created, this is also seen in TSA where the crack length is increasing. In this initial test AE data was binned into three-minute periods, these time periods were chosen to match the frequency of TSA recordings. The sum of these three-minute binned windows was then plotted. This reduced the resolution of the plotted data however it was sufficient for preliminary tests. The goal of these tests was to determine if TSA and AE could be used to detect crack growth, not to collect accurate data, in this they proved successful, although this was refined in tests using Type II samples.

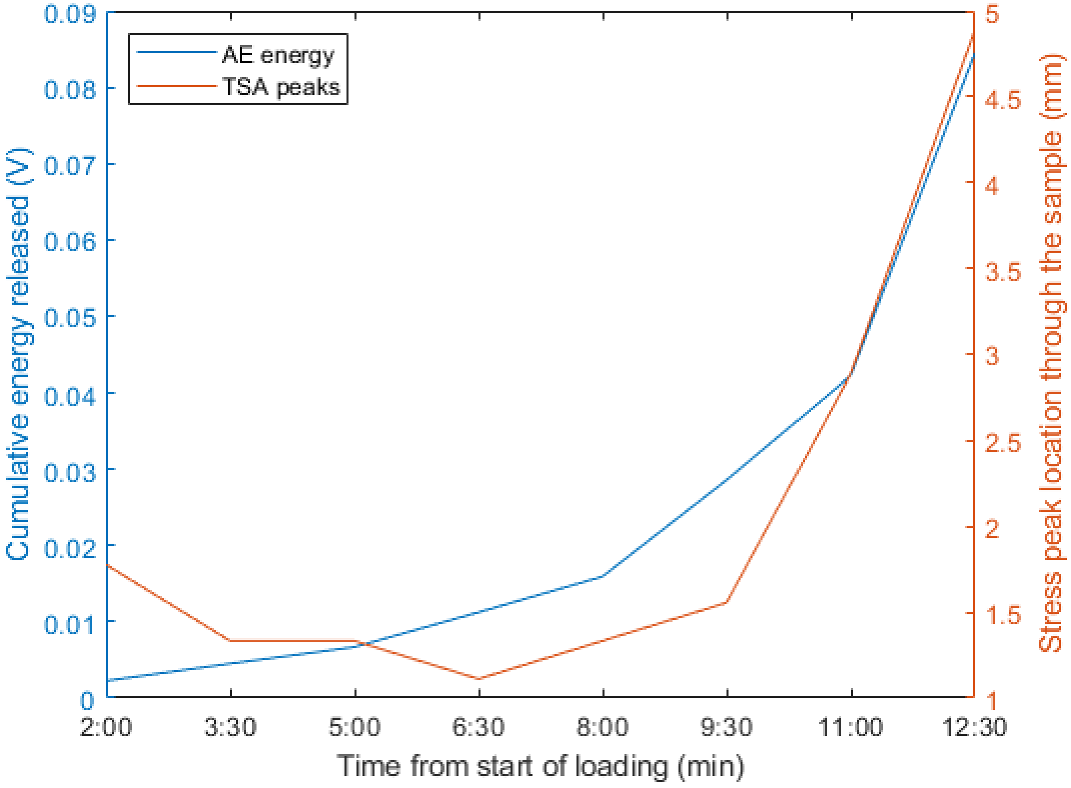

Figure 31. Combined AE and TSA results Type I - Test 5 samples.

4.1.2 Type II samples: Waterjet cut aluminium

The following tests using Type II samples were used to further develop and refine the individual TSA and AE techniques as well as developing a combined method using both techniques.

Table 6. Type II sample result summary.

Sample number	Time of TSA detection (h:mm)	Time of AE detection (h:mm)	Time of failure (h:mm)	Comment

1	1:20	1:18	1:44	
2	2:45	2:51	2:53	
3	2:21	2:18	2:30	
4	0:55	N/A	1:04	Bonding issues with AE sensor
5	2:06	1:50	2:18	
6	1:15	N/A	1:28	Bonding issues with AE sensor
7	1:09	1:08	1:15	
8	1:12	1:08	1:29	
9	N/A	1:55	2:09	TSA recording software failed
10	1:04	0:55	1:11	
11	1:40	1:30	1:57	
12	N/A	1:17	1:37	TSA did not record due to capture times

The waterjet cut, Type II samples also yielded positive results as seen in Table 6. Of the 12 tests completed with the Type II samples, crack growth was detected in all 12 by either one or both techniques. TSA did not detect crack growth in Test 12 due to the crack growing and the sample failing between recordings, to mitigate this the data capture timing should be refined to increase the chance of capturing crack growth. In Test 6 TSA did not detect a crack because the system controlling the equipment, Matlab, malfunctioned causing the data not to be recorded. It was identified that the bonding between the sensor and the surface of the sample were the reason for poor AE hit numbers in two tests as discussed in Chapter 4.4.2. The average time to failure was 1:47 hours and a cycle count of 130 000 cycles. TSA detected the crack in 1:34 hours or 113 000 cycles. AE took 1:36 hours on average to detect crack growth or 115 000 cycles. The standard deviation for the time to failure was 34 min, for TSA detection it was 37.5 min and AE detection was 36.4 min. The average time between detection and failure is a coarse measure of early warning time because each test had a different crack initiation time but it can provide a measure of which material the proposed method is best adapted to. AE detected cracks before TSA in six tests where both techniques were successful, i.e. excluding the N/A samples identified in Table 6. However, it was found that this was not always the case, TSA detected crack growth before AE in test 2. Earlier detection by AE is expected as AE captures continuously while TSA captures at a regular but slower rate which increases once AE detects crack growth, therefore TSA can only detect crack growth before AE if it occurs during capture. AE is also known to be very sensitive which makes it ideal to be the trigger for rapid TSA capture [57]. The average time between TSA detection and failure was 12.7 minutes with a standard deviation of 5.3 minutes while the time between AE detection and failure was 17.5 minutes with a standard deviation of 8.6 minutes.

Figure 33 shows the steady rise in AE energy due to expected noise from the loading, then a sudden sharp rise in energy at 2:55 due to a crack growing. The small variations in the TSA stress peak location are due to measurement uncertainty as discussed in Chapter 3.6, the crack growing then moving backwards is not physically possible. In this case, TSA detected crack growth before AE did which only occurred twice in tests using Type II samples.

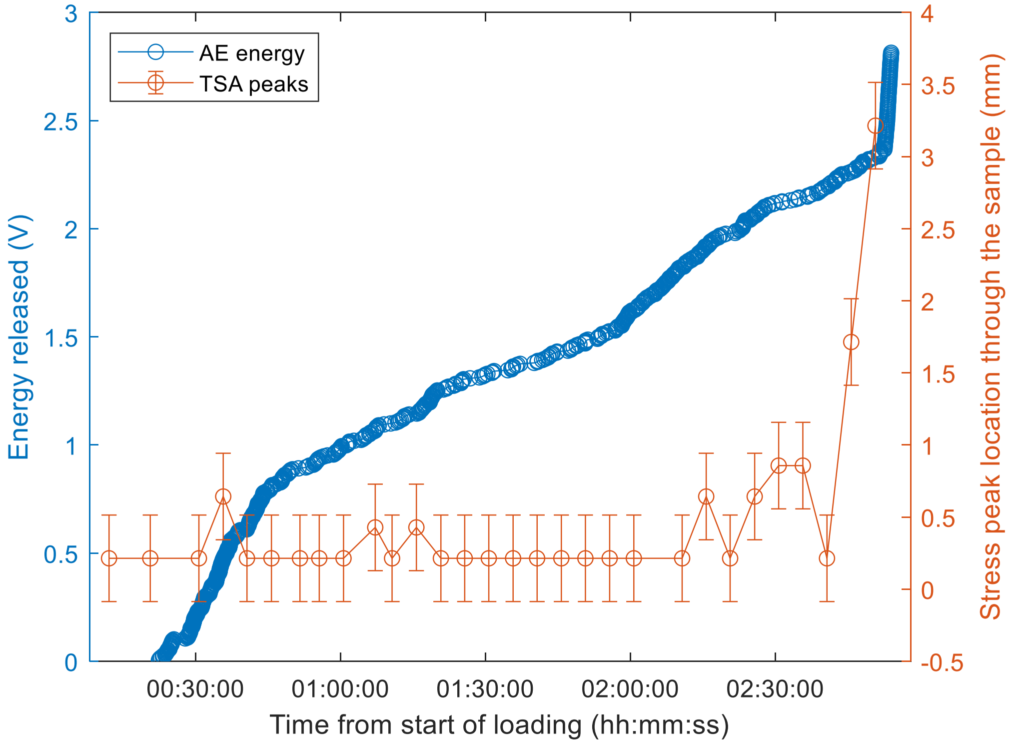

Figure 32. Type II - Test 2 sample

In Figure 34, test 4, AE detected crack growth before TSA detected a change in peak location. AE detecting crack growth before TSA was expected and increasing the capture rate for TSA would increase the chance of capturing crack growth earlier than AE. It is assumed that there is no crack present before 02:15 however the stress peak location is 1 mm instead of 0 mm because of the small distance between crack tip and peak location as mentioned in Chapter 3.6. In this case, AE did not show a slow gradual rise in activity as seen in Figure 33, this may be due to a higher threshold being set to remove the machine noise which would remove the slow rise in energy due to noise.

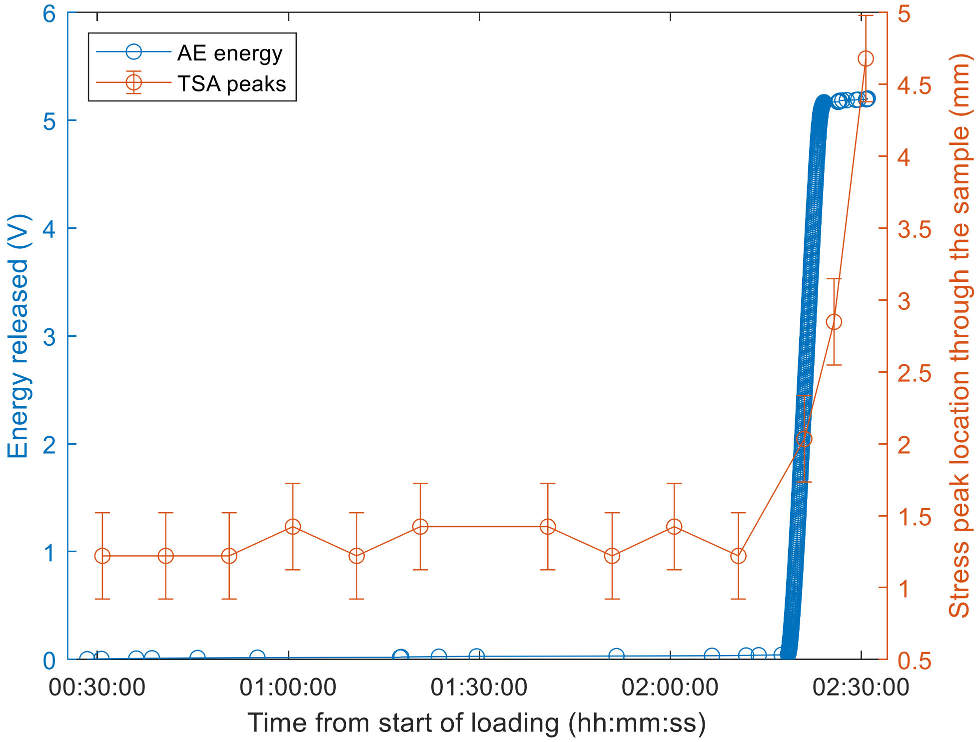

Figure 33. Type II - Test 3 sample

There are cases of TSA recordings failing to be processed and outputs NaN, the issue originates in the processing code and is being investigated. An example of such a recording can be seen in Figure 35 where an outlier close to 0 mm in stress peak location can be seen at 01:12:00. The same dataset without the corrupted recording can be seen in Figure 36. Such failed recordings will be excluded from the remainder of the data shown as this is a non-physical event, i.e. the crack does not move backwards across the sample.

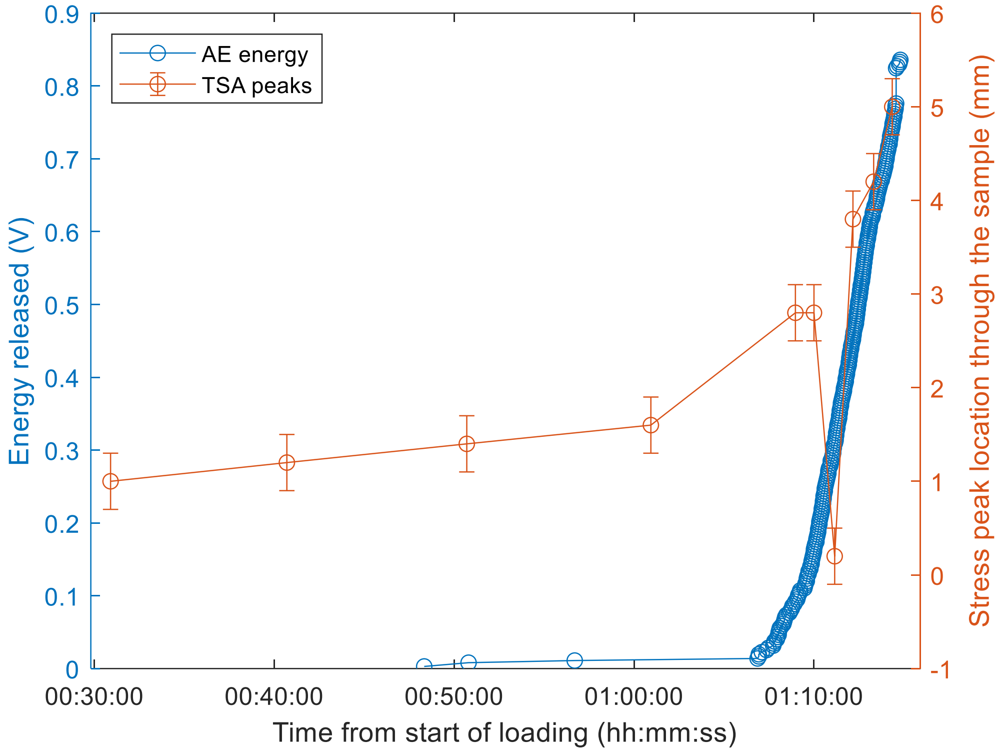

Figure 34. Type II - Test 7 sample

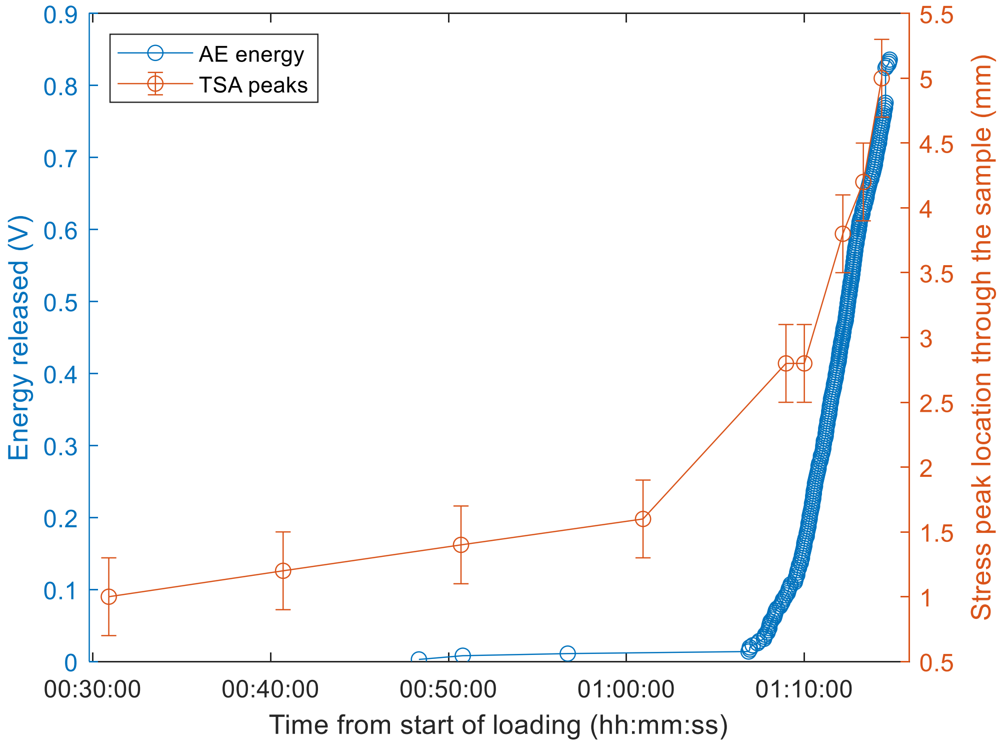

Figure 35. Type II - Test 7 sample with removed failed dataset

Figure 37 shows the results from Type II – test 8 which detected crack growth with both AE and TSA 1:25 hours after the beginning of the test. This test detected less energy than most other Type II samples but still displayed a large shift in gradient indicative of crack growth, this is to be expected as aluminium is known to be quiet for AE but the lower amount of energy collected could also be due to poor bonding of the sensor [91]. This test collected a total energy of 0.3 V where most tests with Type II samples displayed AE energy levels in the range of 0.5 V to 6 V. Any tests which detected less than 0.01 V of energy were considered substandard due to inadequate sensor bonding and were discarded because AE could not detect adequate data.

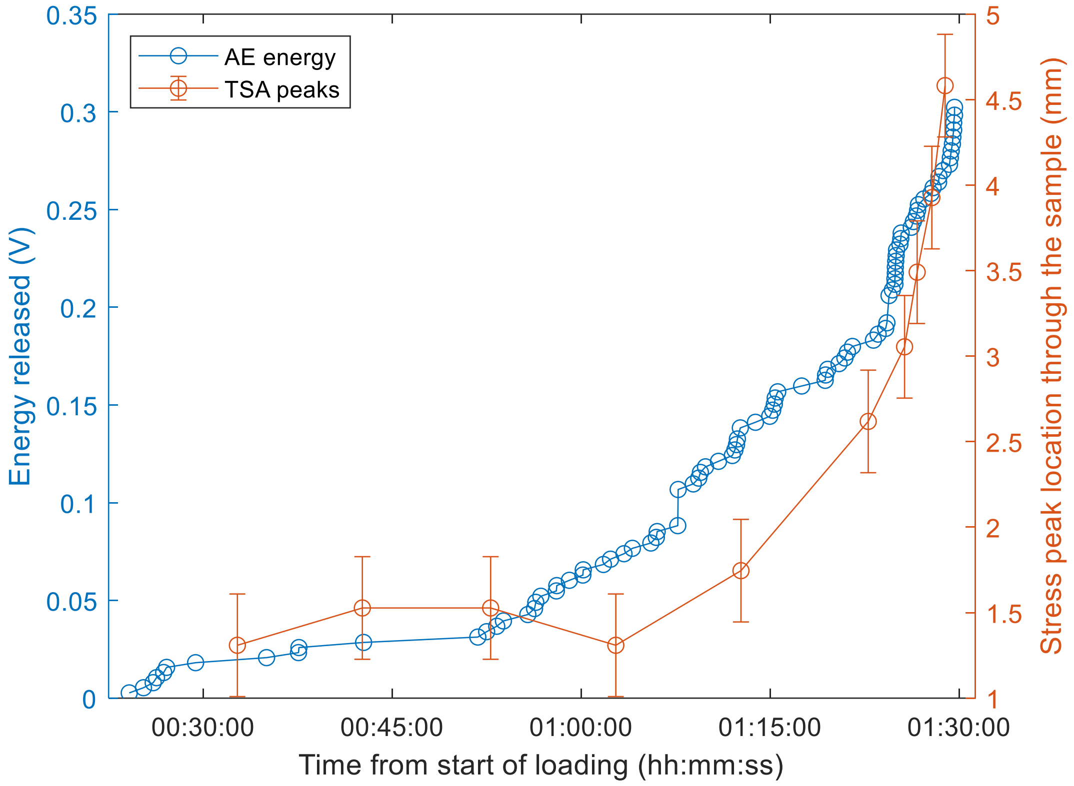

Figure 36. Type II - Test 8 sample

Tests using Type II samples have proven that the method can be successfully applied to monolithic metals to detect crack growth from a known initiation point. It could be applied to any metals parts in cyclically loaded high risks situations where the stress concentrators are known, the surface is visible for the IR camera and accessible to attach an AE sensor.

4.2 AM results

The AM samples were expected to show similar results to the monolithic samples presented with crack growth being able to be detected by both techniques. The signal generated by the crack was expected to be the same, however the formation and behaviour of the crack may change due to the orthotropic nature of the material and differing manufacturing methods.

4.2.1 Type III samples: AM aluminium

Out of the six tests completed using Type III samples, a crack could be detected in 5 tests by one or both techniques as seen in Table 7. The success of the crack detection by the method shows that it can be used in cyclically loaded SLM printed aluminium for crack detection. However, the importance of good bonding between AE sensor and sample surface was reinforced by the 4 tests in which AE could not detect crack growth or was quiet due to bonding issues. The average time to failure for the Type III samples was 44 minutes or 53 000 cycles, with a standard deviation of 17 minutes. The average time of crack detection by TSA was 35.4 minutes or 42 000 cycles, with a standard deviation of 18 minutes, leaving an average time between detection and failure of 8.4 minutes. AE meanwhile had an average time to detection of 40.5 minutes or 48600 cycles, with a standard deviation of 27.5 minutes and an average time between detection and failure of 3.3 minutes excluding the N/A tests. AE detected crack growth 13 minutes before TSA in one test and 4 minutes after TSA in one other test.

Table 7. Type III test results summary

Test number	Time of TSA detection	Time of AE detection	Time of failure	Comment
1	0:48	N/A	0:53	No AE activity before failure due to sensor bonding.
2	0:24	N/A	0:30	No AE activity before failure due to sensor bonding.
3	N/A	N/A	0:44	Issues with sensor bonding and TSA capture software.
4	1:04	1:08	1:15	
5	0:26	0:13	0:40	
6	0:15	N/A	0:21	No AE due to sensor bonding issue.

In Type III - test 4 as shown in Figure 38, crack growth is detected by TSA peak stress location and AE energy at 1:08, represented by the green line. AE shows the accumulation of machine noise before a shift in gradient at 1:08 which is confirmed by the TSA peak stress location. Prior to the green line, the change in peak stress location is within TSA error. After the green line the change peak location is greater than the error, this is when crack growth is considered detected.

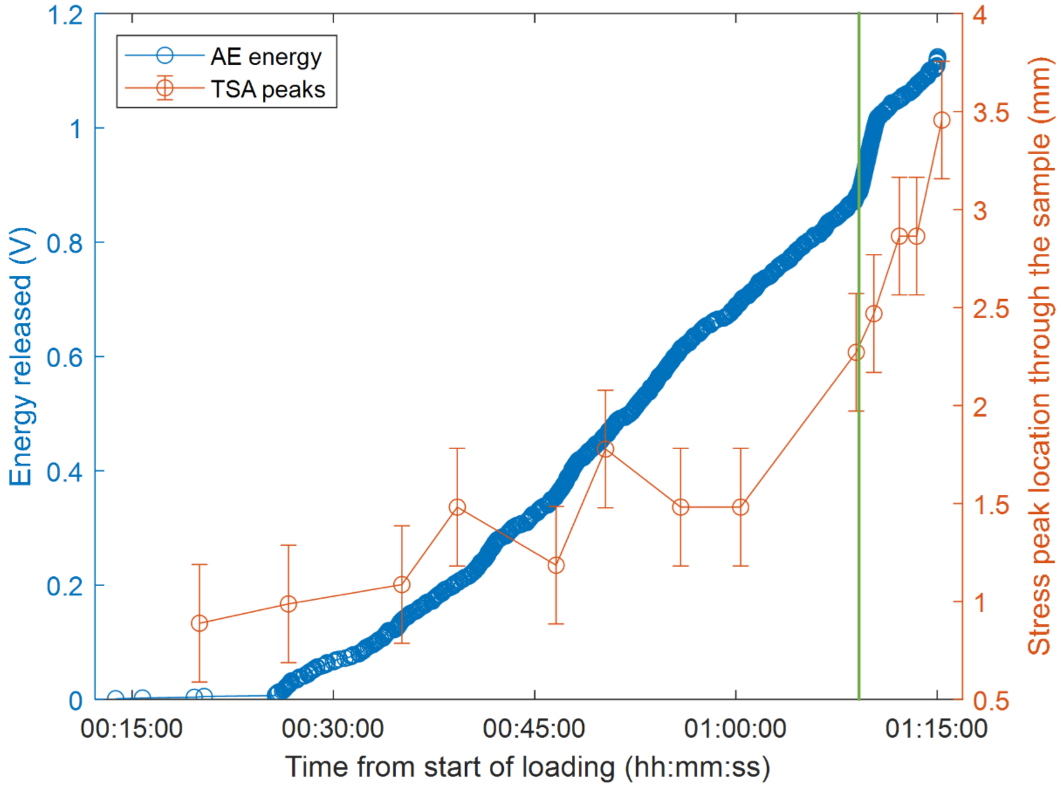

Figure 37. Type III – Test 4 sample.

Type III - Test 7 in Figure 39 showed a large peak in AE activity before a gradual rise in crack length detected by TSA 32 minutes after the beginning of the test. The AE energy is low compared to the previous test and the apparent activity starting 13 mins after the start of the test could be due to the sample slipping in the machine grips or a bonding issue between the AE sensor and the sample.

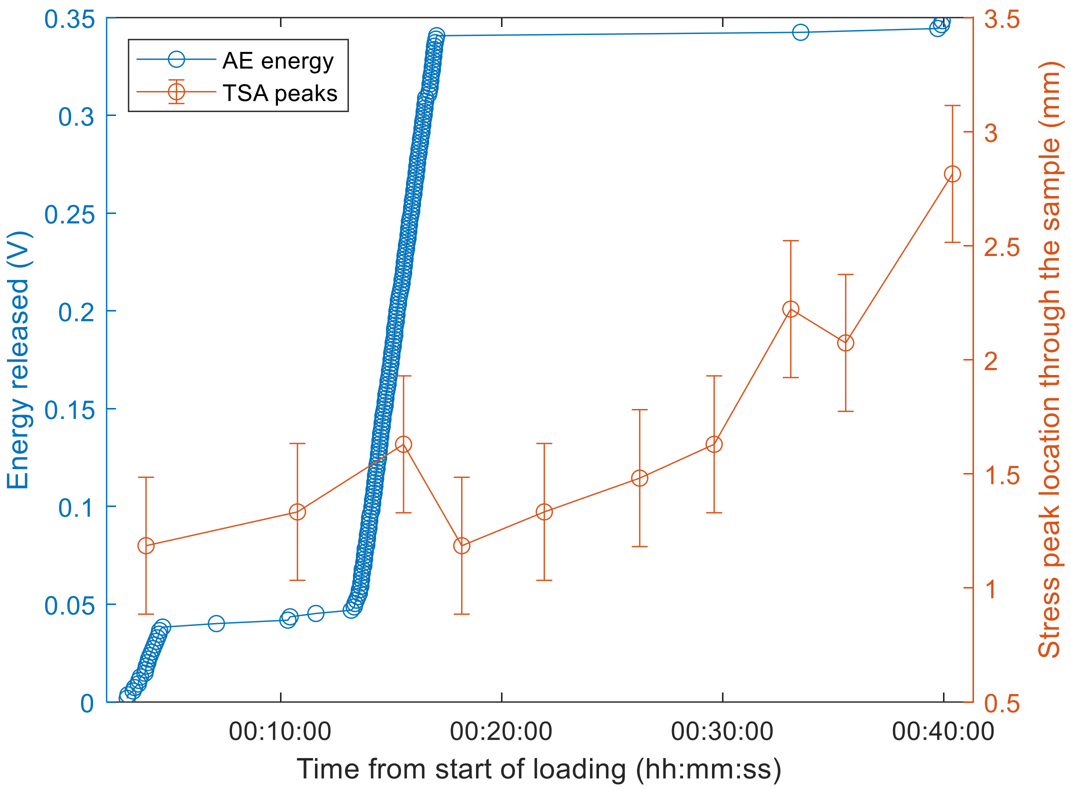

Figure 38. Type III - Test 5 samples.

4.2.2 Type IV samples: AM titanium

Ti 64 AM samples were used to apply the proposed monitoring method to a purpose-built sample with built-in notch and possible built-in subsurface defect as outlines in objectives 4 and 5. The AE sensors were glued with a stronger emphasis on good bonding which yielded good results with AE being able to capture signals in all tests as opposed to the Type III tests. The average time to failure for the Type IV samples was 1:31 hours or 109 000 cycles, with a standard deviation of 24 minutes. The average TSA detection time was 40 minutes or 48 000 cycles with a standard deviation of 24 minutes and an average time between detection and failure of 51 minutes. The average AE detection time was 1:03 hours or 76 000 cycles with a standard deviation of 17.7 minutes and an average time between detection and failure of 27.8 minutes. TSA detected crack growth first in three tests, while AE detected crack growth first in one test excluding N/A tests.

Table 8. Type IV test results.

Test	Notched	Time of TSA detection (h:mm)	Time of AE detection (h:mm)	Time of failure (h:mm)	Comment
1	Yes	0:14	1:20	2:28	
2	Yes	0:18	1:13	2:14	
3	No	N/A	0:30	0:30	Sudden failure. Did not detect with TSA due to time between captures
4	No	1:03	1:01	1:04	
5	No	1:05	1:12	1:19	

Two notched Type IV Ti64 samples were tested to determine if the method could be applied to Ti64 with the same geometry as Type III samples as seen in Table 8. Both samples displayed a gradual crack growth with one example shown in figure 40. The TSA detected the change in peak location very early in the tests, over two hours before failure, while AE activity began 1:15 hour after the start of the test, sample 2 showed a similar response. Compared to the Type III samples, AE signals were strong and consistent throughout the Type IV tests due to the different material. Literature has identified that aluminium is known to be a quiet material for AE signals [91]. It is possible that AE could detect crack growth earlier with a lower threshold to detect smaller hits caused by early crack growth in the Type IV samples. It should also be noted that the energy levels captured in the notched Type IV samples was in the order of 5 times larger than the energy observed in the Type III samples. This may be due to the good bonding between the sensor and the sample along with slow crack growth. The sampling rate for TSA was greatly increased in Type IV samples to every three minutes on average compared to the 10 minutes between recordings in Type III samples before AE activity was detected. This would have increased the chance of TSA crack detection before AE. The crack slower in the notched Type IV samples than in the notched Type III samples, this also increased the likelihood of crack detection by TSA. The slow crack growth rate and increased AE energy levels showed that the proposed method worked better in the titanium samples but could still be applied to the aluminium samples. The TSA peak stress location in Figure 40 shows the peak location at the beginning of the test at 0 mm, this is due to the fracture toughness of the material and the plastic zone. Depending on the radius of the plastic zone created by the crack, the peak stress which is at the centre of the plastic zone will be closer or further away from the tip of the crack as seen in Figure 41 [92]. In this case, the stress starts low, and the plastic zone radius is small. The size of the plastic zone is not taken into account in the peak stress location when the stress in front of the crack increases later in the test. The crack can be clearly seen growing through the Test 1 sample as seen in Figure 42.

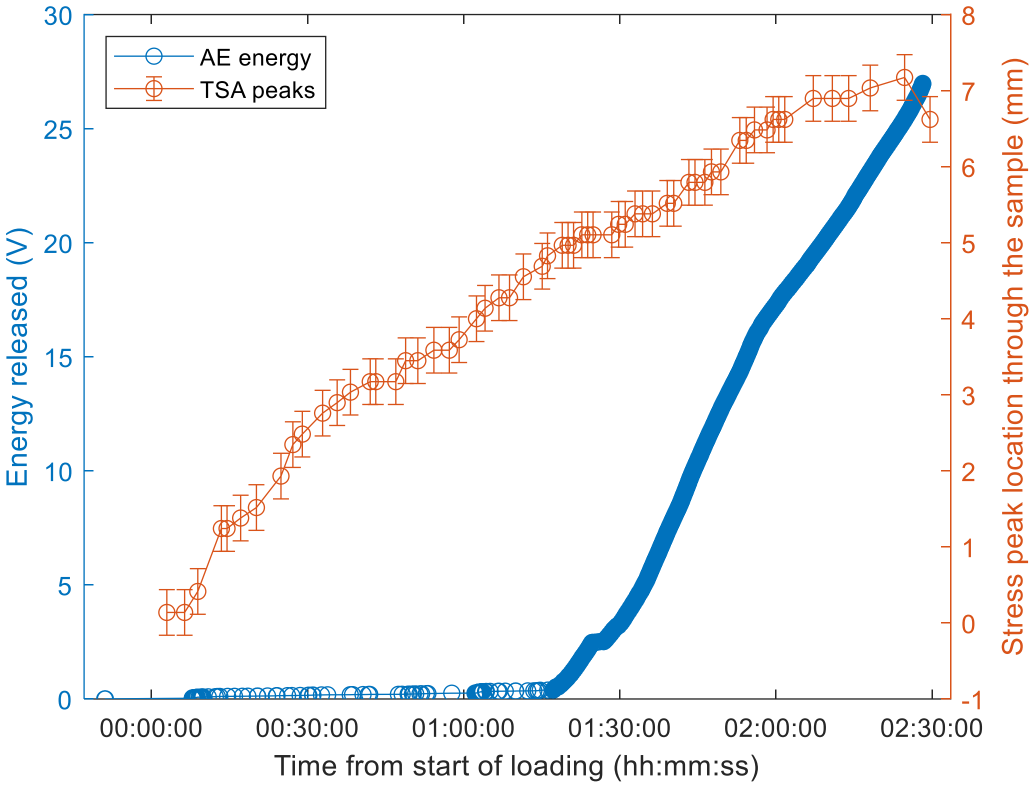

Figure 39. Type IV notched Test 1 result.

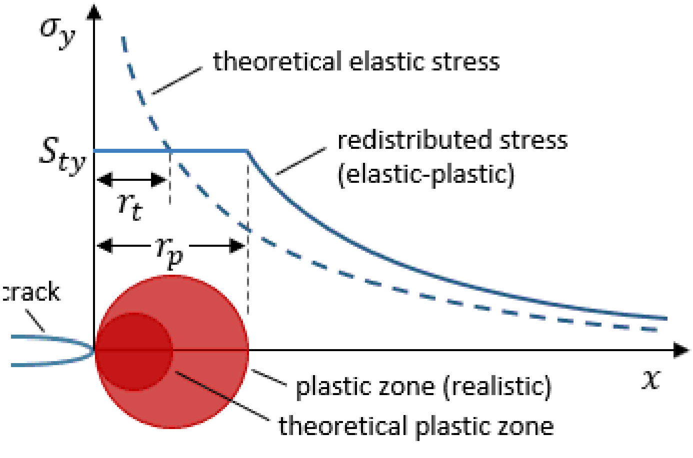

Figure 40. Plastic zone size illustration from [93].

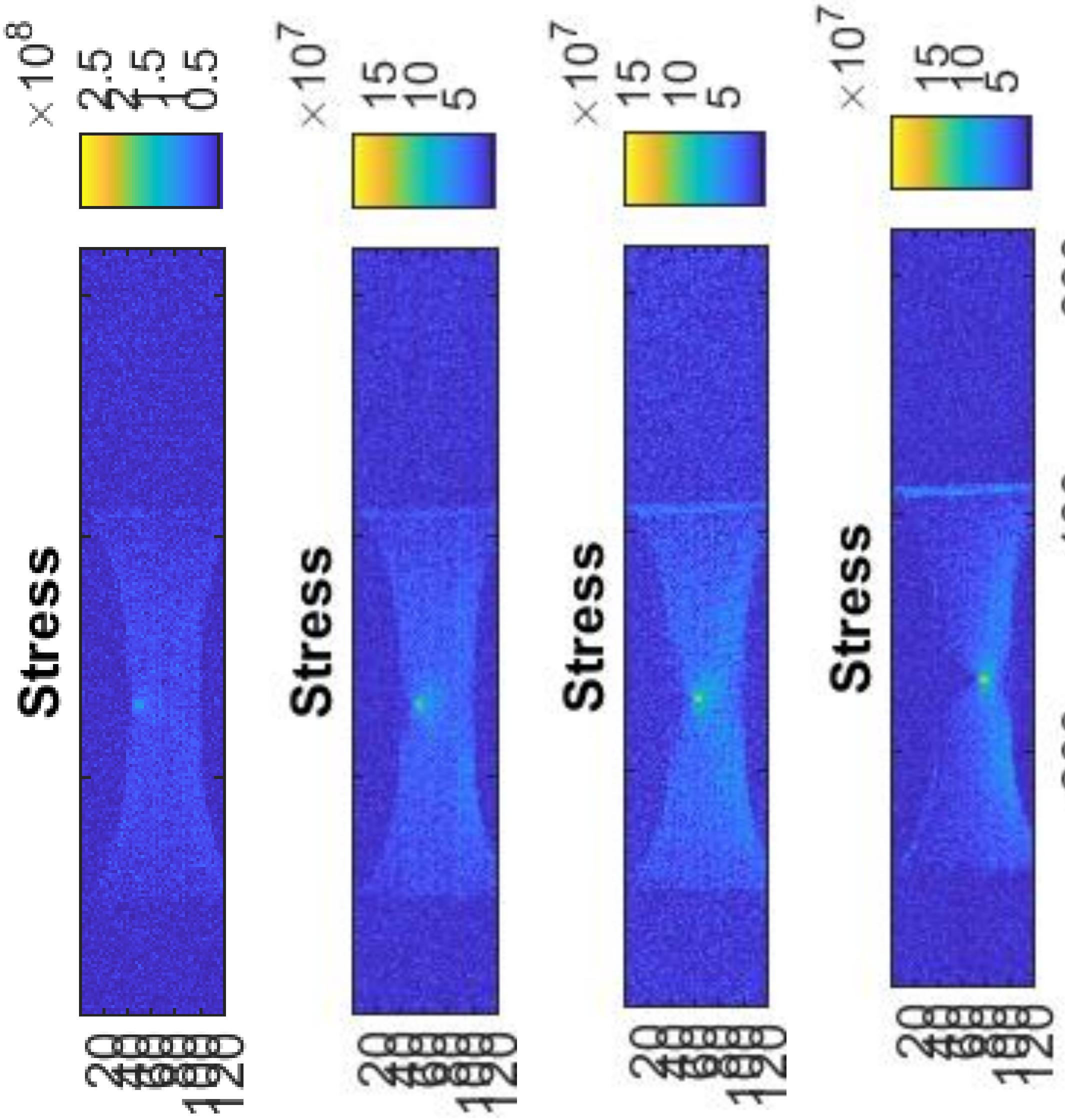

TSA at 00:8:55 TSA at 00:20:11 TSA at 00:38:15 TSA at 01:04:07

Figure 41. TSA data visualising crack growth Type IV Test 1. The bright area is an area of higher stress which precedes the crack tip.

Three plain Type IV Ti64 samples were tested to prove the method can detect defects in samples with no known crack initiation points as seen in Table 8. Previous tests used a notched sample to provide a known crack initiation point to provide a focus point to monitor. Without the notch, a crack could grow anywhere on the sample and could grow at an angle, increasing the area required to be monitored by TSA. However, the lack of a known crack initiation point is likely in out-of-lab situations where their exact positions in a part is less well defined or known. TSA could not detect a crack on one sample due to the capture rate, but cracks were detected in the two other samples. In Test 4, crack growth was detected by TSA in the last frame, seen in Figure 43, one minute before failure. The crack is only noticeable by analysing the final frame and does not appear in any previous frames. The crack growth rate was much faster in the plain Type IV samples than in the notched samples, this could be due to a higher loading which increased the crack growth rate.

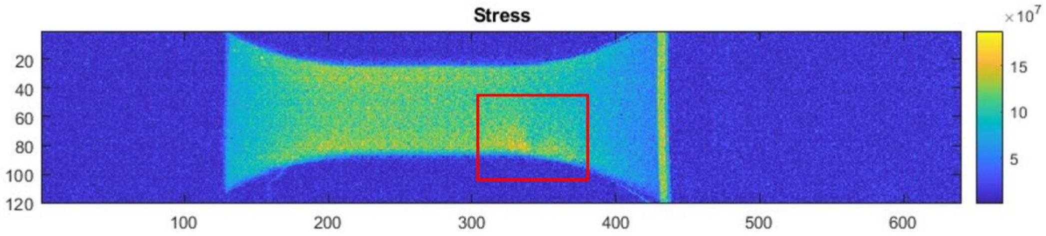

Figure 42. Type IV Test 4 sample TSA recording showing crack growth in red rectangle.

AE detected crack growth in all three samples with Test 5 being shown in Figure 44. A slow increase in AE energy can be seen throughout the loading until 1:15 when a rise in energy is detected. This coincides with the crack length increasing two minutes earlier detected by TSA. A processed TSA recording can be seen in Figure 45 which shows the location of the crack. The crack tip location is no longer measured relative to the notch but to the edge of the sample. The reason why the starting peak stress location is close to 0 mm is explained above for the notched Type IV samples.

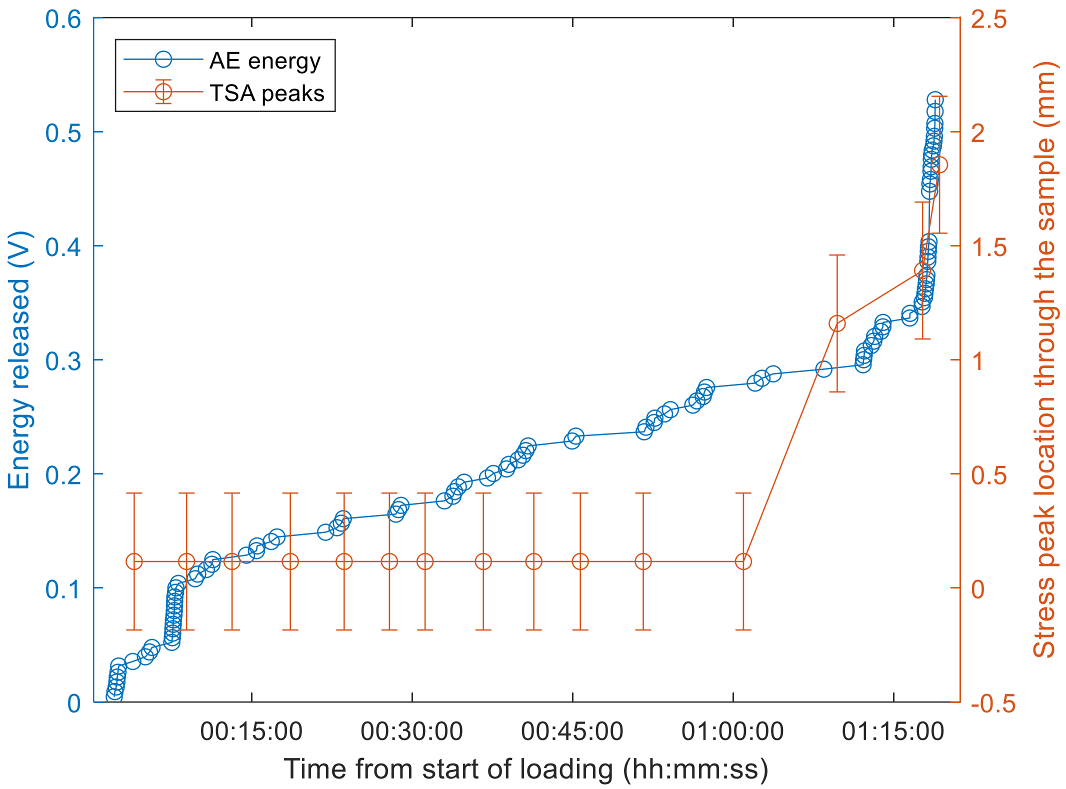

Figure 43. Type IV Test 5.

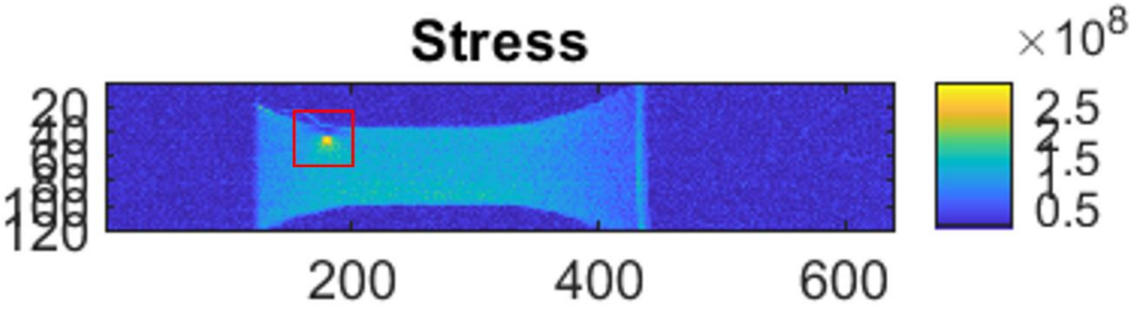

Figure 44. Crack location highlighted by red rectangle from Type IV Test 5.

4.3 Discussion

In type II samples, crack growth was detected in 100% of cases by either AE or TSA or both. TSA detected crack growth in 83% of tests and AE in 67% of tests. The tests where TSA failed were due to the length of time between capture events, not the technique itself. The frequency of capture events can be increased to detect rapid crack growth in the future. The effects of this are shown in the Type IV tests where TSA was recorded every three minutes instead of every 10 minutes like in Type III samples. The crack growth was tracked with much higher resolution however, a compromise must be made due to the much larger volume of data collected which would require a more powerful system to process and store.

There were no major differences between monolithic and AM samples in signal captured during testing. AE energy was as quiet in monolithic and AM aluminium, with titanium showing a much stronger signal and TSA functioned in both monolithic and AM metals. Because both techniques worked in both monolithic and AM metals, this approached has been demonstrated as feasible on both. The main difference between AM and monolithic would be potential initiation points that could be caused by LOF defects, however this would be heavily dependent on print quality and post-processes used on the material.

In the AM Type III samples, crack growth was detected in five out of six tests by either one or both techniques. TSA worked in 83% of tests, the test where it did not work was due to similar reasons to Type II tests. AE worked in 33% of the tests, similar improper bonding of sensor was the reason for the tests where AE did not work.

Two notched Type IV samples were tested to prove that the method can be applied to Ti64. Both tests were a success with TSA detecting crack growth two hours before failure and AE one hour before failure. Three plain Type IV samples were also tested to determine if the method could detect crack growth in samples with no known initiation points. Crack growth was detected in all three samples by either one or both techniques, TSA did not capture it in one test due to time between capture, but AE detected it in all three samples a few minutes before failure. The bonding issues between the AE sensor and sample were addressed in the Type IV tests with 100% crack detection by AE before failure. The notched Ti64 samples showed slow crack growth which could be detected early by both TSA and AE, this was better than the aluminium samples discussed earlier where the time between detection and failure were shorter because it increases the probability of detection and an opportunity to intervene before catastrophic failure. The reason for the slower crack growth could be due to lower loads applied to the material. The fracture toughness of aluminium is smaller than that of titanium which could also explain why crack growth was faster in aluminium than titanium at similar relative loads. A slower crack growth rate is beneficial to the monitoring method, and new material should be investigated prior to testing because their material properties could negatively affect the crack growth rate and decrease the effectiveness of the proposed method.

Overall crack growth was detected in all tests where the data capture was successful. The main limitations with this method were experimental, namely the TSA time between capture, AE sensor bonding and thresholding. All of which impacted data capture itself. When data could be captured, both techniques worked together to detect crack location, growth rate and severity. The first two limitations were addressed with the Type IV samples, TSA was captured at a much higher frequency and AE sensors were bonded with higher quality leading to more reliable crack detection and monitoring. AE was expected to detect crack growth before TSA due to the continuous capture and higher sensitivity as discussed in Chapter 2.3 compared to the larger TSA capture time interval, however this was not always the case, and a high threshold value was believed to be the reason. A smaller threshold for AE hit capture could increase the probability of AE detecting crack growth before TSA as was expected and solve the final limitation. AE was able to detect crack growth reliably by monitoring for the energy released by crack growth 33 000 cycles before failure on average, which leaves time to a part to be replaced before catastrophic failure. TSA meanwhile could detect crack growth 61 000 cycles before failure on average but requires continuous processing to detect the crack before too much time is elapsed. The raw IR data was processed after the sample's failure for this study, but continuous monitoring would require the raw IR data to be processed immediately after capture to provide timely crack detection in-situ. Depending on the size of the raw footage, a powerful computer may be required to speed processing and therefore capture rate.

The time between capture of TSA recordings is a compromise between volume of data collected and the possibility of missing an event. The TSA capture was manually triggered in this study but could be automated. The optimal timing could be investigated by testing samples with a high capture rate, and determining how many capture events are needed to detect crack growth by reducing the number of used recordings to simulate a slower capturing frequency. The crack growth rate is highly dependent on loading parameters and material properties and should be considered when determining the optimal capture frequency. A slower crack growth rate would not require as fast a capture frequency as a faster crack growth rate material because there would be a higher probability of capturing crack growth before failure. In Type IV – Test 1, 22 GB of raw TSA data was captured. This is acceptable for a lab setting but would be too much to continuously monitor multiple parts at once in a system without an expensive set up to collect, store and process the raw data. The raw frames saved in this study were windowed down frames with 120 x 480 pixels, however, not all the frame was needed, and background pixels could have been dropped to reduce the overall volume of data. This would have to be done on a case-by-case basis for each part being monitored but would enable a cheaper system to be used to handle the data. The raw data does not need to be stored once it has been processed, a single processed frame is outputted from 3750 raw frames (based on a 30 second recording at 125 Hz). The resolution of the IR camera could be reduced at the cost of location accuracy, this compromise may be preferable in some applications where many IR sensors are required to reduce the volume of data and speed processing time.

Multiple AE sensors could be glued to the sample to not only increase the data collection reliability in case one sensor is not glued on adequately but also to provide linear crack location and machine loading noise removal. A sensor could be placed on either end of the sample to provide the location and another sensor placed on either grip to provide the machine noise. This was not possible in the current study due to equipment constraints but would be achievable with multi-channel capable equipment.

AE data storage and handling can also be an issue. In Type IV – Test 1 AE collected 7.9 GB of data. The whole waveform was saved however only the energy released was used in the results. There is potential to reduce the volume of data by extracting the energy as the waveform is being captured and only saving the energy. However, doing so may increase saving time and reduce the amount of potential waveform captures in a given amount of time. With the current recording parameters, system and processing power, saving the waveform takes 0.7 seconds, extracting the energy value from the waveform may increase the time to save each hit slightly by requiring an additional operation to each waveform but would drastically reduce data volume. Another method to reduce AE data volume would be to take 25 parameters that define the waveform using Chebyshev descriptors [73]. This method does not require large computing power and means the waveform can be discarded almost immediately after capture to save storage space. This method has proved sufficient to describe variations from calibration waveforms and can be used to reduce the computational power and storage required to continuously monitor parts.

Applying the proposed continuous monitoring method to parts could also enable safety factors to be reduced. If the part is continuously monitored it may not need the large safety factors it once needed, meaning the part could be lighter and cheaper at the cost of a monitoring system. The AE set-up used in this study cost 20 000 NZD and the IR microbolometer used was 12 000 NZD, however this is a laboratory system. The cost of sensors is lowering at a steady pace and chip-based sensors could be used in situation where their characteristics are enough for the application. There is potential to make cheap systems when prices drop, and components become more refined. The PureThermal Mini Pro JST-SR (with FLIR Lepton 3.5) is an example of an IR camera that could be used with a cost of 740 NZD and a thermal resolution of 50 mK similar to the IR microbolometer used in this study [94]. An Arduino UNO could potentially be used to collect AE data at a cost of 44 NZD instead of the Picoscope used in this study.

Due to issues in capturing data, some cracks have gone undetected by one or both methods. The main limitations have been identified and were addressed in Type IV samples to yield a much higher crack detection rate with early detection of crack growth. There are still limitations such as rapid crack growth causing catastrophic failure which is difficult to detect using TSA due to the short window between crack initiation and failure. Rapid failure was more prominent in samples under a high cyclic load such as Type II samples and samples with no know initiation sites as seen in Type IV tests. Because of these limitations, consideration to the application of this method should include parts that can tolerate some undetected crack growth without failure until the method is refined counter the limitations.

All objectives laid out in Chapter 1.2 have been achieved except the final one which was to detect subsurface defects in built-in AM samples. AE inspection, equipment and methodology was developed for crack detection. The independent methods and processing for TSA and AE were developed before being implemented together in Type II and Type III samples with the updated method being used in the Type IV samples. Type IV samples with built-in subsurface defects were manufactured but the defect did not materialise in the samples as discussed in Chapter 5.2.

Chapter 5

Conclusion and future work

5.1 Conclusion

A new method combining TSA and AE to monitor cyclically loaded metal parts for crack growth was presented and experimentally tested. Combining TSA and AE increased the chance of crack detection, location of crack initiation and a measure of crack severity in-situ. The TSA can provide the location and monitor crack growth rate but cannot detect cracks that are deep under the surface that do not affect the surface stress field, while AE can detect deep cracks but cannot locate them. Combining the two has not been done before in such a way for crack detection and monitoring. The method proved successful in detecting cracks in all tests with monolithic and SLM printed metals when the techniques were applied correctly. Notched monolithic aluminium sample were used to develop the method while SLM printed aluminium samples were used to prove the method can be used in AM metals. Finally, the method was applied to SLM printed Ti64 samples to prove it can be used in another material both when a notch is present in the sample and without a notch.

The importance for good bonding between piezoelectric sensor and sample surface was shown during the Type II and Type III tests with multiple tests failing due to inadequate bonding. This can be remedied with removing and re-bonding the sensor on which worked well during the Type IV tests, but a way to reliably bond the sensor the first time with glue should be investigated. The sensor could be bonded a different way using mechanical fasteners or other methods as presented in Chapter 4.3 to remove the uncertainty of glue bonding. The timing of the TSA capture should also be investigated as mentioned in Chapter 4.3 because it caused multiple tests to fail because crack initiation and sample failure occurred between capture events.

This study has proved that this combined approach can be applied to metal parts that are under cyclic loading. It could then be applied to any part undergoing such loading with the area of interest on the surface being visible by TSA and accessible for an AE sensor to be bonded. If the part is designed with this method in mind, a dedicated bonding point could be manufactured directly on the surface to provide a good interface for the piezoelectric sensor. The surface should also be able to be painted with matt black paint to enable a high and uniform surface emissivity for TSA.

5.2 Future work

Multiple areas in this study showed the need for further investigations.

5.2.1 Designing new purpose-built samples

Samples with built-in defects should be investigated. Type IV samples with a subsurface defect were planned but the defect did not appear in the samples after manufacturing. Subsurface defects should be able to be detected by both techniques used in this method up to a maximum depth by TSA. It was seen that pores are present in the microstructure of the material and their effects on crack growth should be investigated.

A series of Type IV samples were manufactured with a built-in defect; however, this defect did not materialise in the sample after manufacturing. The expected layer thickness was 20 µm and the defect was planned to be two layers thick or 40 µm to replicate a LOF defect. Micrographs were extracted from the Type IV sample in Figure 47 which came from the centre of the sample as seen in Figure 46. The surface of the sample was prepared with a 500 grit SiC plate, a diamond solution with particle size of 9 µm and a silica solution (OPS) before being etched with Kroll’s reagent (2%HF, 6%HNO3 in distilled water). A defect in the form of porosity should be present in the middle of Figure 47, but no defect can be found. As the defect did not affect the stress distribution in the samples, they were considered as plain. The reason for the absence of the defect is unknown at present and requires further investigation. The microstructure does show the presence of porosity within the material structure as highlighted in Figure 48. The defect inclusion in the sample should be investigated in the future with thicker defects to be manufacturable with the current printing parameters.

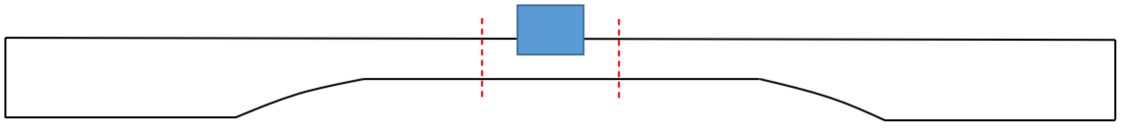

Figure 45. Location of the micrographs seen in Figure 47 on Type IV samples. the micrograph is taken from the top side of the sample and is represented by the blue rectangle.

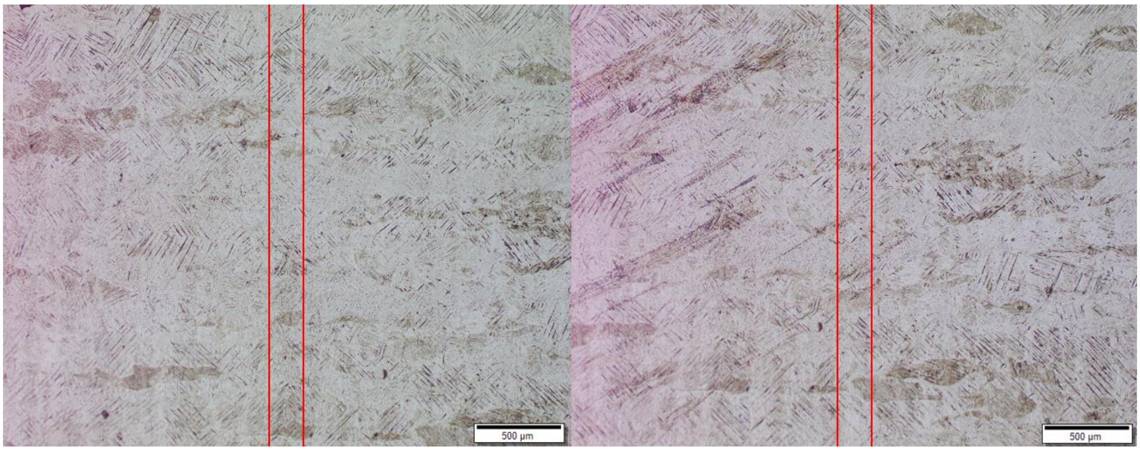

Figure 46. Two micrographs from the centre of the Type IV sample with planned defect. The defect should be visible between the red lines.

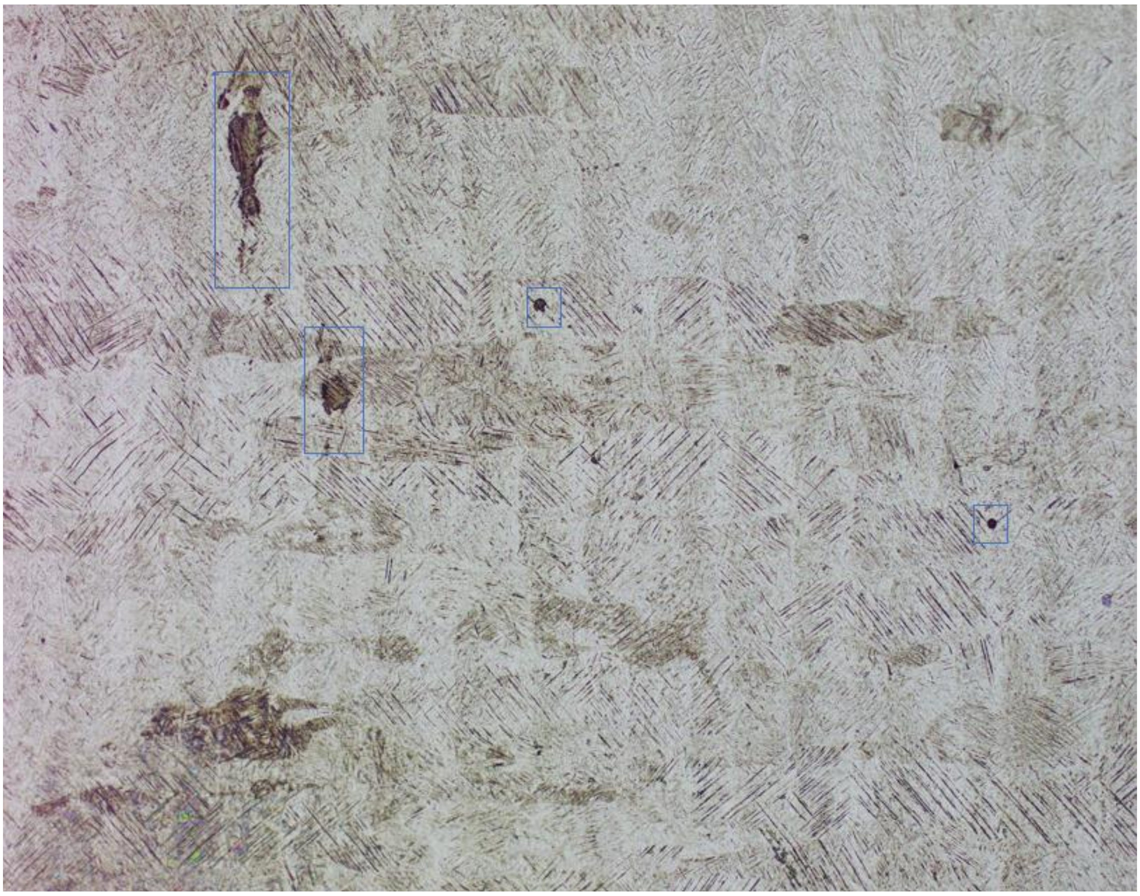

Figure 47. Type IV sample micrograph. Pores are highlighted by blue rectangles.

5.2.2 Designing a purpose-built monitoring system

The boundaries of suitable applications for this approach should be investigated. E.g which material and industries where a defect of a detectable size is tolerable, acceptable specifications for monitoring systems, lowest IR camera resolution to detect crack growth, etc. Designing a cheaper system using chip-based components could be a viable way to reduce the cost, size and weight of the set up to enable monitoring of larger systems at an industrial scale. Reducing the amount of data required for crack detection and monitoring should also be investigated. Reducing the size of the frame captured by TSA could reduce the data required if the defect initiation site is at the centre of the frame. Calculating and saving the energy for each AE waveform captured could also decrease data volume but may increase the time between captures because of the additional processing required. Current chip-based IR cameras have a slower capture rate than other microbolometers, however TSA has been shown to be possible with slower capture rates and loading rates[31; 95]. Non-cyclic loading should also be investigated to determine if the proposed monitoring method could be applied to applications undergoing such loading [38].

The issue of bonding the AE sensor to the sample surface can be remedied in future work with designated built-in mounting points in the parts to provide a good connection between the part and the sensor. Sensors could also be imbedded in AM parts during manufacture to ensure a good interface between the sensor and the material. This has been done previously in composite materials where Polyvinylidene sensors (PVDF) were embedded in fibre glass and resin composites samples that were tensile tested [96]. It was found that the amplitude of the signals captured by the embedded sensor were higher than the ones without an embedded sensor and that the mechanical strength of the material was only negligibly decreased by the presence of the embedded sensor. Recently a study has considered embedding a PVDF sensor on aluminium by using ultrasonic AM to bond the sensor to the surface [97]. A pocket in the sample is milled to create room for the sensor, it is installed in the pocket and a layer of aluminium foil covers the sensor. This foil is then ultrasonically welded to the aluminium sample, effectively embedding the sensor between the foil and the sample. This technique allows sensors to be embedded without using high temperatures which could potentially damage the sensor or introduce localised heat treatment to the sample. Although it could not be used for AE as is, other piezoelectric sensors could possibly be embedded in metal samples using this method. This would work well in AM metal samples where the pocket could be designed in the part removing the need for it to be milled.

References

---

[1] Grand Veiw Research (2020). *Additive Manufacturing Market Size, Share & Trends Analysis Report By Component, By Printer Type, By Technology, By Software, By Application, By Vertical, By Material, By Region, And Segment Forecasts, 2022 - 2030.*

[2] Lewandowski, J. J., & Seifi, M. (2016). *Metal Additive Manufacturing: A Review of Mechanical Properties*. Annual Review of Materials Research, 46(1), 151-186.

[3] Fatemi, A., Molaei, R., Simsiriwong, J., Sanaei, N., Pegues, J., Torries, B., Phan, N., & Shamsaei, N. (2019). *Fatigue behaviour of additive manufactured materials: An overview of some recent experimental studies on Ti-6Al-4V considering various processing and loading direction effects.* Fatigue & Fracture of Engineering Materials & Structures, 42(5), 991-1009.

[4] Mower, T. M., & Long, M. J. (2016). *Mechanical behavior of additive manufactured, powder-bed laser-fused materials*. Materials Science and Engineering: A, 651, 198-213.

[5] Dian-Zheng Wang, K.-L. L., Chen-Fan Yu, Jing Ma, Wei Liu, Zhi-Jian Shen. (2019). *Cracking Behavior in Additively Manufactured Pure Tungsten.* Acta Metallurgica Sinica (English Letters), *32*(1), 127-135.

[6] Reider, H., Dillhofer, A., Spies, M., Bamberg, J., & Hess, T. (2014). *Online Monitoring of Additive Manufacturing Processes Using Ultrasound* Presented at the 11th European Conference on Non-Destructive Testing.

[7] Hansen, R. S., Burn, K. Z., Rigby, C. M., Ashby, E. K., Nickerson, E. K., & Berke, R. B. (2022). *Digital image correlation at long working distances: The influence of diffraction limits.* Measurement, 189, 110493.

[8] ASTM *ASTM 52900 Additive manufacturing - General principles - Fundamentals and vocabulary.*

[9] Godec, D., Pilipović, A., Breški, T., Ureña, J., Jordá, O., Martínez, M., Gonzalez-Gutierrez, J., Schuschnigg, S., Blasco, J. R., & Portolés, L. (2022). *Introduction to Additive Manufacturing.* In D. Godec, J. Gonzalez-Gutierrez, A. Nordin, E. Pei & J. Ureña Alcázar (Eds.), A Guide to Additive Manufacturing (pp. 1-44). Cham: Springer International Publishing.

[10] Singh, S. R., & Khanna, P. (2021). *Wire arc additive manufacturing (WAAM): A new process to shape engineering materials.* Materials Today: Proceedings, 44, 118-128.

[11] Frazier, W. E. (2014). *Metal Additive Manufacturing: A Review.* Journal of Materials Engineering and Performance, 23(6), 1917-1928.

[12] Sanaei, N., & Fatemi, A. (2021). *Defects in additive manufactured metals and their effect on fatigue performance: A state-of-the-art review.* Progress in Materials Science, 117, 100724.

[13] Ratna, D. (2022). *Recent Advances and Applications of Thermoset Resins*. (Second edition.).

[14] Zhang, B., Li, Y., & Bai, Q. (2017). *Defect Formation Mechanisms in Selective Laser Melting: A Review.* Chinese Journal of Mechanical Engineering, 30(3), 515-527.

[15] Yap, C. Y., Chua, C., Dong, Z., Liu, Z., Zhang, D., Loh, L. E., & Sing, S. L. (2015). *Review of selective laser melting: Materials and applications.* Applied Physics Reviews, 2, 041101.

[16] AbouelNour, Y., & Gupta, N. (2022). *In-situ monitoring of sub-surface and internal defects in additive manufacturing: A review.* Material & Design.

[17] Zeng, K., Pal, D., & Stucker, B. (2012). *A review of thermal analysis methods in laser sintering and selective laser melting.* 23rd Annual International Solid Freeform Fabrication Symposium - An Additive Manufacturing Conference, SFF 2012, 796-814.

[18] Mohr, G., Altenburg, S. J., Ulbricht, A., Heinrich, P., Baum, D., Maierhofer, C., & Hilgenberg, K. (2020). *In-Situ Defect Detection in Laser Powder Bed Fusion by Using Thermography and Optical Tomography—Comparison to Computed Tomography.* Metals, 10(1), 103.

[19] Seleznev, M., Gustmann, T., Friebel, J. M., Peuker, U. A., Kühn, U., Hufenbach, J. K., Biermann, H., & Weidner, A. (2022). I*n situ detection of cracks during laser powder bed fusion using acoustic emission monitoring.* Elsevier.

[20] Charalampous, P., Kostavelis, I., & Tzovaras, D. (2020). *Non-destructive quality control methods in additive manufacturing: a survey.* Rapid Prototyping Journal, 26(4), 777-790.

[21] Allevi, G., Cibeca, M., Fioretti, R., Marsili, R., Montanini, R., & Rossi, G. (2018). *Qualification of additively manufactured aerospace brackets: A comparison between thermoelastic stress analysis and theoretical results*. Measurement, 126, 252-258.

[22] Dulieu-Barton, J. M. (2012). *Thermoelastic stress analysis*. In optical Methods for Solid Mechanics, A full-field approach (Vol. 2012, pp. 345-366). Wiley-VCH.

[23] Thompson, W. (1853). *On the Dynamical Theory of Heat, with numerical results deduced from Mr Joule's Equivalent of a Thermal Unit, and M. Regnault's Observations on Steam*. Transactions of the Royal Society of Edinburgh, 20(2), 261-288.

[24] Compton, K. T., & Webster, D. B. (1915). *Temperature Changes Accompanying the Adiabatic Compression of Steel*. Physical Review, *5*(2), 159-166.

[25] Belgen, M. H. (1967). *Structural stress measurements with an infrared radiometer.* ISA Trans., 6, 49-53.

[26] Belgen, M. H. (1967). *Infrared radiometric stress instrumentation application range study.* NASA technical reports.

[27] Dulieu-Smith, J., Quinn, S., Shenoi, R., Read, P., & Moy, S. s. J. (1997). *Thermoelastic Stress Analysis of a GRP Tee Joint.* Applied Composite Materials, 4, 283-303.

[28] Yadav, P. V. K., Yadav, I., Ajitha, B., Rajasekar, A., Gupta, S., & Ashok Kumar Reddy, Y. (2022). *Advancements of uncooled infrared microbolometer materials: A review.* Sensors and Actuators A: Physical, 342, 113611.

[29] Sambasivam, S. (2009). *Thermoelastic stress analysis of laminated composite materials.* Doctoral Thesis thesis, University of Southampton.

[30] Bayareh, R., Vera, A., Leija, L., & Gutierrez-Martínez, J. (2017). *Programming of a system for the acquisition of images and thermographic data for the diabetic foot analysis.* In 2017 14th International Conference on Electrical Engineering, Computing Science and Automatic Control (CCE) (pp. 1-7).

[31] Pitarresi, G., Cappello, R., & Catalanotti, G. (2020). *Quantitative thermoelastic stress analysis by means of low-cost setups.* Optics and Lasers in Engineering, 134, 106158.

[32] Uchida, Y., Kanade, T., Shiozawa, D., & Sakagami, T. (2023). *Thermoelastic Stress Measurement Using SVD Thermo-Component Analysis.* Experimental Mechanics, 63(2), 337-347.

[33] Bercelli, L., Doudard, C., Calloch, S., Le Saux, V., & Beaudet, J. (2023). *Thermometric investigations for the characterization of fatigue crack initiation*

and propagation in Wire and Arc Additively Manufactured parts with as-built surfaces. Fatigue & Fracture of Engineering Materials & Structures, 46(1), 153-170.

[34] Greene, R. J., Patterson, E. A., & Rowlands, R. E. (2008). *Thermoelastic stress analysis.* In Springer (Ed.), Springer Handbook of experimental solid mechanics.

[35] Robinson, A. F., Dulieu-Barton, J., Quinn, S., & Burguete, R. (2010). *Paint coating characterization for thermoelastic stress analysis of metallic materials.* Measurement Science and Technology, 21, 085502.

[36] Dulieu-Barton, J. M., Fruehmann, R. K., & Quinn, S. (2013). *A Full-Field Stress Based Damage Assessment Approach for In Situ Inspection of Composite Structures.* Key Engineering Materials, 569-570, 3-10.

[37] Tighe, R. C., Howell, G. P., Tyler, J. P., Lormor, S., & Dulieu-Barton, J. M. (2016). *Stress based non-destructive evaluation using thermographic approaches: from laboratory trials to on-site assessment.* NDT & E International, 84, 76-88.

[38] Misiewicz, R., Moczko, P., & Boyce, B. (2022). *The use of thermoelastic stress analysis for stress distribution evaluation of an industrial equipment under regular operating conditions.* Archives of Civil and Mechanical Engineering, 22(3), 106.

[39] Crump, A. C., Sathon, N., Tighe, R. C., Reed, P. A., & Dulieu-Barton, J. M. (2017). *Development of a technique for evaluating damage in composites overwrapped pressure vessels using TSA*. Presented at the 21st International Conference on Composite Materials.

[40] Quinn, S., Dulieu-Barton, J. M., & Fruhmann, R. K. (2008). *In-service TSA of composite structures using transient loading* In XIth International Congress and Exposition. Orlando, Florida USA.

[41] Krstulovic-Opara, L., Klarin, B., Neves, P., & Domazet, Z. (2011). *Thermal imaging and Thermoelastic Stress Analysis of impact damage of composite materials.* Engineering Failure Analysis, 18(2), 713-719.

[42] Palumbo, D., De Finis, R., Saponaro, A., Nobile, R., Panella, F., & Galietti, U. (2021). *Assessment of TSA Technique for the Estimation of CFRP T-Joint Debonding.* Journal of Nondestructive Evaluation, 40(4), 94.

[43] Palumbo, D., De Finis, R., Demelio, G. P., & Galietti, U. (2017). *Study of damage evolution in composite materials based on the Thermoelastic Phase Analysis (TPA) method.* Composites Part B: Engineering, 117, 49-60.

[44] Fruehmann, R. K., Dulieu-Barton, J. M., & Quinn, S. (2010). *Assessment of fatigue damage evolution in woven composite materials using infra-red techniques.* Composites Science and Technology, 70(6), 937-946.

[45] Dulieu-Barton, J. M., & Emery, T. R. (2008). *Prediction of fatigue life in composite materials using thermoelastic stress analysis*. Presented at the 17th European Congress on Fracture.

[46] Demelio, P. G., De Finis, R., Galietti, U., & Palumbo, D. (2016). *Fatigue Limit Evaluation of Composite Materials by Means of TSA.* Presented at the 13th International Conference on Quantitative Infrared Thermography 2016, Gdansk, Poland.

[47] Wei, B.-S., Johnson, S., & Haj-Ali, R. (2010). *A stochastic fatigue damage method for composite materials based on Markov chains and infrared thermography.* International Journal of Fatigue, 32(2), 350-360.

[48] Emery, T. R. (2007). *Identification of Damage in Composite Materials using Thermoelastic Stress Analysis.* thesis, University of Southampton.

[49] Haj-Ali, R., Wei, B.-S., Johnson, S., & El-Hajjar, R. (2008). *Thermoelastic and infrared-thermography methods for surface strains in cracked orthotropic composite materials.* Engineering Fracture Mechanics, 75(1), 58-75.

[50] Middleton, C. A., Weihrauch, M., Christian, W. J. R., Greene, R. J., & Patterson, E. A. (2020). *Detection and tracking of cracks based on thermoelastic stress analysis.* Royal Society Open Science, 7(12), 200823.

[51] Carteron, L., Doudard, C., Calloch, S., Levieil, B., Beaudet, J., & Bridier, F. (2020). *Naval welded joints local stress assessment and fatigue cracks monitoring with quantitative thermoelastic stress analysis.* Theoretical and Applied Fracture Mechanics, 110, 102792.

[52] Brooks, C., & Rajic, N. (2022). *Automated visual tracking of crack growth in coupon and component level fatigue testing using thermoelastic stress analysis.* International Journal of Fatigue, 163, 107037.

[53] Middleton, C. A., Gaio, A., Greene, R. J., & Patterson, E. A. (2019). *Towards Automated Tracking of Initiation and Propagation of Cracks in Aluminium Alloy Coupons Using Thermoelastic Stress Analysis.* Journal of Nondestructive Evaluation, 38(1), 18.

[54] de Sá Rodrigues, F., Marques, R., Tabrizi, I. E., Kefal, A., Ali, H. Q., Yildiz, M., & Suleman, A. (2021). *A new methodology for thermoelastic model identification in composite materials using digital image correlation.* Optics and Lasers in Engineering, 146, 106689.

[55] Chen, D., Sun, S., Dulieu-Barton, J. M., Li, Q., & Wang, W. (2018). *Crack growth analysis in welded and non-welded T-joints based on lock-in digital image correlation and thermoelastic stress analysis.* International Journal of Fatigue, 110, 172-185.

[56] ASTM *ASTM E1316-22a Standard Terminology for Nondestructive Examinations.*

[57] Aggelis, D. G., Sause, M. G. R., Packo, P., Pullin, R., Grigg, S., Kek, T., & Lai, Y.-K. (2021). *Acoustic Emission.* In M. G. R. Sause & E. Jasiūnienė (Eds.), Structural Health Monitoring Damage Detection Systems for Aerospace (pp. 175-217). Cham: Springer International Publishing.

[58] ASTM *Standard Practice for Acoustic Emission Monitoring of Structures During Controlled Stimulation.*

[59] Pullin, R., Wright, B. J., Kapur, R., McCrory, J. P., Pearson, M., Evans, S. L., & Crivelli, D. (2017). *Feasibility of detecting orthopaedic screw overtightening using acoustic emission.* Proceedings of the Institution of Mechanical Engineers, Part H: Journal of Engineering in Medicine, 231(3), 213-221.

[60] Dong, L., Tao, Q., Hu, Q., Deng, S., Chen, Y., Luo, Q., & Zhang, X. (2022). *Acoustic emission source location method and experimental verification for structures containing unknown empty areas.* International Journal of Mining Science and Technology, 32(3), 487-497.

[61] Pascoe, J. A., Zarouchas, D. S., Alderliesten, R. C., & Benedictus, R. (2018). *Using acoustic emission to understand fatigue crack growth within a single load cycle.* Engineering Fracture Mechanics, 194, 281-300.

[62] Philippidis, T. P., Nikolaidis, V. N., & Anastassopoulos, A. A. (1998). *Damage characterization of carbon/carbon laminates using neural network techniques on AE signals.* NDT & E International, 31(5), 329-340.

[63] Schumacher, T., Linzer, L., & Grosse, C. U. (2022). *Signal-Based AE Analysis.* In C. U. Grosse, M. Ohtsu, D. G. Aggelis & T. Shiotani (Eds.), Acoustic Emission Testing: Basics for Research – Applications in Engineering (pp. 73-116). Cham: Springer International Publishing.

[64] Haneef, T., Lahiri, B. B., Bagavathiappan, S., Mukhopadhyay, C. K., Philip, J., Rao, B. P. C., & Jayakumar, T. (2015). *Study of the tensile behavior of AISI type 316 stainless steel using acoustic emission and infrared thermography techniques.* Journal of Materials Research and Technology, 4(3), 241-253.

[65] Ghaib, M., Shateri, M., Thomson, D., & Svecova, D. (2018). *Study of FRP bars under tension using acoustic emission detection technique.* Journal of Civil Structural Health Monitoring, 8.

[66] Eitzen, D. G., & Wadley, H. N. G. (1984). *Acoustic Emission: Establishing the Fundamentals.* J Res Natl Bur Stand (1977), 89(1), 75-100.

[67] Kaiser, J. (1953). *Erkenntnisse und Folgerungen aus der Messung von Geräuschen bei Zugbeanspruchung von metallischen Werkstoffen.* Archiv für das Eisenhüttenwesen, 24(1-2), 43-45.

[68] Lyons, R. G. (2011). *Understanding Digital Signal Processing. Pearson (3 ed.).* ISBN: 0137027419.

[69] Kaiser, J. (1950). *Untersuchung über das Auftreten von Geräuschen beim Zugversuch.* thesis, Technische Hochschule Munich.

[70] Fowler, T. J. (1977). *Acoustic emission testing of fiber reinforced plastics*. Presented at the ASCE Fall Convention.

[71] M. R. Kaphle, A. C.C. Tan, D. P. Thambiratnam, & Chan, T. H. T. (2011). *Study of Acoustic Emission Data Analysis Tools for Structural Health Monitoring Applications.* Journal of Acoustic Emission, 29.

[72] Aggelis, D. G., Kordatos, E. Z., & Matikas, T. E. (2011). *Acoustic emission for fatigue damage characterization in metal plates.* Mechanics Research Communications, 38(2), 106-110.

[73] Crivelli, D., McCrory, J., Miccoli, S., Pullin, R., & Clarke, A. (2018). *Gear tooth root fatigue test monitoring with continuous acoustic emission: Advanced signal processing techniques for detection of incipient failure.* Structural Health Monitoring, 17(3), 423-433.

[74] Strantza, M., Aggelis, D. G., De Baere, D., Guillaume, P., & Van Hemelrijck, D. (2015). *Evaluation of SHM System Produced by Additive Manufacturing via Acoustic Emission and Other NDT Methods.* Sensors, 15(10), 26709-26725.

[75] Strantza, M., Van Hemelrijck, D., Guillaume, P., & Aggelis, D. G. (2017). *Acoustic emission monitoring of crack propagation in additively manufactured and conventional titanium components.* Mechanics Research Communications, 84, 8-13.

[76] Li, B., Tong, X., Feng, Z., & Yao, L. *Infrared thermography and acoustic emission in 2D plain woven C/Sic composites under tensile-tensile fatigue loading.* In (Vol. 118-120, pp. 251-255).

[77] Cuadra, J., Vanniamparambil, P. A., Hazeli, K., Bartoli, I., & Kontsos, A. (2013). *Damage quantification in polymer composites using a hybrid NDT approach.* Composites Science and Technology, 83, 11-21.

[78] Dassios, K. G., Kordatos, E. Z., Aggelis, D. G., & Matikas, T. E. (2014). *Crack Growth Monitoring in Ceramic Matrix Composites by Combined Infrared Thermography and Acoustic Emission.* Journal of the American Ceramic Society, 97(1), 251-257.

[79] Giudice, F., Rosa, G. L., Savio, F. L., & Clienti, C. (2019). *Comparison between thermal energy and acoustic emission for the fatigue behavior of steels.* Procedia Structural Integrity, 18, 886-890.

[80] Ouyang, H., Shi, J., Sakamoto, H., & Zhao, G. H. . (2016). *Characterizing Fracture Development in Ti-Alloy with I-Type Cracks Using Acoustic Emission and Thermal Infrared Imaging.* Key Engineering Materials, 725, 477–482.

[81] Barile, C., Casavola, C., Pappalettera, G., & Pappalettere, C. (2016). *Analysis of crack propagation in stainless steel by comparing acoustic emissions and infrared thermography data.* Engineering Failure Analysis, 69, 35-42.

[82] Plotnikov, Y., Henkel, D., Burdick, J., French, A., Sions, J., & Bourne, K. (2019). *Infrared-assisted acoustic emission process monitoring for additive manufacturing.* AIP Conference Proceedings, 2102(1), 020006.

[83] Kordatos, E. Z., Dassios, K. G., Aggelis, D. G., & Matikas, T. E. (2013). *Rapid evaluation of the fatigue limit in composites using infrared lock-in thermography and acoustic emission*. Mechanics Research Communications, 54, 14-20.

[84] Eaton, M. J., Pullin, R., & Holford, K. M. (2012). *Acoustic emission source location in composite materials using Delta T Mapping.* Composites Part A: Applied Science and Manufacturing, 43(6), 856-863.

[85] Dutton, A. (2004). *Thermoelastic stress measurement and acoustic emission monitoring in wind turbine blade testing.* Presented at the European Wind Energy Conference London, 2004.

[86] Middleton, C., McCrory, J., Greene, R., Holford, K., & Patterson, E. (2019). *Detecting and Monitoring Cracks in Aerospace Materials Using Post-Processing of TSA and AE Data.* Metals, 9, 748.

[87] Kordatos, E. Z., Aggelis, D. G., & Matikas, T. E. (2012). *Monitoring mechanical damage in structural materials using complimentary NDE techniques based on thermography and acoustic emission.* Composites Part B: Engineering, 43(6), 2676-2686.

[88] Robinson, A. F., Dulieu-Barton, J., Quinn, S., & Burguete, R. (2010). *Thermoelastic investigation of residual stress: Plastic deformation and the change in thermoelastic constant.* Presented at the ICEM 14 – 14th International Conference on Experimental Mechanics 2010.

[89] R. Boyer, G. Welsch, & Collings, E. W. (1994). *Materials Properties Handbook: Titanium Alloys*.

[90] ASM International (1990), *Metals Handbook, Vol.2 - Properties and Selection: Nonferrous Alloys and Special-Purpose Materials*. 10th edition.

[91] Daniel, I. M., Luo, J. J., Sifniotopoulos, C. G., & Chun, H. J. (1998). *ACOUSTIC EMISSION MONITORING OF FATIGUE DAMAGE IN METALS*. Nondestructive Testing and Evaluation, 14(1-2), 71-87.

[92] Sanford, R. (2002). *Principles of Fracture Mechanics 1st Edition*.

[93] MechaniCalc. (2022). *Fracture mechanics*. Retrieved 02/04, 2023, from https://mechanicalc.com/reference/fracture-mechanics#references.

[94] Zealand, M. N. (2023). *PureThermal Mini Pro JST-SR (with FLIR Lepton 3.5)*. Retrieved 03/04, 2023, from https://www.mindkits.co.nz/PureThermal-Mini-Pro-JST-SR-with-FLIR-Lepton-3-5.aspx?feed=Froogle&gclid=Cj0KCQjwz6ShBhCMARIsAH9A0qUqTQvsRWjGSKT6k8rOV06n00Jqu7LXvNCjagqpmelZn65PvPg9ItwaAm_7EALw_wcB.

[95] Rajic, N., & Rowlands, D. (2013). *Thermoelastic stress analysis with a compact low-cost microbolometer system.* Quantitative InfraRed Thermography Journal, 10(2), 135-158.

[96] Fabrizia Ghezzo, Anthony F. Starr, & Smith, D. R. (2010). *Integration of Networks of Sensors and Electronics for Structural Health Monitoring of Composite Materials.* Advances in Civil Engineering, 2010.

[97] Ramanathan, A. K., Gingerich, M. B., Headings, L. M., & Dapino, M. J. (2022). *Metal structures embedded with piezoelectric PVDF sensors using ultrasonic additive manufacturing.* Manufacturing Letters, 31, 96-100.

Appendix A

optris PI 640i
TECHNICAL DATA

optris
infrared measurements

Thermography in VGA resolution

Features:

- 640 x 480 pixels
- Superb thermal sensitivity of 40 mK
- Radiometric video recording with 32 Hz / 125 Hz in subframe mode
- Interchangeable lenses: 15°, 33°, 60° and 90°
- Licence-free analysis software and complete SDK inclusive

Technical specifications

Optical resolution	640 x 480 pixels
Detector	FPA, uncooled (17 µm x 17 µm)
Spectral range	8 – 14 µm
Temperature ranges	–20 ... 100 °C, 0 ... 250 °C, (20) 150 ... 900 °C[1] optional temperature range: 200 ... 1500 °C
Frame rate	32 Hz / 125 Hz @ 640 x 120 pixels
Optics (FOV)	15° x 11° FOV / f = 41.5 mm or 33° x 25° FOV / f = 18.7 mm or 60° x 45° FOV / f = 10.5 mm or 90° x 64° FOV / f = 7.7 mm
Thermal sensitivity (NETD)	40 mK
Accuracy	±2 °C or ±2 %, whichever is greater
PC interface	USB 2.0 / optional USB GigE (PoE) interface
Process interface (PIF), standard	0 – 10 V input, digital input (max. 24 V), 0 – 10 V output
Process interface (PIF), industrial	2x 0 – 10 V input, digital input (max. 24 V), 3x 0/4 – 20 mA outputs, 3x relay (0 – 30 V/ 400 mA), fail-safe relay
Cable length (USB)	1 m (standard), 5 m, 10 m, 20 m 5 m and 10 m also as high temperature USB cable (180 or 250 °C)
Ambient temperature	0 ... 50 °C
Storage temperature	–40 ... 85 °C
Relative humidity	20 – 80 %, non-condensing
Enclosure (size / rating)	46 x 56 x 76 – 100 mm (depending on lens + focus position) / IP 67 (NEMA)
Weight	269 - 340 g (depending on lens)
Shock / Vibration [2]	IEC 60068-2-27 (25G and 50G) / IEC 60068-2-6 (sinus shaped), IEC 60068-2-64 (broadband noise)
Tripod mount	¼-20 UNC
Power supply	via USB
Scope of supply	• USB camera with 1 lens • USB cable (1 m) • Table tripod • Standard PIF with cable (1 m) and terminal block • Software package optris PIX Connect • Hard transport case

[1] Accuracy effective starting at 150 °C

[2] For more details see operator's manual

For further information as well as the product configurator, please visit:
www.optris.global/thermal-imager-optris-pi-640

Optris GmbH · Ferdinand-Buisson-Str. 14 · 13127 Berlin · Germany
Phone: +49 30 500 197-0 · Fax: +49 30 500 197-10 · Email: sales@optris.global · www.optris.global

Appendix B

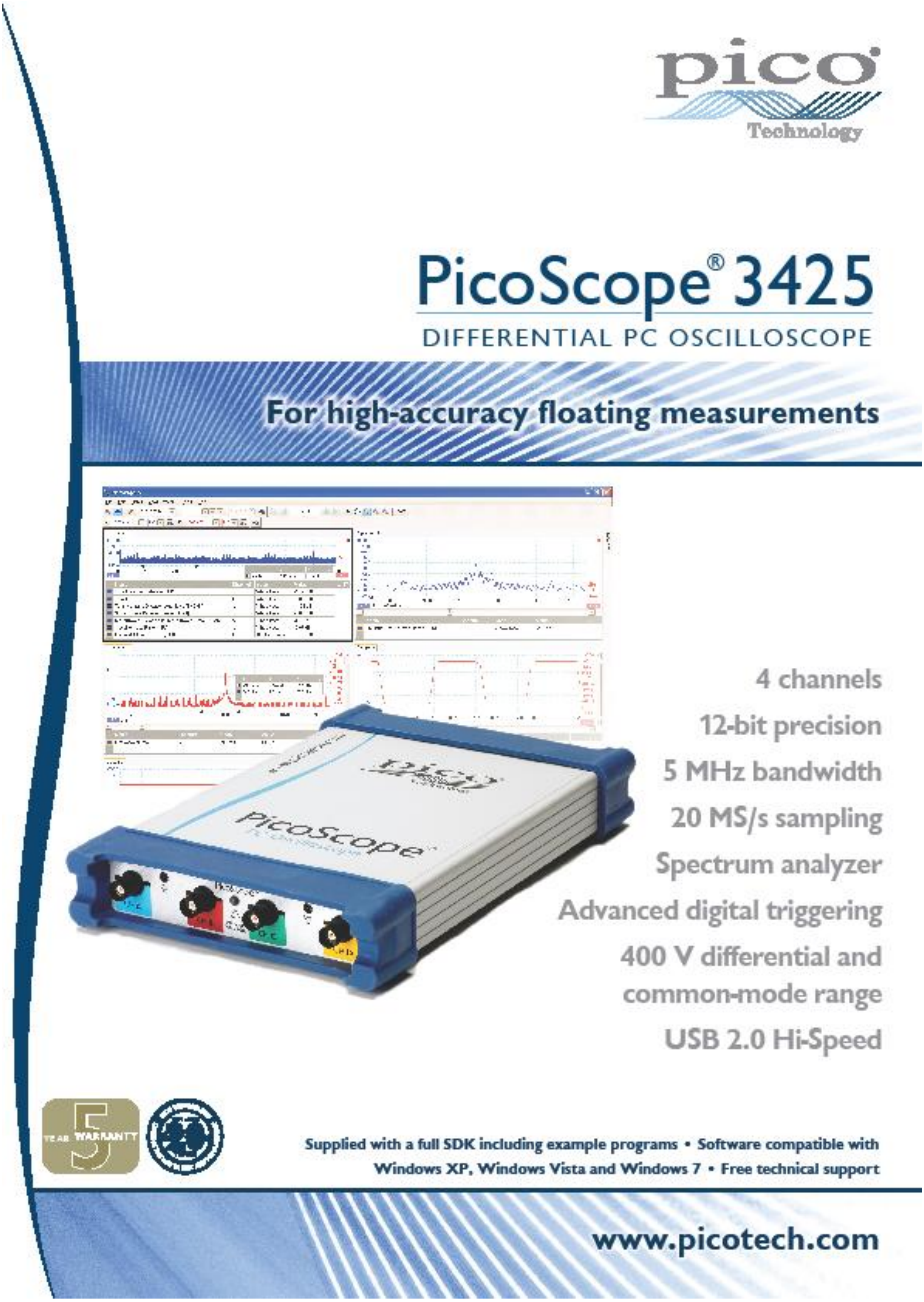

pico Technology

PicoScope® 3425

DIFFERENTIAL PC OSCILLOSCOPE

For high-accuracy floating measurements

4 channels

12-bit precision

5 MHz bandwidth

20 MS/s sampling

Spectrum analyzer

Advanced digital triggering

400 V differential and common-mode range

USB 2.0 Hi-Speed

5 YEAR WARRANTY

Supplied with a full SDK including example programs • Software compatible with Windows XP, Windows Vista and Windows 7 • Free technical support

www.picotech.com

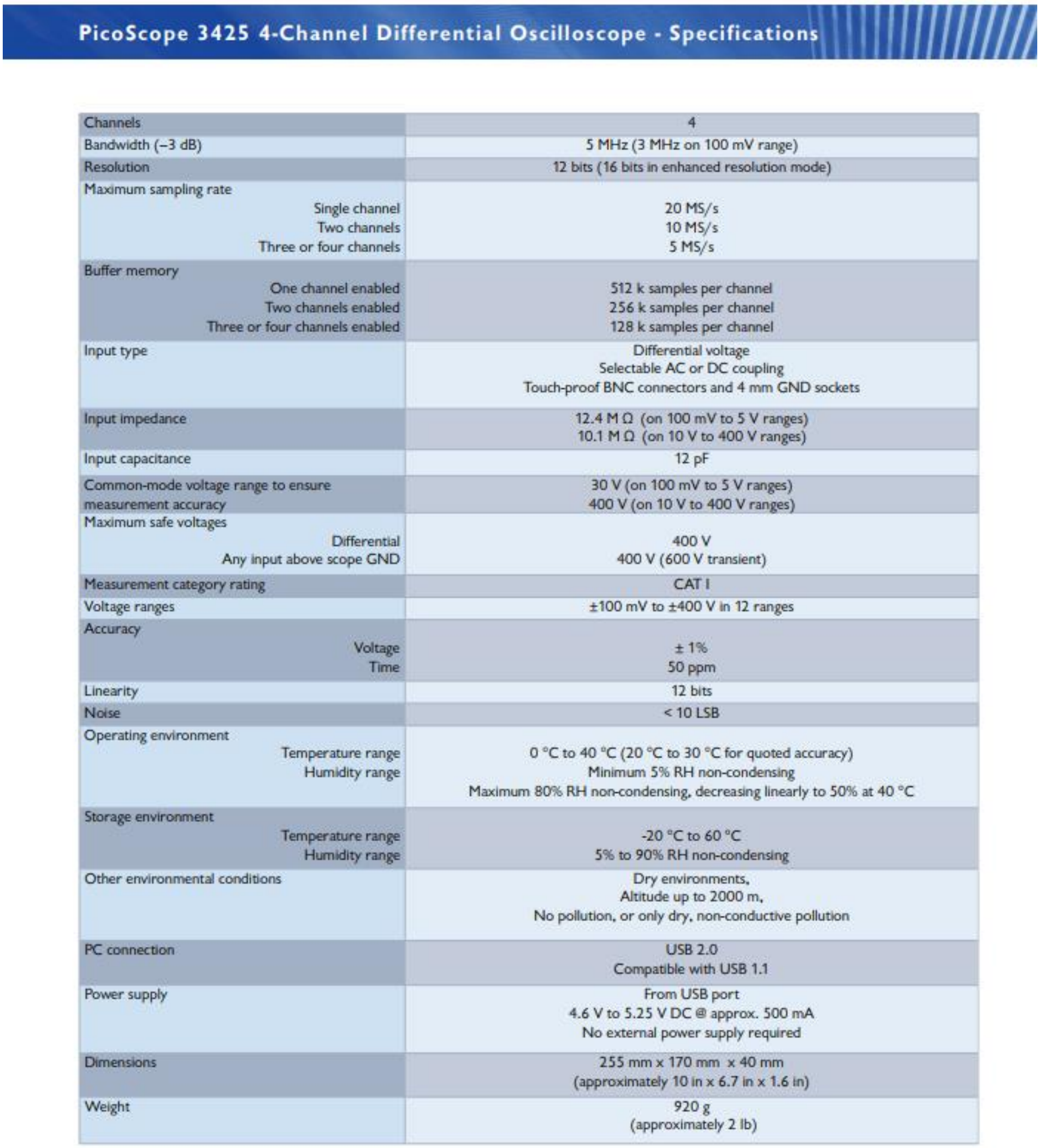

PicoScope 3425 4-Channel Differential Oscilloscope - Specifications

Channels	4
Bandwidth (−3 dB)	5 MHz (3 MHz on 100 mV range)
Resolution	12 bits (16 bits in enhanced resolution mode)
Maximum sampling rate	
Single channel	20 MS/s
Two channels	10 MS/s
Three or four channels	5 MS/s
Buffer memory	
One channel enabled	512 k samples per channel
Two channels enabled	256 k samples per channel
Three or four channels enabled	128 k samples per channel
Input type	Differential voltage Selectable AC or DC coupling Touch-proof BNC connectors and 4 mm GND sockets
Input impedance	12.4 M Ω (on 100 mV to 5 V ranges) 10.1 M Ω (on 10 V to 400 V ranges)
Input capacitance	12 pF
Common-mode voltage range to ensure measurement accuracy	30 V (on 100 mV to 5 V ranges) 400 V (on 10 V to 400 V ranges)
Maximum safe voltages	
Differential	400 V
Any input above scope GND	400 V (600 V transient)
Measurement category rating	CAT I
Voltage ranges	±100 mV to ±400 V in 12 ranges
Accuracy	
Voltage	± 1%
Time	50 ppm
Linearity	12 bits
Noise	< 10 LSB
Operating environment	
Temperature range	0 °C to 40 °C (20 °C to 30 °C for quoted accuracy)
Humidity range	Minimum 5% RH non-condensing Maximum 80% RH non-condensing, decreasing linearly to 50% at 40 °C
Storage environment	
Temperature range	-20 °C to 60 °C
Humidity range	5% to 90% RH non-condensing
Other environmental conditions	Dry environments, Altitude up to 2000 m, No pollution, or only dry, non-conductive pollution
PC connection	USB 2.0 Compatible with USB 1.1
Power supply	From USB port 4.6 V to 5.25 V DC @ approx. 500 mA No external power supply required
Dimensions	255 mm x 170 mm x 40 mm (approximately 10 in x 6.7 in x 1.6 in)
Weight	920 g (approximately 2 lb)

Appendix C

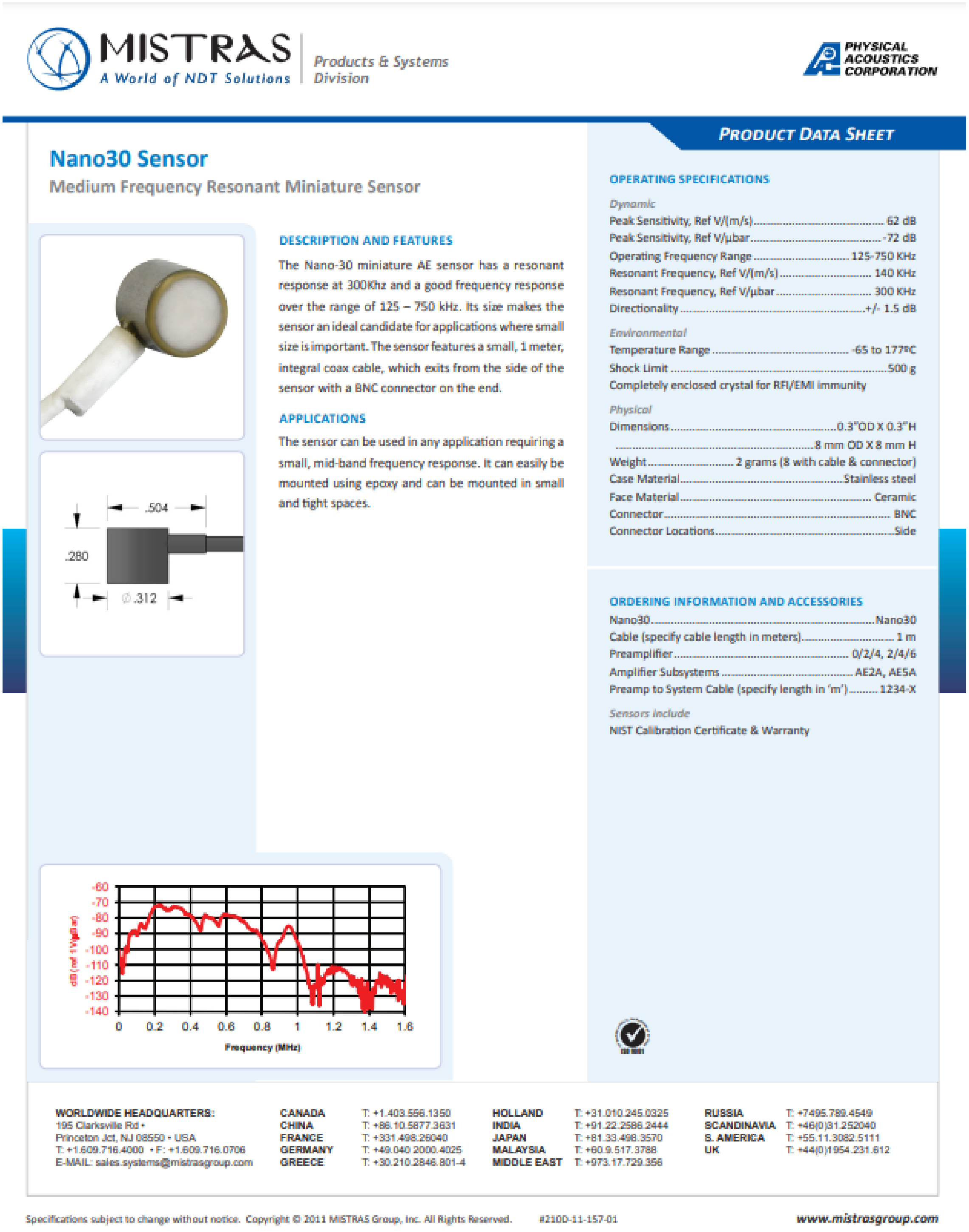

Nano30 Sensor

Medium Frequency Resonant Miniature Sensor

DESCRIPTION AND FEATURES

The Nano-30 miniature AE sensor has a resonant response at 300Khz and a good frequency response over the range of 125 – 750 kHz. Its size makes the sensor an ideal candidate for applications where small size is important. The sensor features a small, 1 meter, integral coax cable, which exits from the side of the sensor with a BNC connector on the end.

APPLICATIONS

The sensor can be used in any application requiring a small, mid-band frequency response. It can easily be mounted using epoxy and can be mounted in small and tight spaces.

OPERATING SPECIFICATIONS

Dynamic

Peak Sensitivity, Ref V/(m/s)	62 dB
Peak Sensitivity, Ref V/µbar	-72 dB
Operating Frequency Range	125-750 KHz
Resonant Frequency, Ref V/(m/s)	140 KHz
Resonant Frequency, Ref V/µbar	300 KHz
Directionality	+/- 1.5 dB

Environmental

Temperature Range	-65 to 177ºC
Shock Limit	500 g

Completely enclosed crystal for RFI/EMI immunity

Physical

Dimensions	0.3"OD X 0.3"H
	8 mm OD X 8 mm H
Weight	2 grams (8 with cable & connector)
Case Material	Stainless steel
Face Material	Ceramic
Connector	BNC
Connector Locations	Side

ORDERING INFORMATION AND ACCESSORIES

Nano30	Nano30
Cable (specify cable length in meters)	1 m
Preamplifier	0/2/4, 2/4/6
Amplifier Subsystems	AE2A, AE5A
Preamp to System Cable (specify length in 'm')	1234-X

Sensors include

NIST Calibration Certificate & Warranty

WORLDWIDE HEADQUARTERS:
195 Clarksville Rd •
Princeton Jct, NJ 08550 • USA
T: +1.609.716.4000 • F: +1.609.716.0706
E-MAIL: sales.systems@mistrasgroup.com

CANADA	T: +1.403.556.1350
CHINA	T: +86.10.5877.3631
FRANCE	T: +331.498.26040
GERMANY	T: +49.040 2000.4025
GREECE	T: +30.210.2846.801-4
HOLLAND	T: +31.010.245.0325
INDIA	T: +91.22.2586.2444
JAPAN	T: +81.33.498.3570
MALAYSIA	T: +60.9.517.3788
MIDDLE EAST	T: +973.17.729.356
RUSSIA	T: +7495.789.4549
SCANDINAVIA	T: +46(0)31.252040
S. AMERICA	T: +55.11.3082.5111
UK	T: +44(0)1954.231.612

#2100-11-157-01 www.mistrasgroup.com